

Contents

ABSTRACT	3
STATEMENT OF AUTHORSHIP.....	4
ACKNOWLEDGEMENTS	5
CHAPTER 1: GEOSPACE, THE IONOSPHERE, AND MIDDLE ATMOSPHERE ..	6
1.1 GEOSPACE.....	6
1.2 THE VERTICAL STRUCTURE OF THE EARTH’S ATMOSPHERE	8
1.3 THE IONOSPHERE	10
1.4 THE MESOSPHERE AND THERMOSPHERE.....	11
1.4.1 Composition of the Mesosphere.....	12
1.4.2 Dynamics of the Mesosphere	13
1.4.3 D- and E-Regions.....	14
1.4.4 Neutral winds.....	15
CHAPTER 2: METEOR ECHOES AND OBSERVING THEM WITH SUPERDARN RADARS.....	17
2.1 METEOR BACKGROUND INFORMATION	17
2.2 METEOR OBSERVATION TECHNIQUES	19
2.3 THE SUPER DUAL AURORAL RADAR NETWORK (SUPERDARN)	21
2.4 THE TASMAN INTERNATIONAL GEOSPACE ENVIRONMENT RADAR (TIGER).....	22
2.5 CHARACTERISTICS OF SUPERDARN METEOR ECHOES	26
2.6 OPTIMISING METEOR ECHO DETECTION RATES.....	30
CHAPTER 3: “METEOR_FREQ,” 1 TO 2 MARCH 2003.....	32
3.1 EXPERIMENT	32
3.2 METEOR_FREQ RESULTS	33
3.3 SEPARATION OF RESULTS ACCORDING TO FREQUENCY	36
3.4 DESCENDING PLASMA STREAMS (DPSs)	39
3.5 PROBABILITY DISTRIBUTION FUNCTIONS OF DPS EVENTS	40
3.6 ECHOES DETECTED AT 12 MHz WITH SPECTRAL WIDTH $<50 \text{ m s}^{-1}$	43

CHAPTER 4: “METEOR_SCAN1,” 6 TO 10 MARCH 2003	46
4.1 EXPERIMENT	46
4.2 METEOR_SCAN1 RESULTS	47
4.3 ECHOES RECORDED AT 14 MHz WITH SPECTRAL WIDTH $<50 \text{ m s}^{-1}$	54
CHAPTER 5: “METEOR_SCAN2,” 23 TO 25 MAY 2003	59
5.1 EXPERIMENT	59
5.2 “METEOR_SCAN2” RESULTS	60
5.3 METEOR_SCAN2 SPECTRAL WIDTH ANALYSIS	62
5.4 ECHOES RECORDED AT FREQUENCY 12 MHz WITH SPECTRAL WIDTH	66
300–600 m s^{-1}	66
5.5 ECHOES RECORDED AT FREQUENCY 12 MHz WITH SPECTRAL WIDTH $<50 \text{ m s}^{-1}$..	70
SUMMARY AND CONCLUSIONS	74
FUTURE WORK.....	77
APPENDIX A.....	79
BAS .MET FILE CONTENTS	79
APPENDIX B.....	80
SEPARATION OF RESULTS ACCORDING TO FREQUENCY	80
BIBLIOGRAPHY.....	83

Abstract

SuperDARN HF backscatter radars can be used to detect meteor echoes and estimate mesospheric winds. Large meteor echo detection rates increase the accuracy of the wind estimates, and also permit them to be estimated with better time and height resolution. Larger meteor echo detection rates can be achieved by modifying the radar hardware, radar operating parameters, real-time signal processing, and the post-processing analysis of echoes. In this study, enhanced meteor echo detection rates were achieved by modifying TIGER operating parameters and improving the post processing analysis. The characteristics of several different kinds of echoes which contaminate the meteor echo population were identified. Echoes with unusually large spectral widths ($\sim 300\text{--}500\text{ m s}^{-1}$) were observed scattered throughout the meteor echo population. Their characteristics were otherwise the same as meteor echoes, and their large spectral widths were probably an artefact caused by a limitation of the algorithm used of process echoes with marginal signal-to-noise ratio. However, the large spectral widths may have been caused by a plasma instability acting upon the meteor trails. Another kind of echo was of ionospheric origin and formed thin, continuous traces decreasing in group range from $\sim 1200\text{ km}$ to $\sim 300\text{ km}$ in range-time summary plots. These “descending plasma streams” (DPS) merged into and disappeared at the group ranges of meteor echoes. DPS traces were striated in group range, and oscillated on atmospheric gravity-wave time scales ($\sim 15\text{ min}$ to 2 h). Their behaviour resembled sporadic E associated with proton aurora as observed by other SuperDARN radars, and tidal ion layers observed by incoherent scatter radars.

Statement of Authorship

Except where reference is made to the text of the thesis, this thesis contains no material published elsewhere or extracted in whole or in part from a thesis presented by me for another degree or diploma.

No other persons' work has been used without due acknowledgement in the main text of the thesis.

This thesis has not been submitted for the award of any other degree or diploma in any other tertiary institution.

Deanna Matthews

Acknowledgements

Firstly I would sincerely like to thank Dr Murray Parkinson for his guidance, wisdom, and insight into all aspects of this thesis, and for his willingness to explain all, from the most important theories to the most trivial programming requirements. Your assistance and input were invaluable.

I would also like to thank Professor Peter Dyson for his leadership, support, and assistance throughout the project. Thank you, also, for providing the facilities and resources to enable this project to take place.

Thank you also to Dr Paul Pigram and Rudy Bursa for their advice and assistance throughout the year.

Lastly, I would like to thank my family and Toby Balfour. Without their ongoing support and encouragement, I would not have been able complete this year.

Chapter 1: Geospace, the Ionosphere, and Middle Atmosphere

1.1 Geospace

Most ionospheric and upper atmosphere phenomena are influenced by complex processes occurring millions of kilometres away in the ever-evolving layers of the Sun; and although the 149 million kilometres of “Space” separating these layers and the Earth is often considered a vast vacuum, it is in fact a highly dynamic region filled with particles and fields. Fluctuating clouds of charged particles are expelled from the Sun carrying the relatively weak interplanetary magnetic field (IMF) through the vacuum. This outward flow of fully ionised hydrogen/helium plasma, the Solar Wind (Parker, 1963), can travel at speeds up to 2000 km s^{-1} (Parker, 1963) during coronal mass ejections (CMEs), as seen in Figure 1.0. The exact origin of the solar wind and CMEs is not fully understood, however it is proposed they are a result of interactions between the Sun’s magnetic field lines in the corona, and not a consequence of solar flares as originally thought. The higher and larger field lines form loops and arches over the lower emerging field lines (Figure 1.0) holding them down, thus preventing the plasma they carry from escaping.

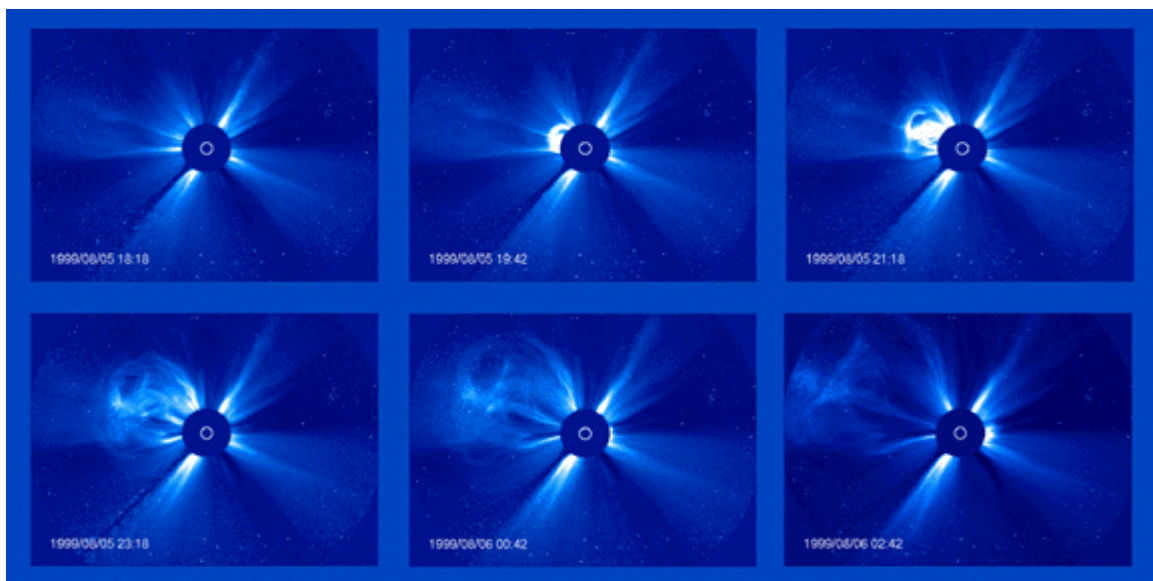


Figure 1.0: Progress of a Coronal Mass Ejection (CME) observed over an eight hour period on 5 – 6 August 1999 by LASCO C3 (SOHO). The dark disk blocks the Sun so that the LASCO instrument can observe the structures of the corona in visible light. The white circle represents the size and position of the Sun (courtesy of SOHO/LASCO C3 consortium).

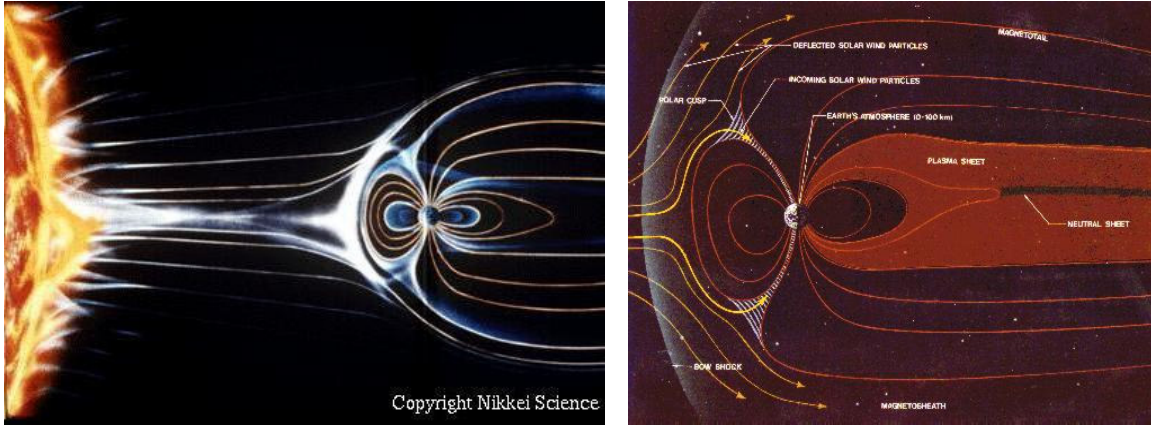


Figure 1.1: (a) High speed plasma from the Sun compresses the dayside Magnetosphere and extends the nightside magnetotail, (b) The dynamics and structure of Geospace (courtesy of NASA GSFC).

Magnetic and plasma pressure therefore builds up, only to be released through a magnetic “hole” formed when oppositely directed field lines merge and cancel each other out (i.e., a reconnection event). It is through this “hole” that the CME is released (see <http://www-istp.gsfc.nasa.gov/istp/outreach/cmeposter/hurricane.html>).

Upon escaping the corona, the plasma bubble of the CME travels at high speed with the IMF. The ionised plasma cloud is frozen into the Sun’s magnetic field, spiralling radially outwards from the Sun until, in the case of Earth, it reaches the bow shock. The solar wind now encounters the region known as geospace, first being modified in the foreshock, bow shock, and magnetosheath, before encountering the magnetopause. These constitute the outer most layers of the Earth’s “atmosphere”. One effect of the high speed plasma buffeting against the magnetopause is clearly seen in Figure 1.1, compressing the dayside magnetosphere to geocentric distances of $\sim 10 R_E$, and stretching the nightside magnetotail millions of kilometres into space, well beyond the orbit of the moon.

The processes that follow a CME event reaching the magnetosphere are extremely complex, and not yet fully understood, and include the reconnection of IMF lines with the Earth’s magnetic field, redirection of plasma along the magnetopause to the polar cusps, and magnetic storms that modify ionospheric convection and the aurora.

The Sun is coupled to the magnetosphere by magnetic reconnection between the IMF B_z component and the geomagnetic field. Coupling between the magnetosphere and ionosphere is also via magnetic field lines, where magnetospheric electric fields map down to the ionosphere, driving the circulation of ionospheric plasma. This moving plasma collides with the neutral upper atmosphere, generating neutral winds and Joule heating within the neutral gas.

1.2 The Vertical Structure of the Earth's Atmosphere

The vertical structure of the atmosphere varies significantly in temperature and composition from sea level to the base of the magnetosphere, beyond which reside the exosphere where the neutral particles travel along gravitationally bound orbits. The primary classification of atmospheric regions is according to temperature gradient; however, they are also defined by variations in composition and state of mixing with altitude (Figure 1.2).

Within the temperature gradient system, regions are known as “spheres” and region boundaries as “pauses” (Hargreaves, 1992). Extending from sea level to ~14 km altitude is the troposphere, the region of greatest density, where the temperature decreases from 290°K to 221°K. The top of this region is bounded by the tropopause which varies in height according to various factors including season and latitude. The stratosphere is notably drier and less dense than the troposphere, with temperatures increasing due to the absorption of UV radiation mainly by ozone (O_3), until a maximum of 270°K is reached at the stratopause (50 km). Another decrease in temperature gradient marks the beginning of the mesosphere (literally meaning “middle atmosphere”), where temperatures reach 170°K at the mesopause (~85 km). The summer mesosphere is the coldest region of the atmosphere, and it may prove to be a sensitive indicator of global climate change. At 100 km, the increase in incident solar radiation and weak atmospheric density, ensure a positive temperature gradient in the thermosphere. From 100 km to ~300 km, the

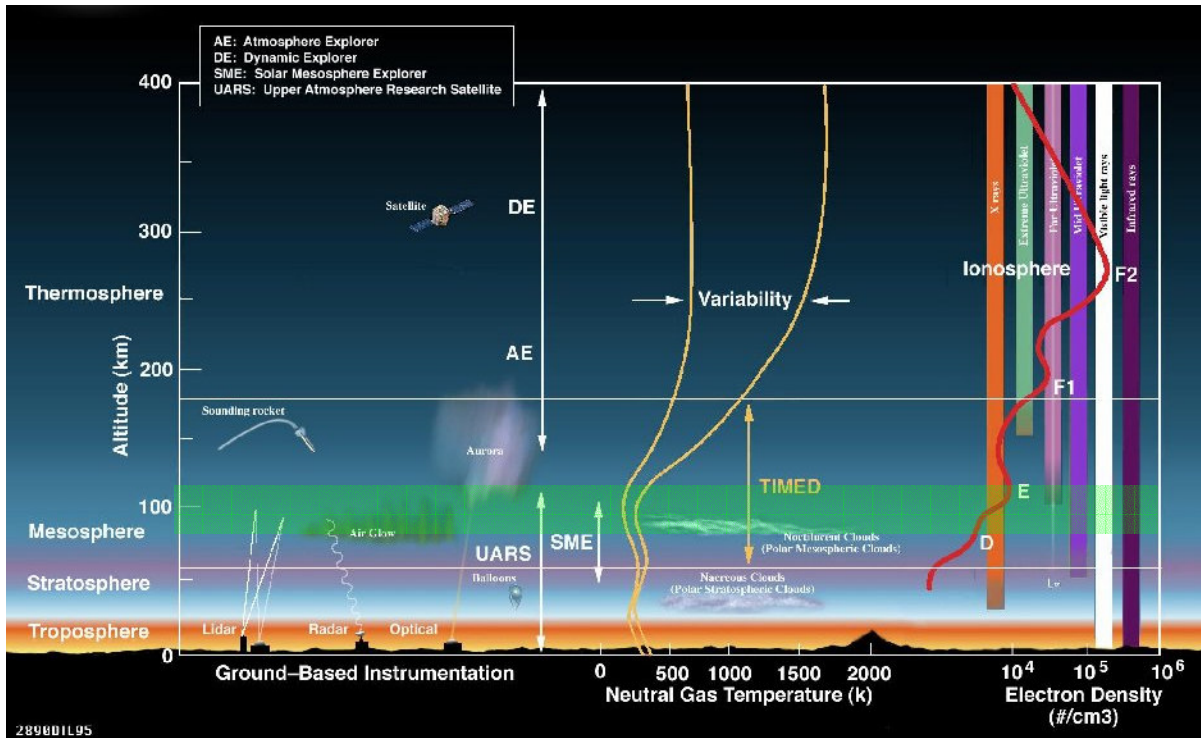


Figure 1.2: Vertical structure of Earth's Atmosphere. Important features are the temperature and electron density variation with altitude, and the existence of ionospheric layers. The transparent green band represents the meteor region (courtesy of NASA TIMED Mission).

temperature continually increases to a maximum over 1500° K, at which point it becomes almost constant. Figure 1.2 shows that this maximum temperature has large variability due to changing solar flux and geomagnetic activity. However the thermosphere is the hottest region of the atmosphere.

The ablation of meteors, the focus of this thesis, maximises in the mesosphere and lower thermosphere. Meteor trails are detected between ~80 and 120 km using the classical VHF meteor radar technique, as will be described in Chapter 2.

1.3 The Ionosphere

Classified by its vertical structure and composition, the ionosphere is a weakly ionised region of the atmosphere, nevertheless containing significant amounts of positive and negative ions, and free electrons from 60 km to ~1000 km (Hargreaves, 1992). Equal quantities of positive and negative charges give the ionosphere overall charge neutrality. However, the plasma plays a major role in the dynamics of the thermosphere, and it has a significant influence on regions at lower and higher altitude. Ultraviolet and X-ray photons are the primary producer of ionisation, but collisions with precipitating particles also play an important role, especially in the auroral regions. Cosmic rays also make a small but significant contribution.

Free electrons influence the propagation of radio frequency electromagnetic waves through the ionosphere, thus allowing for investigation of the region using different kinds of radars operating from median (MF) to ultrahigh (UHF) radio frequencies. The ionosphere comprises four main layers, defined by their height (km), composition and electron density (m^{-3}), as given in Table 1.0. Figure 1.3 illustrates how these layers are not a permanent feature of the ionosphere, with the D, F1, and E regions usually vanishing at night, but the F2 layer persisting despite its reduced strength. Auroral E and sporadic E layers also occur during the night. The fact that the F2 layer remains allows ionospheric radars to operate continuously over 24 hours. Meteor echoes are detected in the D and E regions, mostly at heights less than ~120 km.

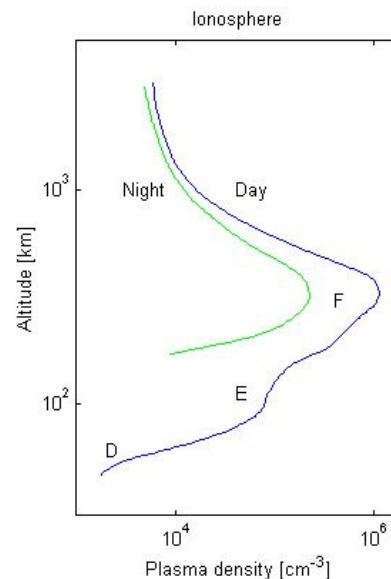


Figure 1.3: Day and night ionospheric profiles (courtesy of Space Physics Text Book of Oulu).

Table 1.0: Characteristics of the Daytime Ionospheric Layers. (Hargreaves, 1992).

Region	Height (km)	Composition	Electron Density (m^{-3})
D	60-90	NO^+ , O_2^+ , Negative ions	10^8-10^{10}
E	90-150	O_2^+ , NO^+	10^{11}
F1	150-180	O^+ , NO^+ , O_2^+ , N_2^+	$10^{11}-10^{12}$
F2	~300	O^+ , N^+ , H^+ , He^+	Up to several 10^{12}

Neutral atmospheric density decreases with increasing altitude; hence there is less gas to ionise and thus lower plasma densities in the extreme topside F region despite the increased availability and intensity of incident solar radiation. A peak in ionisation is thus produced, and can be modelled by a “Chapman layer”. As Figure 1.3 shows, maximum electron density usually occurs in the F2 region. Plasma is ultimately lost through recombination and diffusion.

1.4 The Mesosphere and Thermosphere

For many years the mesosphere was merely considered to be an uninteresting “in between” layer of Earth’s atmosphere, but an understanding of the importance of the layer is emerging. The mesosphere is the third highest layer of the neutral atmosphere, extending from 50 to 90 km above the Earth’s surface. Coupled to the thermosphere and stratosphere, the mesosphere is partly under solar control and partly influenced by weather in the lower atmosphere. The upper mesosphere and lower thermosphere provide a natural boundary between the predominantly neutral lower atmosphere and strongly plasma influenced upper atmosphere (Arnold *et al.*, 2003) (Figure 1.2).

Mesospheric dynamics and chemistry are closely linked, and the temperature profile of the region is most remarkable. Temperatures in the mesosphere decrease with increasing altitude, and the atmospheric gravity-wave dynamics driving the cold summer mesopause

and warm winter mesopause is topic of much interest. The summer mesopause can decrease to temperatures as low as 130°K making it the coldest natural terrestrial environment! Atmospheric gravity waves grow in amplitude and break within the lower air density of the mesosphere. The resulting atmospheric turbulence produces irregularities that can be observed using powerful VHF radars. Variability in the mesospheric winds will affect the meteor echoes measured by various radars, including HF backscatter radars.

The ionospheric D and E layers overlap the mesosphere and mesopause (Figure 1.2). Both regions exhibit very different characteristics and these will be discussed in Section 1.4.3. There have been extensive studies into the geomagnetic influences on the high latitude neutral atmosphere at E region heights (~110 km) (Dickinson *et al.*, 1984). However, there is still much to learn about this important region.

1.4.1 Composition of the Mesosphere

The upper mesosphere is a transition region for several processes, and constituents are transported either by advection or diffusion, both of which are a consequence of gravity-wave saturation. The chemical families O_x and HO_x go from photochemical control in the upper mesosphere to dynamical control in the lower thermosphere. Mesospheric temperature decreases with increasing altitude, with cooling via infrared radiation emissions from CO_2 (~85 km), and solar and chemical heating through O_2 and O_3 (~30 km) (Viereck, 1991). A consequence of this behaviour is a region, warm at the bottom (250–300°K) and cold at the top (130–220°K). The polar mesosphere has warm winters (130–220°K) and cold summers (130°K). During the summer it is cold enough to freeze H_2O vapour into ice clouds. This contributes to the formation of noctilucent clouds (NLC) and polar mesospheric clouds (PMC).

A sodium layer extending from 80–110 km, and peaking at 90 km, undergoes significant fluctuations in density and often has the effects of gravity waves are imposed on its

vertical density profile. Tidal fluctuations can also be seen in the total vertical abundance of sodium, and will therefore affect meteor ablation and hence the echoes detected from them.

Above 95 km, also in the meteor layer, a region of enhanced stability exists where there is a large abundance of nitrogen dioxide (N_2) (Gardner *et al.*, 2002). Meteor ablation lifetimes and meteor echoes will again be affected by the presence of an N_2 layer.

1.4.2 Dynamics of the Mesosphere

Planetary waves, tides and gravity waves play crucial roles in thermal and momentum budgets of the mesosphere. However, mean diurnal and annual temperature profiles demonstrate that, in the absence of gravity waves and tidal perturbations, the background atmosphere is statistically stable throughout the day and year (Viereck, 1991). Circulation near the upper mesopause is affected by both upward propagating waves, such as planetary scale Rossby waves, and by changes in solar irradiance and high energy particle precipitation (Arnold *et al.*, 2001). Thin layers of instability form in a 100 – 120 km layer in the middle atmosphere, and can only be generated when the combined perturbations associated with tides and gravity waves induce large vertical shears in the horizontal wind temperature profiles (Viereck, 1991).

Gravity wave saturation and dissipation have a profound effect on the structure, composition, and circulation of the middle atmosphere by transporting heat, horizontal momentum, and constituents (Viereck, 1991). Their energy is generally derived from large-scale motions of the neutral air, and although a phenomena of the neutral atmosphere, their effects can be transferred to higher altitude ions and electrons through collisions. Mesospheric gravity waves have periods of minutes to tens of minutes, and wavelengths up to hundreds of kilometres.

It has been proposed that gravity waves disperse energy in the form of wind by accelerating the mean flow (Viereck, 1991). “Momentum flux” is used to quantify the wind energy deposited by gravity waves. This energy deposition can result in turbulence, mean flow accelerations, and the production of secondary waves. Internal atmospheric waves propagate upward, with an increase in wave amplitudes with decreasing atmospheric density; however this occurs more slowly than predicted by the observed density. This is due to saturation of waves as they propagate upwards. There is a strong interaction between gravity waves and the diurnal tide.

Tidal oscillations are global in scale and periods are related to the solar (24 hour) or lunar (24.8 hour) day, and are produced by gravitational forces and thermal energy input (solar radiation). At mesospheric altitudes, atmospheric tides have diurnal (24 hour) and semidiurnal (12 hour) components, but other harmonics may be observed such as 6 and 8 hour waves. Tides alone are not sufficient to induce instabilities; yet when interacting with gravity waves the atmosphere can be destabilized.

Semidiurnal and diurnal tidal phases around 90 km exhibit a bimodal state with the phases almost constant near the northern hemisphere summer (June) and winter (December) solstices, and making rapid transitions near the equinoxes. The vertical wavelengths of tides are less than 100 km and the amplitude of the semidiurnal oscillation decreases with increasing latitude ($5\text{--}15 \text{ ms}^{-1}$) (Viereck, 1991).

1.4.3 D- and E-Regions

Below 90 km is the ionospheric D-layer is maintained by very energetic photons and high energy particle precipitation; hence this region remains at night. Incident galactic cosmic rays also help maintain the D-region and are present regardless of local time; even though solar photons at all wavelengths undergo extreme diurnal intensity fluctuations. D-layer conditions are therefore dependent on the prevailing solar activity and interplanetary conditions.

High ion-neutral collision frequencies mean radio-wave absorption is strong in the D-region. This makes the D-region important for radio communication. As it is the lowest ionospheric layer, only the most energetic ionisation sources can penetrate to D-region altitudes. X-rays from the Sun are the primary sources of ionisation at the top of the D-region, 80–90 km. Very intense Lyman-alpha radiation from the Sun has its peak production rate at ~70–80 km, and ionisation of cosmic ray particles dominates below (Kivelson *et al.*, 1995). The dominant ions, NO^+ and O_2^+ , can recombine with electrons; however at such low altitudes the electrons can also attach themselves to the nearest neutrals to form negative ions.

Extending from 90–150 km and peaking at above 100 km is the ionospheric E region. The behaviour of E-region is close to that of an ideal Chapman layer. That is, it is under direct and strong solar control, and so tends to disappear at night. In the E region the peak electron production is at an altitude of 110–115 km, where molecular gas is abundant. Molecular ions are therefore produced directly, and the loss rate is controlled by dissociative recombination. Sporadic E layers can be observed at altitudes of 90–120 km and are intermittent, narrow, and sometimes intense layers that are formed by wind shears and electric fields (Parkinson *et al.*, 1998). The mechanism that produces sporadic E layers is related to that by which a neutral wind may raise or lower the F region (Hargreaves, 1992).

1.4.4 Neutral winds

Radio frequency echoes from meteor ionisation trails provide a method for the detection and monitoring of neutral winds in the mesosphere. Such winds can also be measured from the Doppler shifts of spectral lines in airglow emission spectra. Near the poles, summer winds are extremely strong and blow east to west, while winter winds blow west to east. Within the auroral regions, the neutral winds change strongly with height. Fluctuation in vertical winds associated with gravity waves at altitudes of 85–100 km have been observed, as well as significant vertical shears between 90 and 100 km.

Thermospheric neutral winds follow isotherms blowing from the dayside over the pole to the nightside. E-region wind speeds are only one third of the F-region speeds on average. Due to strong coupling between neutrals and ions in the E-region, observations of ion motion can sometimes be used as a tracer for neutral winds. The neutral wind velocity due to convection electric fields and ion drag is given by

$$u = v_i - \frac{q}{m_i \nu_{in}} v_i \times B - \frac{q}{m_i \nu_{in}} E \quad (1.1)$$

where u is the neutral wind velocity, v_i is the ion velocity, m_i is the ion mass, ν_{in} is the neutral air collision frequency, q is the charge, B the magnetic field strength and E the electric field strength (see: <http://spaceweb.oulu.fi/education/>). At high latitudes where the magnetic field is almost vertical, this equation applies to the horizontal component of the neutral wind velocity while the vertical motion is assumed equal to the ion motion along the magnetic field.

Importantly, here, if ν_{in} is very large, the neutral velocity is equal to the ion velocity, and this explains why echoes from meteor trails can be used to measure neutral winds.

Chapter 2: Meteor Echoes and Observing Them With SuperDARN Radars

2.1 Meteor Background Information

It is believed approximately 1,000 tons of meteoric dust and rock enter the Earth's atmosphere each day from deep space (Quest, 1998), and the possible origin of these meteors include comets (over 90%), chips off asteroids, debris remaining from the formation of the planets and moons, and distant supernovae. When meteorites fall to the ground their origin can be determined by the mineral composition of the remaining meteorite. As a meteor plunges into the atmosphere at between 12 and 72 km s⁻¹ relative to the motion of the Earth (Zielik *et al.*, 1992) the surrounding air does not have time to flow around the meteor, and a shock front forms. The friction between the air and meteor produces enough heat to ablate the meteor and ionise the neutral air molecules. A long column of ionised plasma particles is therefore produced; the luminous meteor trail generally lasts for only tenths of a second. Very bright meteor trails can last up to a minute or more. Figure 2.0 presents an image from a video recorded of a meteor trail that lasted 10 seconds.



Figure 2.0: Slide from an animation of a meteor trail that lasted for 10 seconds (courtesy of Paulo Raymundo, www.spaceweather.com)

The wide range in meteoroid speeds is caused partly by the fact that the Earth itself is travelling at ~30 km s⁻¹ as it revolves around the Sun. From Figure 2.1 it can be seen that on the dusk side, or trailing edge of the Earth, only the meteoroids travelling faster than the Earth and in the same direction will be detected. On the dawn side, or leading edge of the Earth, meteoroids travelling slower

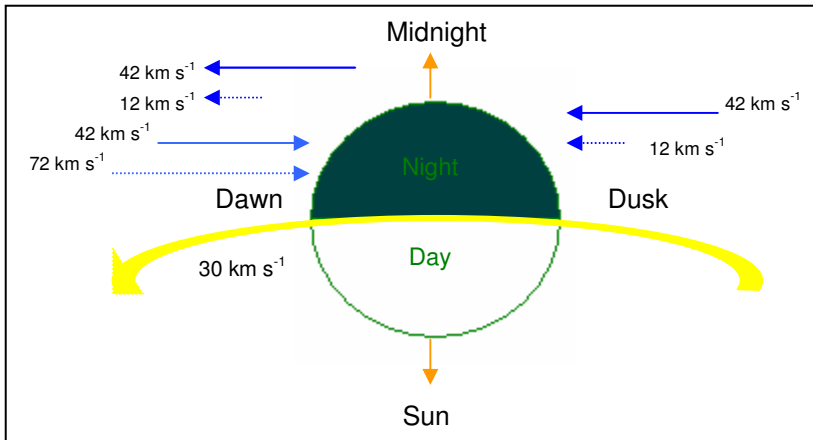


Figure 2.1: Meteor speeds. At dusk meteors catch up to the Earth. At dawn, the Earth catches up to most meteors (courtesy of Zeilik *et al.*, 1992).

than the Earth will also be observed. A diurnal variation of meteors is therefore observed, with peak detection rates at dawn.

Meteors with higher entry velocity will be heated more strongly during their passage

through the atmosphere, and thus more quickly ablated and produce denser ionisation trails than those with low velocities. The motion of the ionisation trails is under the influence of the neutral winds in the mesosphere and lower thermosphere region (80–110 km altitude). Radar pulses that arrive perpendicular to the meteor trails are strongly backscattered, and this type of scatter is known as Bragg scatter. There must be an irregularity within the meteor trail equal to half the radio wavelength for this reflection mechanism to work. Any wind-drifted meteor trails will backscatter the radio waves with a Doppler shift, enabling the determination of Doppler velocities of the meteor trails, and thus ultimately the neutral winds.

Meteor ablation is the chief process responsible for the existence of metallic species in the upper atmosphere. Longer-lived metallic ion species play a major role in the formation of dense layers of E-region ionisation known as sporadic E. At higher latitudes, meteoric dust is also thought to provide the condensation nuclei for formation of noctilucent clouds.

2.2 Meteor Observation Techniques

Several meteor and mesospheric wind observation methods are available including optical (visual, photographic, video), radio (meteor and ionospheric radars), and space-based methods. Ground-based meteor observation methods are classified into radio and optical methods, and space-based investigations make use of Earth orbiting satellites. Investigations in the radio spectrum utilise MF radars (D-region wind radars), HF radars (digital ionosondes and SuperDARN radars), VHF radars (classical meteor radars), and UHF radars (incoherent scatter radars). Many differences exist between all of these observation techniques, and as usual, detailed comparisons require immense caution.

Visual meteor observations use the naked eye to monitor meteor showers of medium and high activity. Meteors are counted or plotted onto gnomonic star charts. Although the accuracy of naked-eye observations is low compared to video observations or photography, the huge amount of data obtained every year provides statistically significant and valuable results. Photographic meteor detection involves the capture of meteors on photographic film, enabling the path of the meteor to be determined with a high degree of accuracy for meteors beyond the naked eye limit. Advanced video techniques presently facilitate the detection of meteors to +8 magnitude. Video observation is the youngest and one of the most advanced observing techniques in meteor science. Professional astronomers began utilising video equipment at the beginning of the seventies. Japanese (1986) and Dutch (1987) observers were amongst the first amateurs using this technology. In 1999, regular observations of meteor showers with automatic video systems commenced in Germany.

Upper atmosphere weather satellites have used the detection of meteors to study the mesosphere-lower thermosphere region. One current example is the TIMED (Thermosphere, Ionosphere, Mesosphere, Energetics, and Dynamics) mission which employs advances in remote-sensing technology to globally observe the Earth's atmosphere. The mission acquires direct measurements of wind, density, and temperature

profiles, thereby the various energy inputs and outputs can be inferred. Satellites can only obtain a couple of samples per day at any location, and often they precess in their orbit so the measurements will be recorded at different local times. Other experimental errors will place constraints on the quality of the data.

Dedicated, classical VHF meteor radars have been an important meteor detection method. They are optimised for the detection of meteors and winds in the mesosphere-lower thermosphere region, detecting meteor echoes with corresponding visual magnitudes down to +11. They operate at VHF (30 MHz) to minimise contamination from other ionospheric sources and ground scatter, and they have the advantage of lower background noise than at HF. However, there may be some advantages to using HF for meteor radars. For example, high gain antennas are easier to construct, and the height range gives better coverage of the lower thermosphere.

One meteor radar, the Advanced Meteor Orbit Radar (AMOR) (Marsh *et al.*, 2000), was designed to measure meridional winds by detecting of meteor echoes in the 80–120 km altitude region. It is located at Birdlings Flat, on the South Island of New Zealand (172°39'E, 43°34'S). AMOR operates at upper HF (26.2 MHz) with a 60-kW pulse and a pulse repetition frequency of 379 Hz. A fan-shaped antenna pattern is used to restrict the main beam to a width less than 2°, therefore measurements are obtained with 80 and 97% echo capture volumes of ~8 and 27 km³ at ranges of 200 km. Height and range uncertainties of ~1 km are obtained. Elevation angles are obtained via a dual interferometer consisting of three receiving antennas at the radar home site.

When performing mesospheric wind analysis using directional meteor data, a uniform flow throughout the sampling volume is assumed, thus enabling the calculation of the meridional and zonal wind components. A major problem with wind measurements is the presence of significant vertical shears in the 90 to 100 km altitude region.

An MF radar is also located at Birdlings Flat, New Zealand, and a Fabry-Perot Interferometer (FPI) is located nearby at Mt John (170°27'E, 43°59'N). Both are used to

study the mesosphere-lower thermosphere region. However, meteor radars have advantages over other systems. For example, they are able to measure winds over an entire day whereas MF wind radars are poor at making wind measurements at night, and FPIs struggle to obtain measurements during the day.

Digital ionosondes are ground-based ionospheric radars that measure the characteristics and movements of the ionosphere, including the virtual height, true height, phase height, Doppler shift, Doppler spread, and angle-of-arrival of echoes. Ionospheric sounding may be set up in the vertical or oblique mode, using pulsed or FMCW sounding techniques. Modern digital ionosondes have relatively low transmitter power because they rely on signal processing to improve their signal-to-noise ratio performance, so that it becomes comparable to that of the older high-power instruments.

The Canadian Advanced Digital Ionosonde (CADI) (MacDougall *et al.*, 2001) was adapted for meteor wind measurements. CADI consists of four receiver antennas (dipoles) along the centre of the four sides of a 60-m square. Each dipole is an untuned “fat” dipole of overall length 19 m and consists of a bundle of 4 wires spaced approximately 30 cm apart. The centre of each dipole is fed to a balanced high input impedance, wideband preamplifier. The transmitting antenna is a delta, using a relatively short mast (13 m). The small size of the delta severely restricts performance at frequencies below about 2 MHz, but it is still adequate for most of our studies. Operation frequencies range from 1–20 MHz, and the peak transmitter power is 600 W. The basic pulse length is 40 μ sec, with a pulse repetition frequency of 20 or 40 Hz.

2.3 The Super Dual Auroral Radar Network (SuperDARN)

Consisting of 15 radars in the Northern and Southern hemispheres, the Super Dual Auroral Radar Network (SuperDARN) was designed to monitor the auroral and polar cap ionospheres. Figure 2.2 shows the clustering of the Southern hemisphere SuperDARN

radars around the south geomagnetic pole. TIGER is currently the lowest latitude SuperDARN radar, and can measure meteor echoes and winds at mid-latitudes.

SuperDARN radars are oblique sounding, coherent scatter radars sensitive to Bragg scattering from small-scale electron density irregularities in the ionosphere (Greenwald *et al.*, 1995). SuperDARN radars transmit at frequencies from 8–20 MHz, but each frequency produces a different gain (Hussey *et al.*, 2000). During routine operation (“common time”), the radar scans through 16 beams to form an $\sim 52^\circ$ azimuthal field of view, once every minute or two. Beam steering is accomplished electronically using an analog phasing matrix.

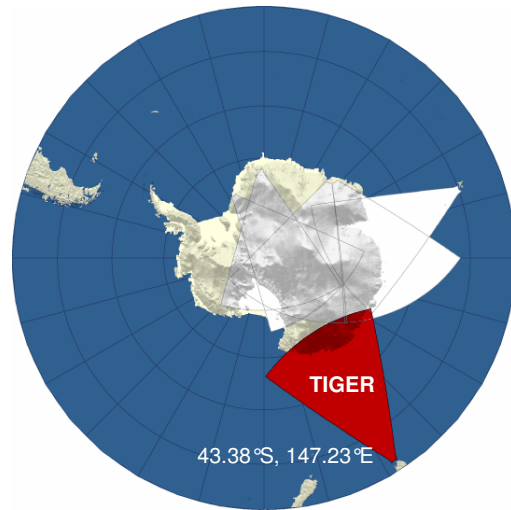


Figure 2.2: Location of SuperDARN radars in the Southern Hemisphere (courtesy of SuperDARN at JHU).

To obtain a coordinated, global view of the polar ionosphere, all 15 SuperDARN radars operate simultaneously during what is known as “common time”. The experimental programs reported in this thesis were run outside common time, during discretionary time, as required under the agreement which helps to bind all members of the SuperDARN community.

2.4 The Tasman International Geospace Environment Radar (TIGER)

Located on Bruny Island off the south coast of Tasmania (43.38°S , 147.23°E), the Tasman International Geospace Environment Radar (TIGER) (Dyson and Devlin, 2000; Dyson *et al.*, 1999; Dyson *et al.*, 2003) (Figure 2.3) provides an excellent opportunity to study auroral processes at high geomagnetic latitudes. The first radar was installed in 1999, and the development of a second radar at Invercargill, New Zealand, has begun.



Figure 2.3: The 16 log-periodic elements of the TIGER radar and its 4 element sub-array (courtesy of Danny Ratcliffe).

Constructed at La Trobe University, TIGER is based on an existing third generation HF radar design, with overlapping footprints for the mapping of ionospheric motions by the detection of ionospheric scatter.

Signals returned to the radar mainly result from Bragg scattering from ionospheric irregularities and the sea surface, but total reflections are also possible. Radio waves are transmitted at elevation angles such that they arrive perpendicular to near vertical magnetic field lines after undergoing ionospheric refraction. Figure 2.4 shows various propagation modes for the backscattered signal.

TIGER's transmitting antenna consists of 16 log-periodic, 10 element, horizontally polarised antennas, used for both transmission and reception. Maximum radar gain and sensitivity is obtained at 12 MHz, the frequency most often used at night. However, a frequency of 14 MHz is often used at day because of increased electron densities and radio-wave refraction. The antenna horizontal beam width is frequency dependent, but approximately $3-4^\circ$, and an auxiliary receiving array of four antennas forms an interferometer to measure the elevation angle of incoming signals (Milan *et al.*, 1997).

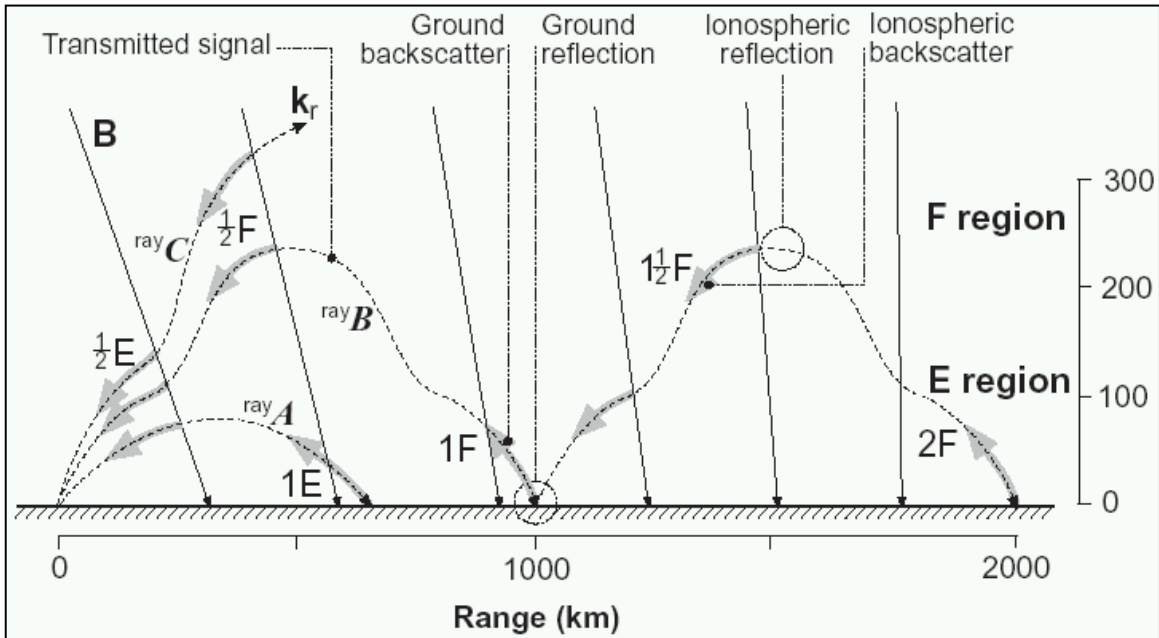


Figure 2.4: Over-the-horizon skywave propagation (courtesy of Steve Milan, 1997).

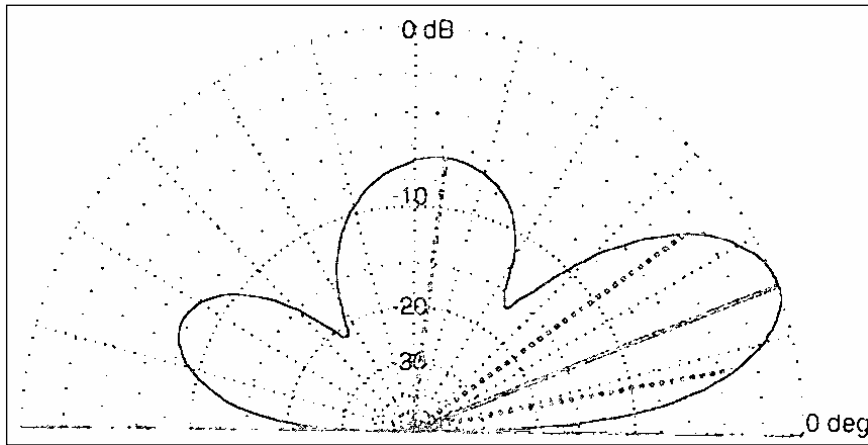


Figure 2.5: Vertical radiation pattern (gain in dB versus elevation angle) at frequency 12 MHz for the log-periodic antennas (from Arnold *et al.*, 2003).

The vertical radiation pattern for the log-periodic antennas is presented in Figure 2.5. The maximum radar sensitivity at 12 MHz is obtained at an elevation angle

of 22° , denoted by the thick solid line. The angles corresponding to the 3-dB gain levels are denoted by dashed lines. The largest side lobe is indicated by the dashed-dotted line (Arnold *et al.*, 2003).

Like all SuperDARN radars, TIGER transmits a sequence of pulses at difference spacings which are multiples of the basic lag length, τ . The 7-pulse sequence used by the radars is

shown in Figure 2.6, which also illustrates how lags in the autocorrelation function (ACF) between 1τ and 27τ can be constructed. At present $\tau=2400\ \mu\text{s}$ is used, so the duration of a pulse set is $\sim 100\ \text{ms}$. All pulses have a duration of $\sim 100, 200, \text{ or } 300\ \mu\text{s}$ corresponding to range resolutions of 15, 30, or 45 km.

ACFs of the echoes at each range are calculated and averaged over the integration time; this “raw” data is stored in *.dat* files. Integration times of 3 or 7 seconds are commonly used for ionospheric studies. Hence during a 7-sec sounding, ~ 70 multi-pulse sequences are transmitted. However, averaging over such long integration times is not ideal for detecting meteor trails with life times of $\sim 0.5\text{-sec}$ (Hussey *et al.*, 2000).

The ACFs are also analysed in near real time using the “FITACF” algorithm, and the results are stored in *.fit* files. Data stored within the *.fit* files are used to generate the summary plots shown in subsequent chapters. These plots reveal changes in the key echo parameters including backscatter power (dB), line-of-sight (LOS) Doppler velocity (m s^{-1}), spectral width (m s^{-1}), and elevation angle ($^\circ$). The latter is determined by cross-correlating the echoes recorded on the main antenna array and the interferometer sub-array.

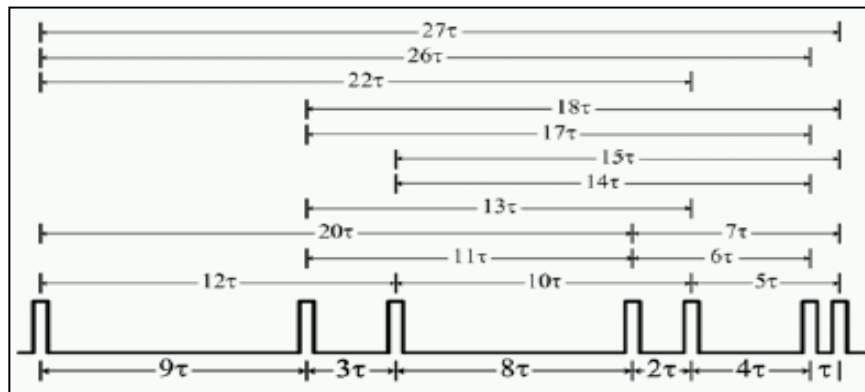


Figure 2.6: The pulse set currently used by the SuperDARN radars (from Dyson *et al.*, 2003).

Estimates of the number of meteor echoes recorded each hour were obtained from the “*number of averages*” (i.e., the number of identified meteor scatter points) contained within *.met* files (see Appendix A). These files are created from ACF *.fit* files by the C language analysis program “*Meteor_Proc*” written by brilliant scientists at the British Antarctic Survey (BAS). The program was written to estimate hourly average mesospheric winds using the beam-swinging technique. Table 2.0 gives the selection criteria for the acceptance or rejection of

Table 2.0: Default criteria used to select meteor echoes in *Meteor_Proc*.

echoes in this program. These criteria will not necessarily reject all of the ionospheric echoes, especially the E-region echoes which sometimes occur in the nearest range gates. Moreover, as will be seen, a vast number of meteor echoes occur beyond range gate 4 (360 km), and many also occur with unusually large spectral widths.

Parameter	Default
Minimum power	3 dB
Maximum range gate	4
Maximum LOS velocity	100 m s ⁻¹
Maximum velocity error	50 m s ⁻¹
Maximum spectral width (recommended)	25 m s ⁻¹

2.5 Characteristics of SuperDARN Meteor Echoes

SuperDARN radars observe a population of echoes below range ~500 km that are present regardless of magnetic activity and its affect on the production of ionospheric irregularities. These grainy near range echoes (GNREs) (Hall *et al.*, 1997) appear continuously on data plots over 24 hours, but with peak intensity near local dawn and minimum intensity near local dusk, as expected for echoes from meteor trails. This diurnal pattern is similar to the behaviour of meteors, and investigations by Hall *et al.*, (1997) confirmed that in fact SuperDARN radars received signals backscattered off ablating meteors. Meteor echoes observed within the first range gates of a SuperDARN radar (<500 km) are often characterised by lower spectral widths than echoes backscattered from plasma irregularities in the E region of ionosphere.

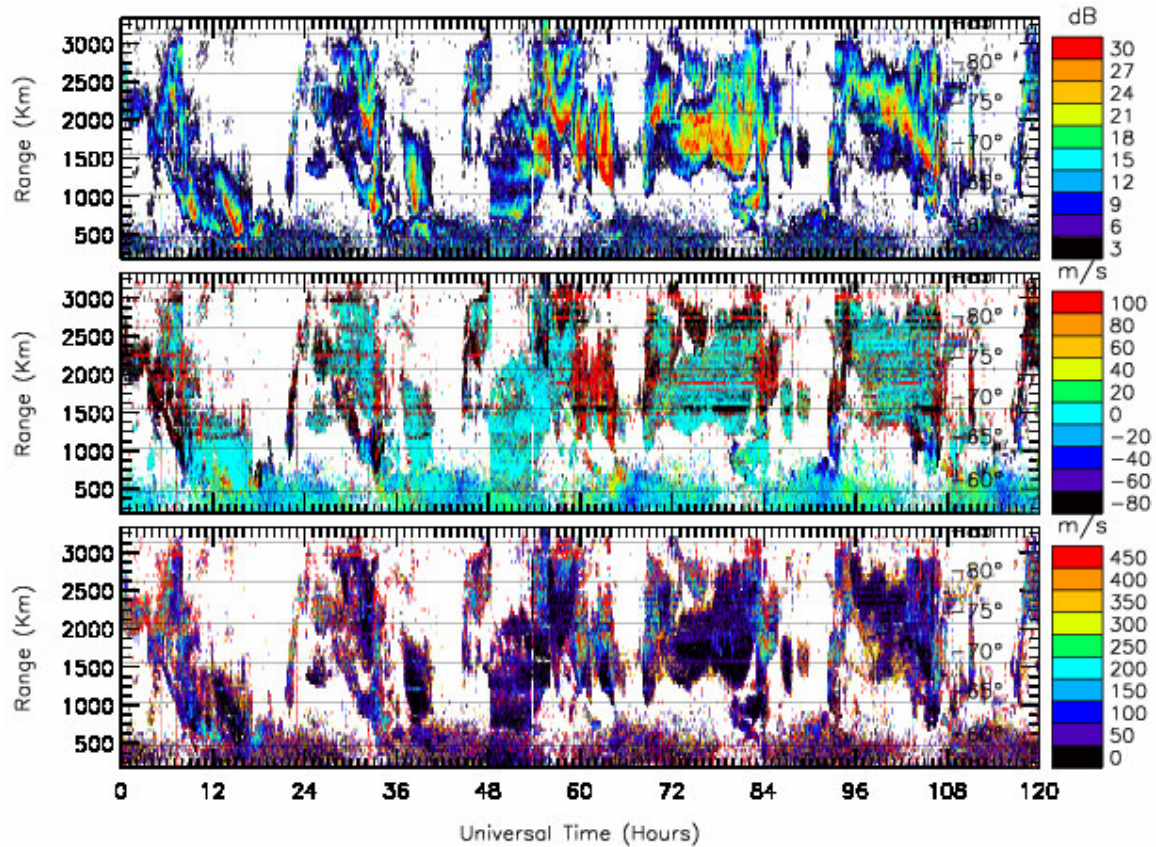


Figure 2.7: Summary plot of all *MSI* echoes (see Chapter 4) recorded at 14,350 kHz on beam 7 during 00 UT, 6 March to 00 UT, 11 March, 2003. The top panel shows the backscatter power (dB), the middle panel the LOS Doppler velocity (m s^{-1}), and the bottom panel the Doppler spectral widths (m s^{-1}).

Figure 2.7 shows GNREs recorded during the *Meteor_Scan1* campaign (Chapter 4) during 00 UT on 6 March to 00 UT on 11 March, 2003. Most of the meteor echoes were detected at group ranges <700 km, and they are characterised by backscatter power, LOS Doppler velocity, and spectral widths lower than those generally observed for ionospheric echoes.

SuperDARN radars were not designed to detect meteor echoes. However, by adjusting the radar control program (RCP) parameters the detection rate of meteors can be enhanced. As explained, the study of meteor echoes is important because they provide a tracer for the neutral winds and other conditions of the mesosphere-lower thermosphere region. The backscattered radar pulses are Doppler shifted by the neutral winds, which constantly change because of gravity waves, planetary waves, and tides. By combining

the LOS Doppler velocities from all 16 beams, the full horizontal wind vector can be estimated at the height of the meteor trails.

The intensity of the backscattered radar signal will be proportional to the square of the electron line density of the meteor trail, where a critical line density used to help classify meteors is $\sim 10^{14}$ electrons per metre of meteor trail length. Three main types of meteors are observed: overdense, underdense, and the overdense-underdense transition type. Overdense echoes have electron line densities that exceed the critical limit such that the ionisation column is sufficiently dense to totally reflect the incident radar beam. These kind of echoes constitute $\sim 1\%$ of all meteor echoes (Hall *et al.*, 1997). Underdense meteor echo line densities fall below the critical limit, and last for less than 1-sec at HF. Most of the observed meteors are the overdense-underdense transition type, characterised by overdense magnitudes and electron line densities, but with a sudden rapid rise time that is characteristic of underdense meteor echoes.

The rise time of an echo is determined by the speed of the meteor creating the ionisation trail, and for typical meteor speed of $30\text{--}40 \text{ km s}^{-1}$, this portion of echo lasts $\sim 100\text{--}200$ ms (Hall *et al.*, 1997). The backscattered power of the meteor decays exponentially as the half-width of the meteor trail increases due to diffusion, as represented by the following equation (see Hall *et al.*, 1997; Arnold *et al.*, 2001):

$$P(t) = P_0 \exp\left(\frac{-t}{\tau}\right) \quad (2.0)$$

Here τ is the decay constant and is given by Equation 2.1 where D is the diffusion coefficient and λ is the radar wavelength.

$$\tau = \frac{\lambda^2}{32\pi^2 D} \quad (2.1)$$

The diffusion coefficient, D , determines the rate at which meteor echoes decay in the atmosphere, and is given by Equation 2.2 where T_i is the ion temperature, T_e is the electron temperature, ν_{in} is the ion-neutral collision frequency:

$$D \propto \frac{T_e + T_i}{v_{in}} \quad (2.2)$$

In the thermosphere, $T_e + T_i$ increases with height, and v_{in} decreases with height. Diffusion coefficients change from $\sim 3 \text{ m}^2 \text{ s}^{-1}$ near 90 km to over $20 \text{ m}^2 \text{ s}^{-1}$ around 100 km.

The average power, mean Doppler velocity, and spectral width are determined by FITACF using the ACF averaged over the integration time at every group range. The Doppler spectral width of an echo, Δv in m s^{-1} , can be expressed in terms of the decay constant (Equation 2.0), or the life time of the irregularity, τ .

$$\Delta v = \frac{\lambda}{4\pi\tau} = \frac{8\pi D}{\lambda} \quad (2.3)$$

Thus we expect FITACF will measure larger spectral widths at greater heights, and if sufficiently accurate, the spectral width measurements will also contain information about thermospheric temperature.

To date, a principal limitation on the merit of SuperDARN meteor data has been the lack of detailed information about the altitude distribution of echoes. A statistical inter-comparison of the Saskatoon SuperDARN radar data with equivalent data from the Saskatoon meteor radar by (Hall *et al.*, 1997) could only restrict the possible effective altitude range to the region between 80–100 km, and was performed using a simple static atmosphere (i.e., no variation neutral density with time).

The variation in spectral width with temperature was investigated by Arnold *et al.*, (2001). They determined the mean spectral width shifted to high values at further ranges, as many weaker signals were lost at lower altitudes. Assuming the relationship between ambipolar diffusion coefficient and height derived by Greenhow and Neufeld (1955) applied equally to spectral width, they determined effective meteor heights of 93 and 95 km during the day and night, respectively

Because of inadequate time resolution, TIGER is not yet capable of determining the sudden rise and gradual decay of overdense-underdense meteor echoes. Sessai Yukimatu at the National Institute of Polar Research, Japan, is presently developing a C program to run on the radars and extract high time resolution in-phase and quadrature samples of the echoes (Yukimatu and Tsutsumi, 2002). The analysis will facilitate identification of the different meteor echo types, permit the collection of echoes at ranges <180 km, improve the effective height resolution, yet exclude directional ambiguities associated with the back lobe.

In summary, the characteristics of meteor echoes have been investigated by Jenkins *et al.*, (1998), Arnold *et al.*, (2001, 2003), and Yukimatu *et al.*, (2002). Table 2.1 lists the currently accepted characteristics of SuperDARN meteor echoes. This study aims to review and improve upon these parameters.

Table 2.1: Accepted meteor echo characteristics.

Characteristic	Accepted Values
Power	3–24 dB
LOS Doppler velocity	$\pm 40 \text{ m s}^{-1}$
Spectral width	> 1 and $< 50 \text{ m s}^{-1}$
Elevation angle	N/A °
Altitude	90–110 km
Range	<500 km

2.6 Optimising Meteor Echo Detection Rates

The detection of meteor echoes using SuperDARN HF backscatter radars stems from the idea that they can be used to investigate winds, gravity waves, planetary waves, and tides in the neutral atmosphere. SuperDARN radars were not designed with specifications optimised for the detection of meteor echoes; hence the optimum radar operating parameters and data analysis filtering conditions have yet to be conclusively determined. In this thesis, the operation of TIGER will be optimised for the detection of meteor echoes and a set of filtering criteria established to build upon those established by earlier meteor studies (Hall *et al.*, 1997; Jenkins *et al.*, 1998; Arnold *et al.*, 2001, 2003).

An investigation into the optimum radar operating frequency for the detection of meteor echoes was conducted. The optimum radar operating parameters determined from this and subsequent discretionary campaigns might be applied to future SuperDARN meteor campaigns which will ultimately be used to monitor the behaviour of mesospheric winds on global scales.

Some of the earlier studies have restricted the group range of meteor echoes to below 360 km. However, it will be shown that TIGER probably detects meteors out to ranges as great as 800 km. Numerous ionospheric echoes contaminate the GNREs at these further ranges, so it is very important to determine the characteristics which can be used to distinguish between the two kinds of echoes.

Summary plots were produced to provide a first qualitative indication of meteor echo characteristics. Normalised probability distribution functions (PDFs) of the echo parameters were then calculated to provide further quantitative detail. Here, PDFs are basically a histogram of the number of occurrences in predefined evenly spaced bins, with every occurrence normalised to the mode value. The mode values of each echo parameter are presented in this thesis. The set of PDFs applicable to meteor echoes should be different to the set of PDFs applicable to ionospheric echoes.

It must be noted that the two receivers for the main and interferometer arrays are yet to be calibrated. Unfortunately, this imposes limitations on the interpretation of the elevation and virtual height results presented in this thesis. Nevertheless the virtual heights, h , of meteor echoes were calculated using the group ranges, r , and interferometer elevation angles, θ .

$$h = \sqrt{R_e^2 + r^2 + R_e^2 r^2 \sin^2(\theta)} - R_e \quad (2.4)$$

This equation was derived using spherical trigonometry, and 6370 km was used for the radius of the Earth.

Chapter 3: “Meteor_Freq,” 1 to 2 March 2003

3.1 Experiment

In this study, TIGER operations were optimized to detect meteor scatter. This required an investigation to determine the appropriate radar transmission frequency. The radar control program “*Vari_Scan.c*” written by Dieter Andre (University of Saskatchewan, Canada) was used for this purpose. This involved editing the text file “*Vari_Scan_Di.rcp*” to produce the “*Meteor_Freq*” (*MF*) measurement parameters (Tables 3.0 and 3.1). The first range, range separation, and pulse width were decreased to 90 km, 15 km, and 15 km respectively, in an effort to detect close range meteor echoes. However an unforeseen error in the software meant that the range separation was left unchanged at 45 km. The time interval over which the radar integrates on a single beam is normally 7 seconds, but

Table 3.0: *Normal_Scan* and *Meteor_Freq* operating parameters

Parameter	<i>Normal_Scan</i>	<i>Meteor_Freq</i>
First range <i>frange</i>	180 km	90 km
Range separation <i>rsep</i>	45 km	45 km
Pulse width <i>txpl</i>	45 km	15 km
Integration time <i>intt</i>	7 sec	2 sec
Day frequency <i>day_freq</i>	14,350 Hz	Table B
Night frequency <i>night_freq</i>	11,650 Hz	Table B

Table 3.1: Day and night frequencies assigned to each beam number.

Index	Day and Night Frequency (kHz)
0	9,040
1	9,400
2	10,100
3	10,600
4	11,400
5	11,650
6	12,050
7	13,410
8	13,800
9	14,350
10	15,100
11	15,600
12	15,800
13	17,410
14	18,030
15	18,168
16	18,900
17	19,020
18	19,800

underdense meteor echo duration is less than 1 second, and so several meteor echoes may occur during 7 seconds. Thus the integration time was reduced to 2-sec to increase the rate at which meteor echoes were detected.

In order to determine the optimum radar operating frequency for meteor detection, *MF* was designed to integrate for 2 seconds on the near meridional beam 7, and sequentially in every licensed frequency band. The chosen frequencies are listed in Table 3.1 and the width of the frequency band was restricted to 100 kHz. Figure 3.0 shows the operating frequencies of all beam 7 soundings made during the campaign.

The information recorded by TIGER will be sorted according to transmission frequency, and analysed. Data recorded at the higher radar frequencies will be used to investigate the descending plasma streams (DPSs) (Figure 3.1) which were also seen to contaminate meteor echoes in *MS1* and *MS2*. The results will ultimately be used to help filter out unwanted echoes in *MS2* data in order to produce a final, quality assured plot of meteor echoes.

3.2 Meteor_Freq Results

The campaign *Meteor_Freq* was run from 00 UT on 1 March to 00 UT on 3 March, 2003. The reduction of pulse width without the corresponding change of range separation was evident from a comparison of the range of echoes observed on previous and successive days. A 45-km range separation was therefore reinstated in the analysis software.

The data and transmission frequency from each beam 7 sounding were stored in *.fit* files enabling the sampling frequency at each frequency to be determined. Figure 3.0 provides a visual measure of the success of transmissions at each frequency, and it can be seen that the density of sampling points was much lower at low frequencies than at high ones. Analyses were therefore performed on frequencies above 11,400 kHz. Figure 3.0 also

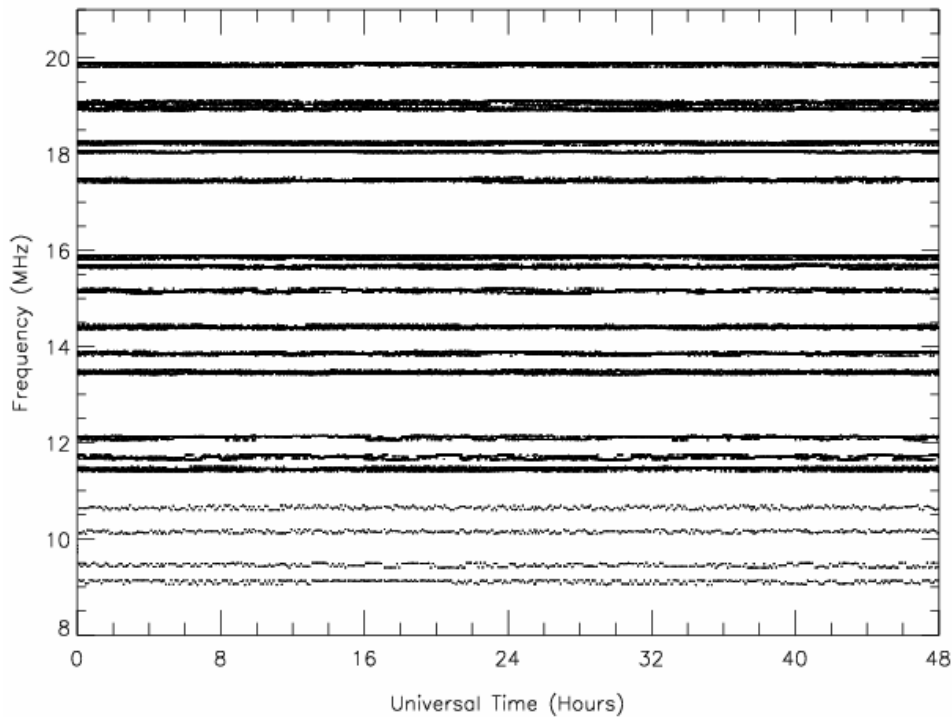


Figure 3.0: Sampling frequencies of each transmission frequency of *MF* during the two campaign days. Low frequencies were recorded at lower sampling rates.

provides an insight into the frequency bandwidth of transmission. At 19 MHz the density of sampling points was high and distributed over a much wider frequency band than was observed for other frequencies, for example, the narrow 12 MHz frequency band.

The operation of TIGER at many frequencies itself made *MF* a novel experiment, but some unexpected results also made it useful for understanding the contamination of meteor echoes by ionospheric scatter. The success of the experiment is clear from the vast amount of echoes recorded in Figure 3.1, a mass plot of the echoes recorded at all frequencies by *MF*. Figure 3.1 also introduces the reader to the overall picture produced by the *MF* experiment. Features extending to ranges of 3000 km are included in this plot to highlight the appearance and origin of ionospheric echoes approaching and merging into ranges corresponding to meteor echoes. As will be seen, similar features were observed during *MS1* and *MS2* campaigns. The characteristics of meteor echoes are not clearly shown in Figure 3.1, hence Figure 3.2 shows the results at frequencies 11,400 kHz to 12,050 kHz, and at group ranges <1700 km only.

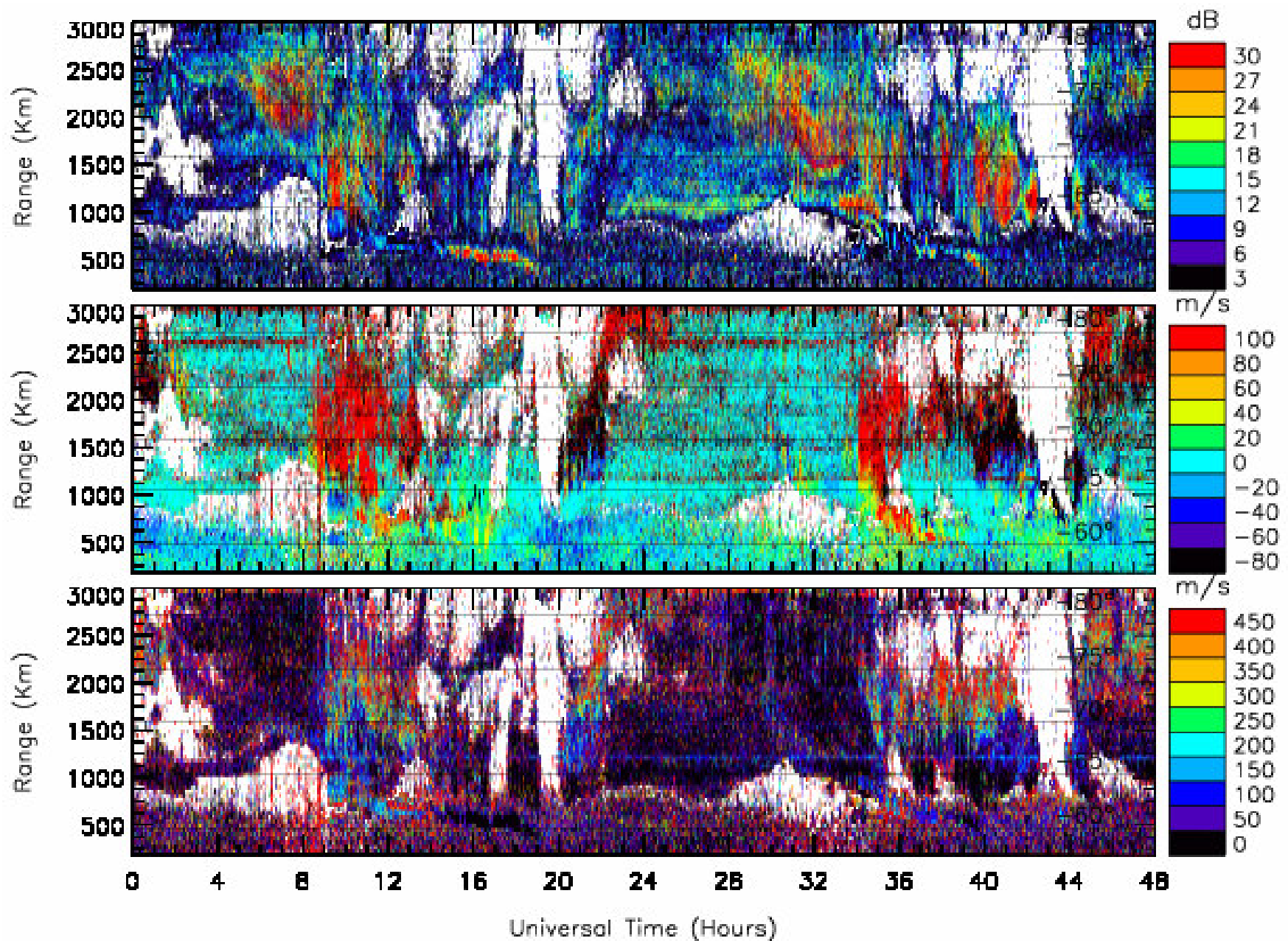


Figure 3.1: Mass summary plot of all MF echoes recorded on beam 7 during 00 UT on 1 March to 00 UT on 3 March 2003. Echoes were recorded concurrently using 19 different frequency bands across the full bandwidth of the radar (see Table 3.1). The top panel shows the backscatter power (dB), the middle panel the LOS Doppler velocity (m s^{-1}), and the bottom panel the Doppler spectral widths (m s^{-1}).

Two significant populations should be considered in Figure 3.1. Below ~700 km the Grainy Near Range Echoes (GNREs) (Hall *et al.*, 1997) dominate, and above 700 km, descending toward the GNRE region, are high powered descending plasma streams (DPSs). While the diurnal variation of the GNREs is no longer evident because of saturation in this particular presentation, significant variations between the results obtained for day and night sounding are apparent.

Commencing at ~09 UT on 1 March, the first DPS appears at 1150 km and over 10 hours descends into the GNREs to as close as ranges of 180 km. Between 14 UT and 20 UT the DPS lies below distributions of streaky low and high powered echoes extending from ranges of 750 km to 1600 km. The second DPS also lasts for ~10 hours, visible from 07 to 17 UT on 2 March (31 to 41 UT), and clearly descends from the higher range ionospheric scatter.

RF interference affects this plot during the same time intervals above, causing some of the DPS and ionospheric echoes to appear with higher spectral widths and Doppler velocities than most echoes.

3.3 Separation of Results According to Frequency

MF data was sorted according to frequency, producing summary plots of greater clarity, as seen in Figure 3.2. Figures 3.2 and 3.3 compare the results obtained in three of the nineteen different frequency bands (11,400, 12,050, and 19,800 kHz), and show that more GNREs were detected at the lower operating frequencies. Appendix B contains summary plots of the data recorded at each frequency, and further illustrates that below 12 MHz, the detection of meteor echoes decreased. As the frequency increased above 12 MHz, the number of detected meteor echoes decreased even more rapidly.

Although the radar gain maximises at 12 MHz, another factor decreased the number of meteor echoes with increasing frequency.

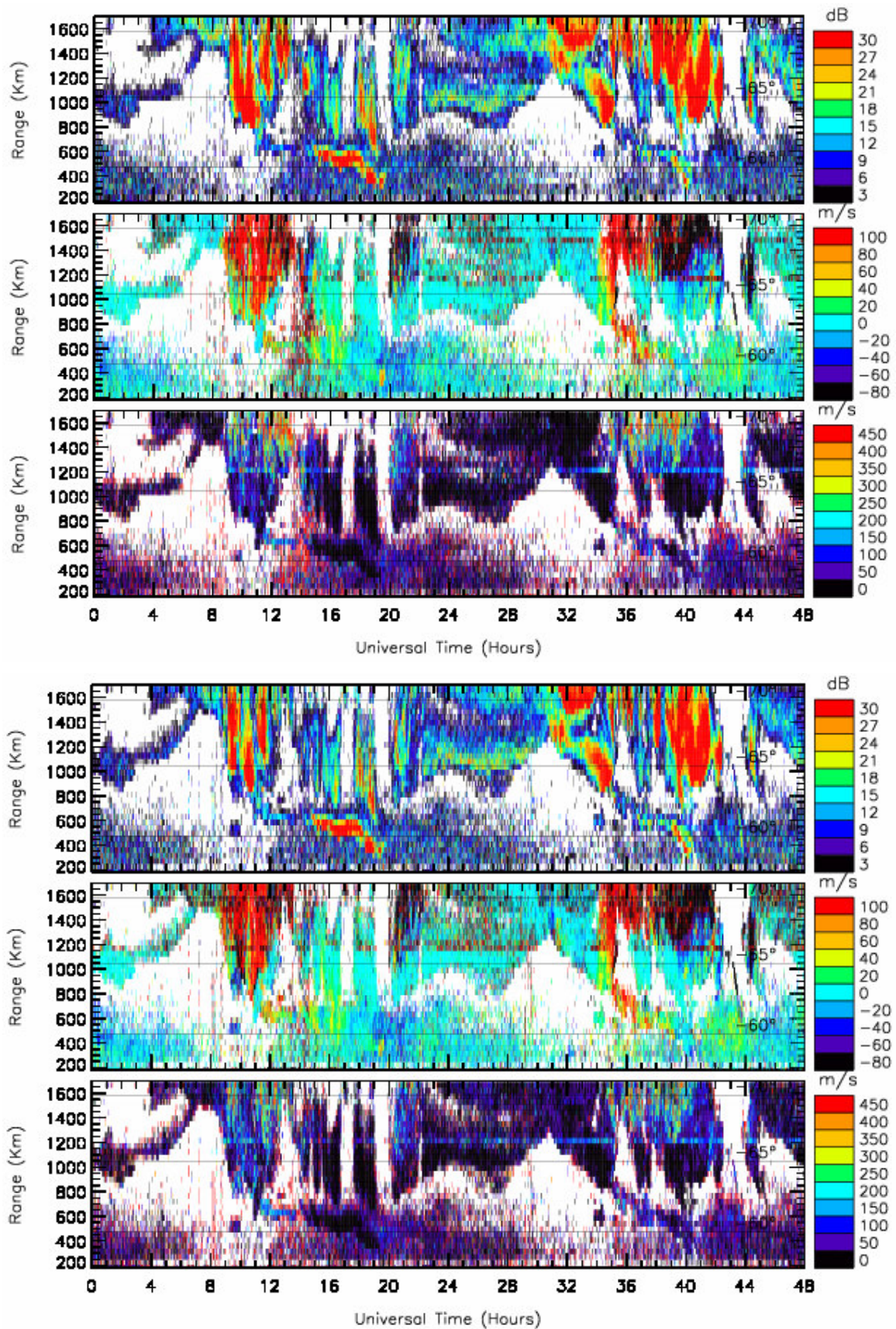


Figure 3.2: (a) Summary plot of TIGER echoes recorded on beam 7 at frequency 11,400 kHz during 00 UT on 1 March to 00 UT on 3 March 2003. The maximum group range was reduced to 1700 km to emphasise details at the ranges of meteor echoes. (b) The same plot as (a) except frequency 12,050 kHz.

The elevation angle of the main radar beam decreased as the radar transmission frequency was increased; therefore only meteor echoes at further ranges were detected, and the numerous echoes at close range echoes were lost.

Some of the ionospheric features shown in Figure 3.2 b were detected at ranges ~ 100 km further than those in Figure 3.2 a, and only the strongest ionospheric echoes persisted at higher frequencies. This is probably because radio waves undergo less refraction at higher frequencies; hence the elevation angle must be lowered to achieve orthogonality of the radio rays with the magnetic field lines. Therefore, ionospheric irregularities will be detected at further ranges and with weaker powers at higher frequencies.

In Figure 3.2 a, a collection of echoes with unusually large spectral widths (600–1000 m s^{-1}) can be seen centred near 14 UT (00 LT), and at every range. These “echoes” were not observed in *MS1* or *MS2*, and are most likely caused by interference from another transmitted.

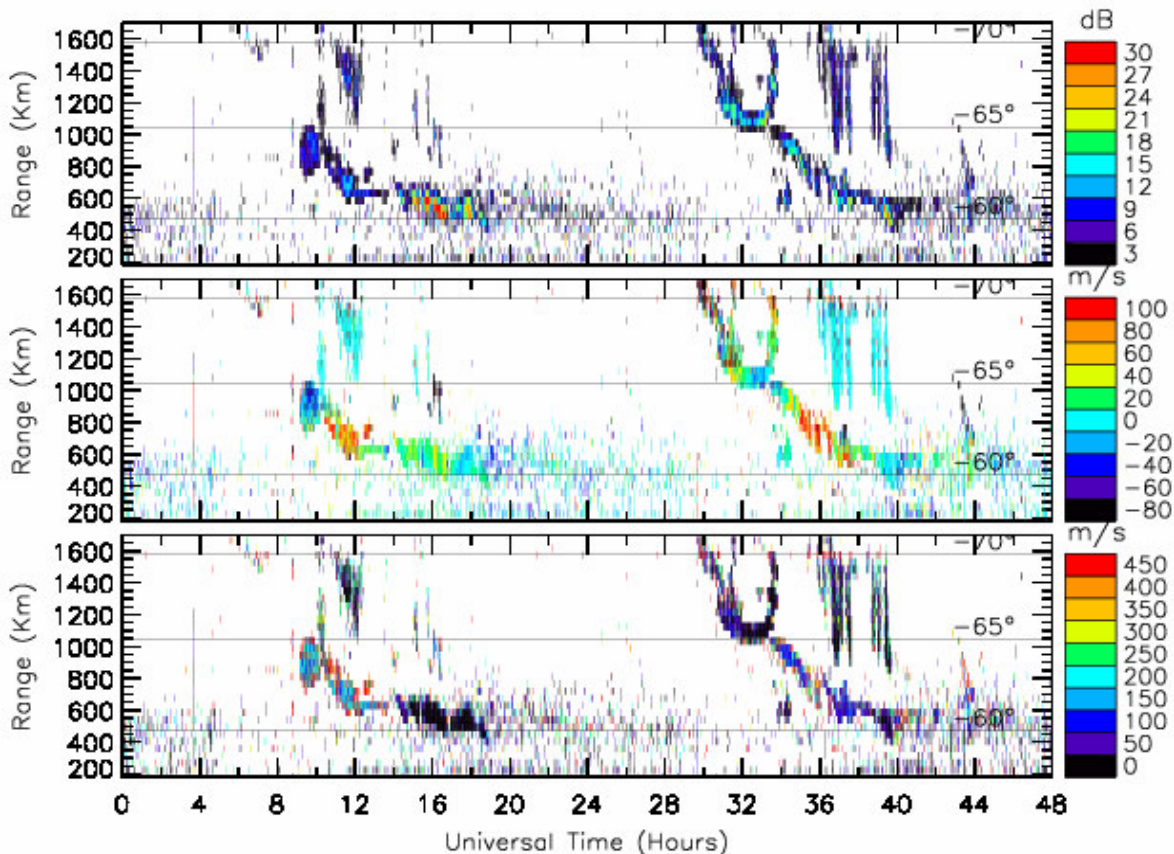


Figure 3.3: Data recorded at 19,800 kHz. Only the high powered echoes are preserved.

3.4 Descending Plasma Streams (DPSs)

The number of ionospheric and meteor echoes recorded at 19.8 MHz (Figure 3.3) was much reduced for reasons explained in the previous section. Figure 3.3 reveals the presence of descending plasma streams (DPS), which are a source of contamination when identifying meteor echoes. An excellent example of one of these features occurs between 30 and 42 UT when it approaches in range until ~500 km, whereupon it disappears amidst the GNREs. Similar features were observed in *MS1* and *MS2*, and it is plausible to assume the same physical explanation(s). The second population of low spectral width echoes maximise near range 500 km, and varies diurnally with small peaks at ~20 UT and 44 UT. This is the familiar dawn peak of GNREs. Their maximum occurrence at range 500 km is higher than generally observed for GNREs, and is a geometrical effect due to changes in the vertical antenna pattern.

The echoes contaminating the meteor scatter were investigated further to determine their characteristics, thus ultimately helping to filter them from meteor echo plots. Two DPS events can be seen in Figure 3.3 commencing at ~09 UT and 30 UT (7 pm LT and 4 pm LT), and ending at 19 UT and 42 UT (5 am LT and 4 am LT), respectively. The 19.8 MHz results shown in Figure 3.3 provide an excellent opportunity to study this phenomenon because other scatter with weak power has been filtered away.

The DPS events descend in group range. It must be considered how much of this corresponds to the equatorward expansion of a feature, as opposed to a descent in altitude. TIGER is an oblique looking radar, and simple geometry will show that if an ionospheric layer descends from an altitude of say, 200 to 100 km at range 1000 km, this change cannot be detected using 45-km range steps. However, large changes in layer height will be discerned at the nearest ranges. We conclude that most of the descent in group range corresponds to the equatorward expansion of some feature with intense irregularities.

During the first DPS, scatter was observed between ~11 UT and just beyond 12 UT, extending from range 1100 to 1600 km. A similar feature was observed during the second DPS, between 36 UT and 40 UT and range 800 to 1600 km. These echoes have very low Doppler velocity and spectral widths, and are probably sea echoes detected via the ionospheric layers responsible for the DPS events. Interestingly, the scatter exhibits wave-like perturbations, revealed by striations in group range on time scales less than 2 hours. These striations may represent oscillations in the leading edge of the sea echo traces caused by irregularities in the plasma density of DPS events, such as those caused by particle precipitation and atmospheric gravity waves.

3.5 Probability Distribution Functions of DPS Events

The probability distribution functions (PDFs) of the echoes shown in Figure 3.3 were calculated in order to further characterise their properties (as explained in Chapter 2). Figure 3.4 shows the PDFs for the backscatter power (a), LOS Doppler velocity (b), Doppler spectral width (c), elevation angle (d), and virtual heights (e). The PDF for the backscatter power was calculated using 1-dB bins over the range 0 to 30 dB. Two major peaks occur, one at 0.5 dB and the other at 3.5 dB. The peak at 0.5 dB is actually caused by a large number of zero values in the FITACF data files. With all other FITACF parameters, a preponderance of zeroes merely represents poorly determined data which should be ignored. The mode value of 3.5 dB means that the majority of echoes had relatively weak power at 19.8 MHz.

The PDF for Doppler velocity (Figure 3.4 b) peaked at 1.5 m s^{-1} , and was clearly positively skewed, indicating there were more positive than negative Doppler velocities, consistent with the equatorward expansion of the DPSs. The PDF for the spectral width (Figure 3.4 c) shows a primary peak at 5 m s^{-1} and a secondary peak at $\sim 230 \text{ m s}^{-1}$. Low spectral widths, below 50 m s^{-1} , are expected for meteor echoes, but they are not the dominant feature in Figure 3.3. This suggests the DPS events had characteristically low spectral widths, but the presence of the secondary peak at 230 m s^{-1} implies two different regimes of plasma instability occurred within the DPS.

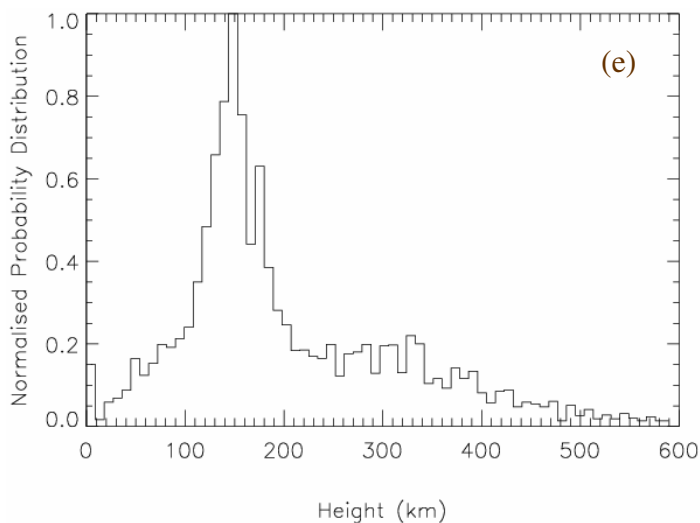
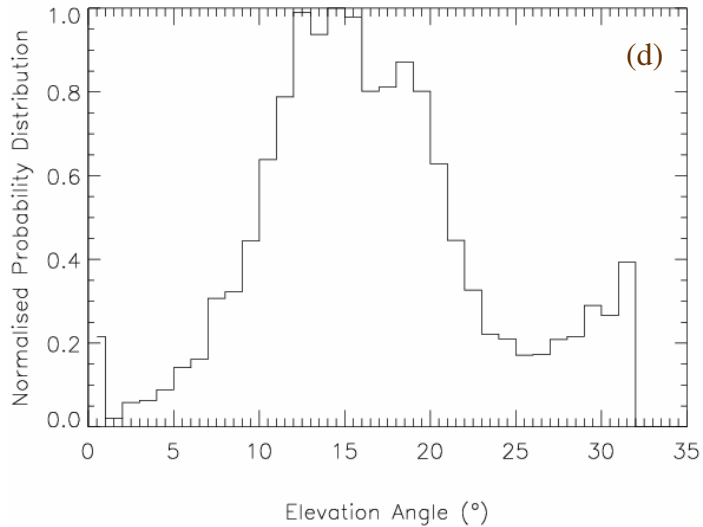
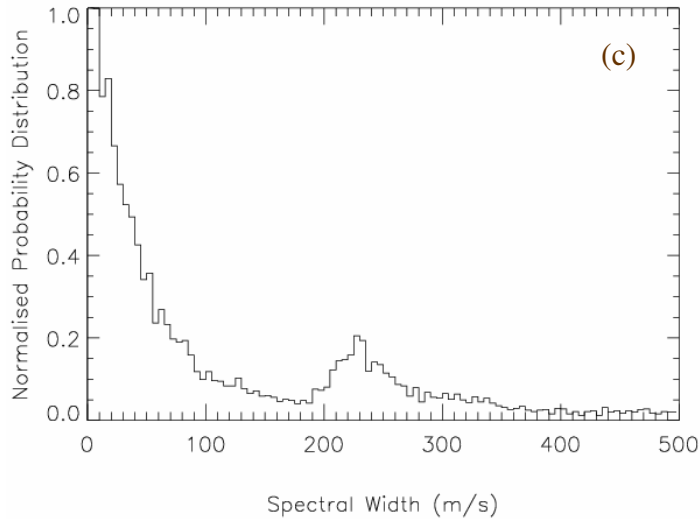
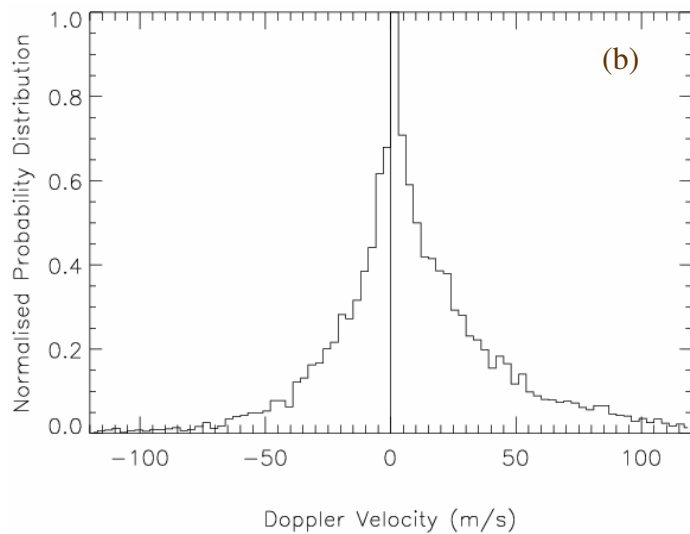
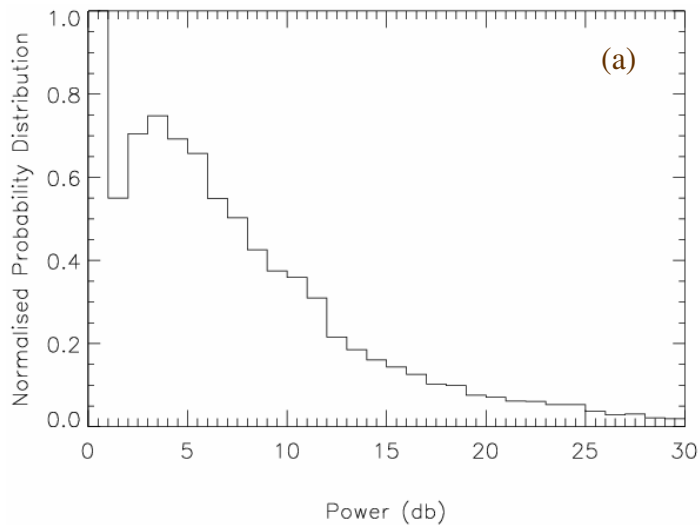


Figure 3.4: Normalised probability distribution functions (PDFs) of echoes recorded on beam 7 at frequency 19800 kHz during 00 UT, 1 March to 00 UT, 3 March 2003. A total of 9,794 Echoes were used to calculate the PDFs for (a) backscatter power (1-dB bins), (b) LOS Doppler velocity (3 m s^{-1} bins), (c) spectral width (5 m s^{-1} bins), (d) elevation angle (1° bins), and (e) virtual height (9 km bins). 10 km bins were not chosen for height as they lacked sufficient detail in the distribution function.

Figure 3.4 d is interesting because it displays opposite behaviour to that observed for the *MS1* and *MS2* elevation angles. Three overlapping distributions may be present; however the distribution with a mode value of $\sim 14^\circ$ was dominant. As before, the peak at 0° indicates poorly determined data, or perhaps even sea echoes observed via HF surface-wave propagation, which is not relevant to this study anyway.

The distribution of corresponding virtual heights, Figure 3.4 e and 3.5, indicates many of the echoes at 19.8 MHz originated from just above the meteor layer, at E-region heights of ~ 150 km. One would normally assume this is too high for meteor echoes, but bearing in mind the high transmission frequency, and concerns about the accuracy of interferometer measurements, some of these echoes might actually be from meteors. Below range 300 km (Figure 3.5), the sprinkling of purple and blue echoes emanate from low virtual heights (~ 40 to 80 km), and are almost certainly meteor echoes.

DPS events were the dominant features in the 19.8 MHz data, Figure 3.3, but some GNREs were also present. The mode values of the PDFs of this data are summarised in Table 3.2. The characteristics of these echoes will be compared with those of meteor echoes in later sections.

Table 3.2: Mode values of DPS echoes measured at frequency 19.8 MHz.

Parameter	Mode Value
Power	~ 3.5 dB
Doppler velocity	~ 1.5 m s ⁻¹
Spectral width	~ 5 and 230 m s ⁻¹
Elevation angle	$\sim 14^\circ, 18^\circ, 32^\circ$
Virtual Height	~ 150 km

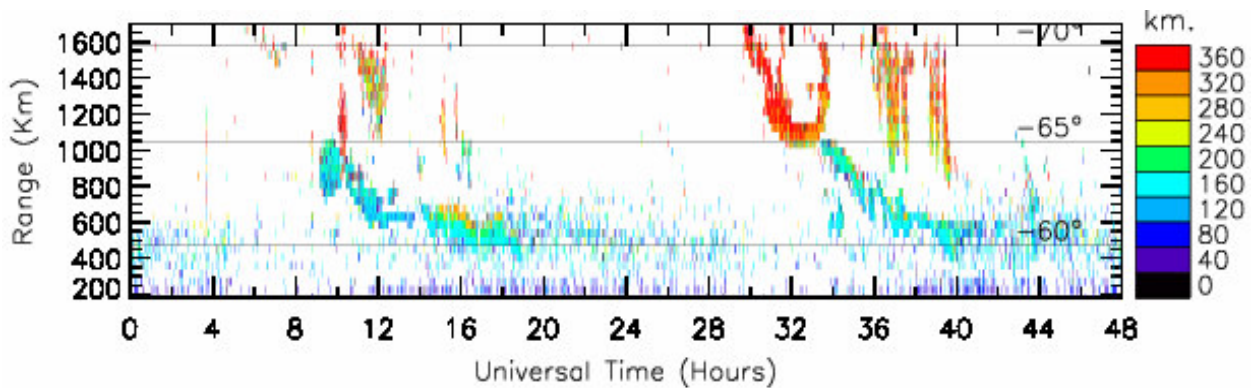


Figure 3.5: Summary plot of virtual heights calculated using elevation angle data recorded at 19,800 kHz. The PDF of this data was shown in Figure 3.4 (e).

3. 6 Echoes Detected at 12 MHz with Spectral Width <50 m s⁻¹

The largest number of meteor echoes were detected at frequency 12 MHz during the *MF* campaign, and meteor echoes are generally thought to have spectral widths less than 50 m s⁻¹. Therefore, the *MF* echoes recorded at 12 MHz with spectral widths <50 m s⁻¹ and between ranges 180 to 800 km were analysed to further characterise the meteor echoes. Figure 3.6 shows the PDFs for this data, presented in the same format as Figure 3.4. The peak in backscatter power was observed at 8 dB. This was somewhat larger than generally observed for meteor echoes, and was probably caused by the intrusion of DPS events which exhibited very high powers (Figure 3.2 b).

A 2 m s⁻¹ Doppler velocity peak was determined (Figure 3.6 b), and overall the PDF was positively skewed. Figure 3.6 c shows the spectral widths had peak occurrence at very low values (<5 m s⁻¹), and gradually decayed towards 50 m s⁻¹. The distribution of elevation angles is interesting because it displays the opposite behaviour to that of Figure 3.4 d. Two distributions are superimposed, a broad one with mode value near 23° and a sharp narrow one centred on 38°. The latter distribution must have corresponding virtual heights too large to be consistent with the detection of meteor echoes. This is supported by the PDFs of virtual heights, Figure 3.4 e. Two main distributions can be seen, a meteor layer distribution with mode ~105 km, and a broader distribution at greater heights with mode ~280 km.

The analysis was performed again with the same constraints, but only using echoes with elevation angles between 1° and 33°. This is because the distribution of echoes with mode value 38° almost certainly emanated from too great an altitude for meteor echoes. The new PDF for the virtual heights is shown in Figure 3.7, and it is evident most of these high altitude echoes were immediately removed. 0° ground scatter was also removed from the data.

Table 3.3: Mode values of meteor echoes detected at frequency 12 MHz.

Parameter	Mode Value
Power	~8 dB
Doppler velocity	~2 m s ⁻¹
Spectral width	<10 m s ⁻¹
Elevation angle	~23°
Virtual Height	105 km

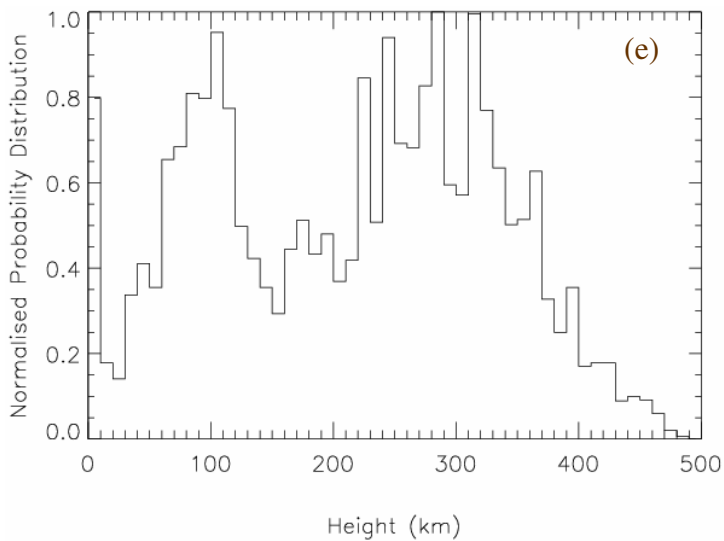
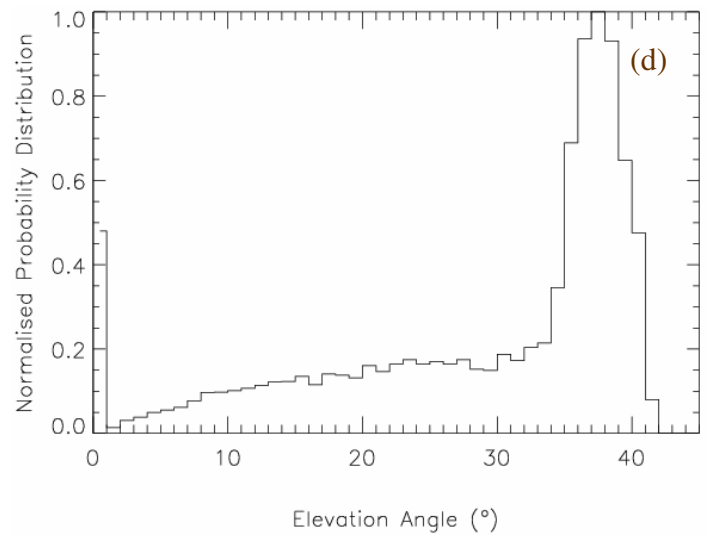
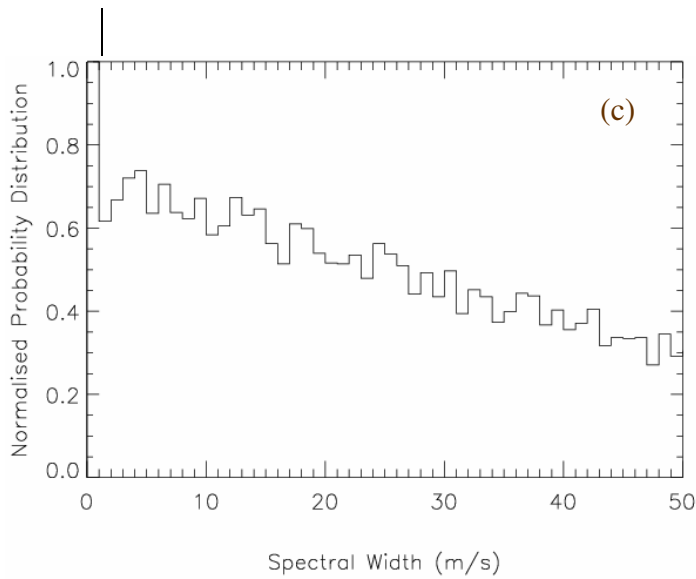
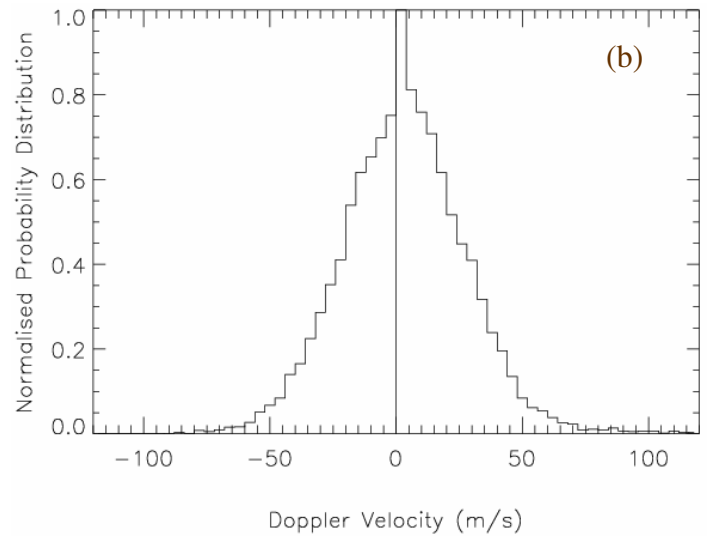
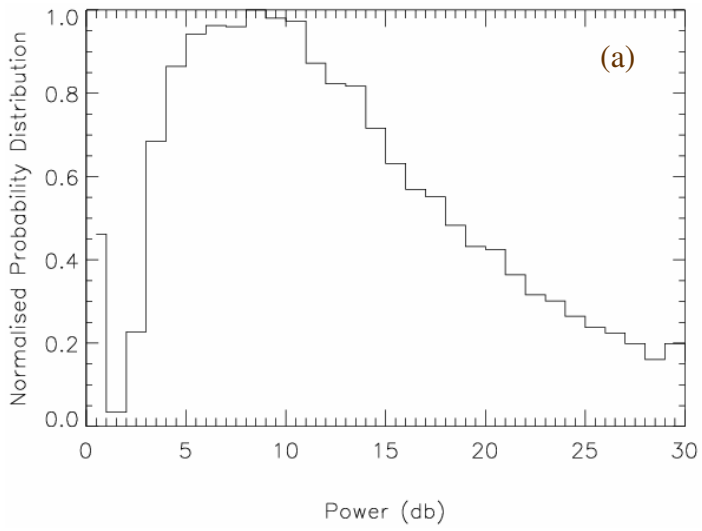


Figure 3.6: PDFs of echoes recorded on beam 7 at frequency 12,050 kHz during 00 UT on 1 March to 00 UT on 3 March 2003. A total of 12,136 Echoes were used to calculate the PDFs for (a) backscatter power (1 dB bins), (b) LOS Doppler velocity (4 m s⁻¹ bins), (c) spectral width (1 m s⁻¹ bins), (d) elevation angle (1 $^{\circ}$ bins), and (e) echo height (10 km bins).

The peak with mode value 110 km remains, more consistent with the expected heights of meteor echoes, though somewhat high. Despite uncertainties about the accuracy of the elevation angles, one can be confident these are meteor echoes, and the final results of this analysis are summarised in Table 3.3.

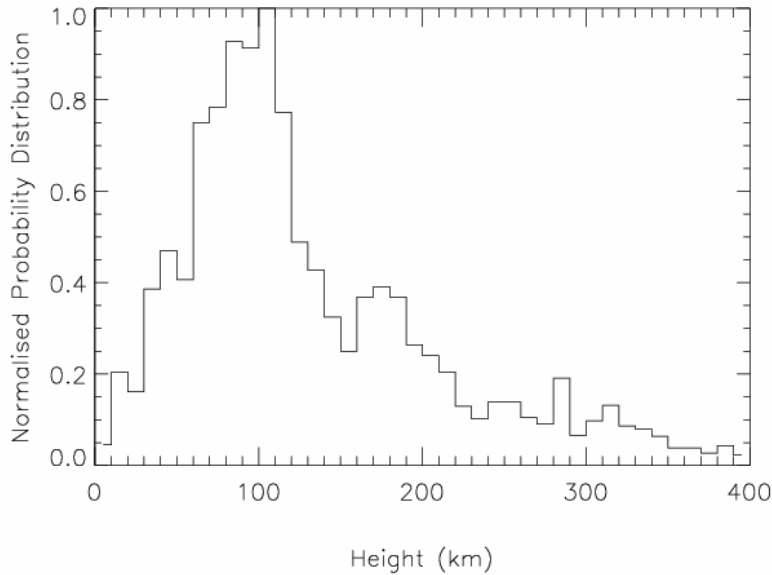


Figure 3.7: Normalised PDF of the virtual height of echoes (10-km bins) recorded on beam 7 at frequency 12,050 kHz during 00 UT on 1 March to 00 UT on 3 March 2003. A total of 7,064 echoes were analysed with spectral width $<50 \text{ m s}^{-1}$, elevation angle $<33^\circ$, and group range $<800 \text{ km}$.

Chapter 4: “Meteor_Scan1,” 6 to 10 March 2003

4.1 Experiment

Like all SuperDARN radars, the design of TIGER was optimised to detect and unambiguously measure the motion of ionospheric irregularities out to ranges of ~3000 km. However most meteor echoes are found to occur closer than 600 km, suggesting TIGER’s ability to detect these echoes could be improved by simple adjustments of the radar operating parameters. Again, Dieter André’s radar control program “Vari_Scan” was used to implement the “Meteor_Scan1” (MS1) measurement parameters (Table 4.0). These parameters were chosen to significantly improve the quality and rate of meteor echo detection. Unfortunately, the bug which affected Meteor_Freq also affected the execution of MS1. Again the range separation was left unchanged at 45 km, even though 15 km was selected. MS1 was run over nearly 4 days in March, namely from 00 UT on 6 March to 00 UT on 8 March UT, and from 08 UT on 8 March to 00 UT on 11 March, 2003.

Table 4.0: *Normal_Scan* and *Meteor_Scan1* operating parameters.

Parameter	<i>Normal_Scan1</i>	<i>Meteor_Scan1</i>
First range <i>frange</i>	180 km	90 km
Range separation <i>resp</i>	45 km	45 km
Pulse width <i>txpl</i>	45 km	15 km
Integration time <i>intt</i>	7 sec	2 sec
Day frequency <i>day_freq</i>	14,350 Hz	14,350 Hz
Night frequency <i>night_freq</i>	11,650 Hz	14,350 Hz

Table 4.1: Beam Sequence

Index	Beam
0	0
1	1
2	2
3	3
4	4
5	5
6	6
7	7
8	8
9	9
10	10
11	11
12	12
13	13
14	14
15	15

Under routine operation, the first range at which SuperDARN radars collect echoes is 180 km. However, many meteor echoes occur at closer ranges. The range separation and pulse width were reduced to 15 km, but as previously explained, only the pulse width actually changed. As with *MF*, the integration time was reduced to 2 sec to better match the integration time of underdense meteor echoes, and thereby measure higher echo detection rates.

MF results were not available before the running of *MS*. Thus 14,350 kHz was chosen for the transmission frequency in order to eliminate the affects of frequency changes in this campaign. A 12 MHz transmission frequency provides optimum radar sensitivity, however classical meteor radars operate at VHF (~30–300 MHz); therefore 14 MHz was a compromise between our knowledge of the radar sensitivity, and the possibility of detecting more echoes at higher frequency. Because a single frequency was used, *MSI* could cycle through all 16 beams (Table 4.1). Estimates of the number of meteor echoes detected each hour were obtained from the *.met* files (refer to Chapter 2 for description of a *.met* file). It will be shown that this TIGER meteor experiment resulted in a significant increase in the detected flux of meteor echoes as compared with the routine operating mode.

4.2 Meteor_Scan1 Results

Figure 4.0 is a mass plot of the entire *MSI* campaign showing echo power (dB), line-of-sight (LOS) Doppler velocity (m s^{-1}), and spectral width (m s^{-1}). Features extending to 3000 km are included to highlight the appearance and origin of ionospheric echoes approaching and merging into ranges corresponding to GNREs. It is also interesting to note the F-region scatter and descending plasma stream (DPS) events have a diurnal variation peaking at ~10 UT, and weakening from the commencement to the conclusion of the campaign. This may be related to declining geomagnetic activity.

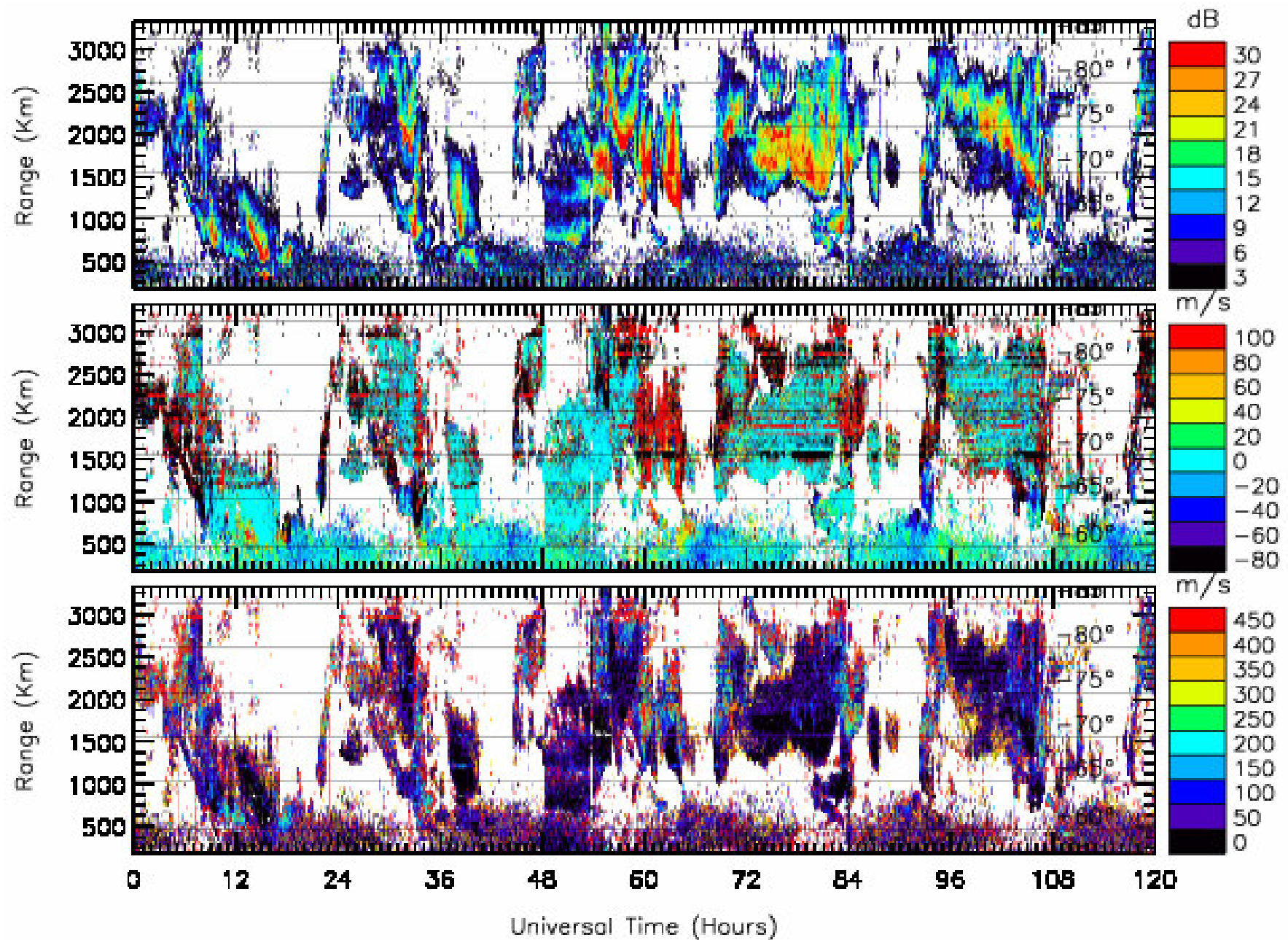


Figure 4.0: Summary plot of all *MSI* echoes recorded at 14,350 KHz on beam 7 during 00 UT, 6 March to 00 UT, 11 March, 2003. The top panel shows the backscatter power (dB), the middle panel the LOS Doppler velocity (m s^{-1}) and the bottom panel the Doppler spectral widths (m s^{-1}).

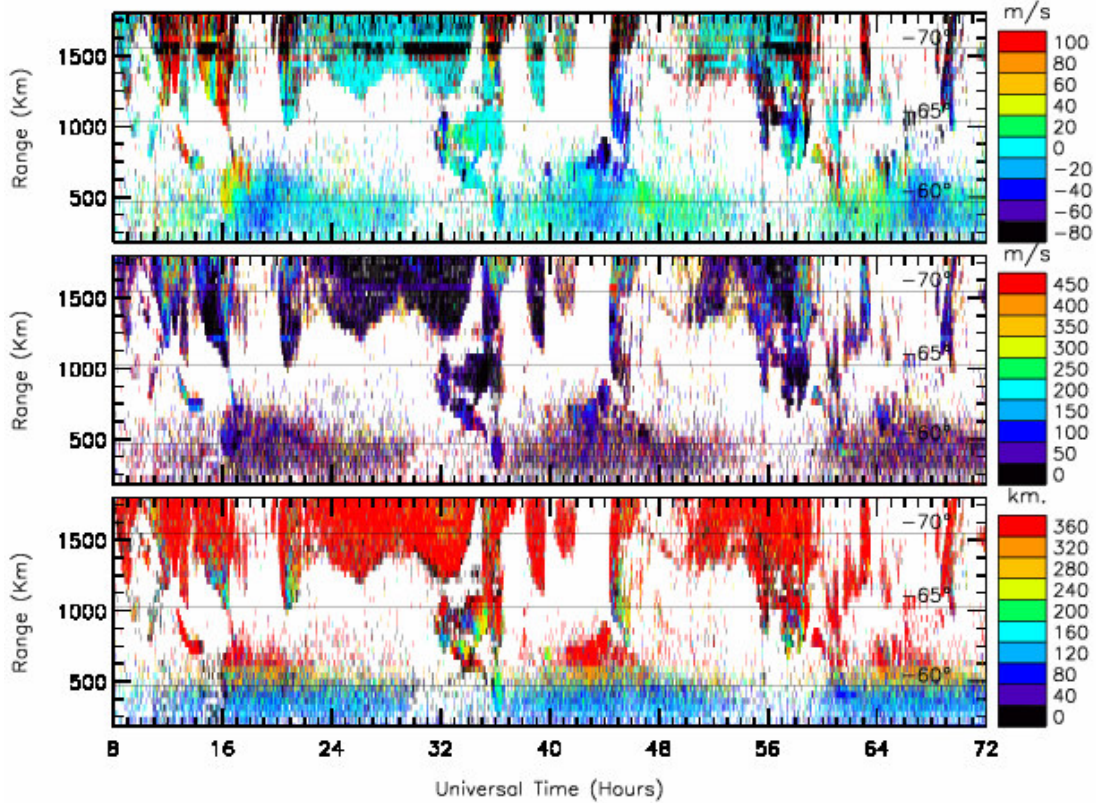


Figure 4.1: Summary plot of *MSI* data recorded during 08 UT on 8 March to 00 UT on 11 March, 2003. LOS Doppler velocity (m s^{-1}), spectral width (m s^{-1}), and virtual height (km) are shown.

The subsequent analysis plots are for the group range intervals 180–1800 km or 180–1000 km, in order to concentrate on the regions where meteor echoes and DPS events were observed. Below range 750 km, the GNREs exhibit a clear diurnal behaviour. Between 00 UT and 08 UT on 8 March the *Fast_Sound* program was run on TIGER. Evidence of this can be seen in Figure 4.0 during this time interval (48 to 56 UT).

Figure 4.1 is an expanded view of the time interval 08 UT on 8 March to 00 UT on 11 March. The LOS Doppler velocities (m s^{-1}), spectral widths (m s^{-1}), and virtual heights (km) are shown for the range interval 180–1800 km. Three DPS events can be seen. These features are not as persistent as they were in *MF* investigations. However, evidence of their existence can be seen between ranges 600–1200 km and between 13 to 18 UT (11 pm to 4 am LT), 32 to 36 UT (6 pm to 10 pm), and 58 to 62 UT (8 pm to 12 am LT). GNREs appear to have Doppler velocities with reasonable values, -50 and 50 m s^{-1} , and

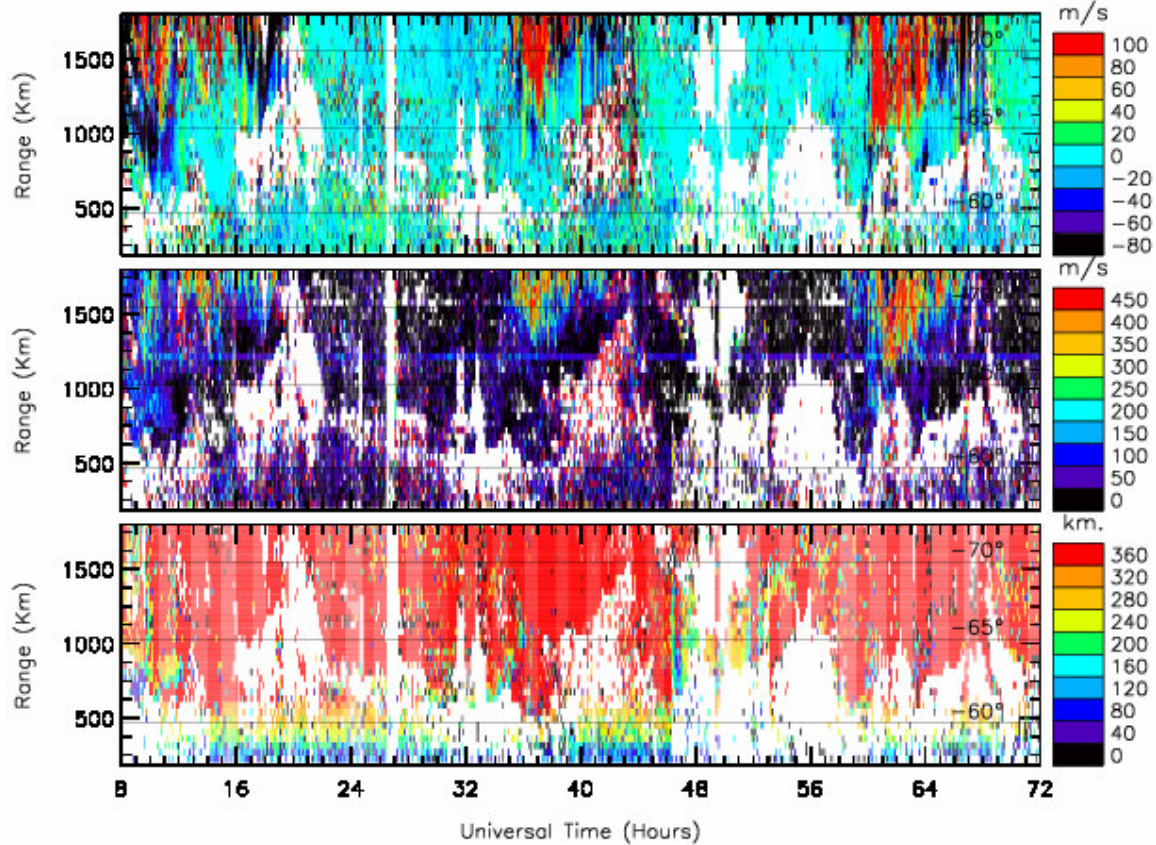


Figure 4.2: Summary plot of data recorded on the days following the *MSI* campaign, namely during 08 UT on 11 March to 00 UT on 14 March, 2003.

spectral widths randomly distributed between 0 and 500 m s^{-1} . Although the accuracy of the interferometer is questionable, we still show the virtual heights (Figure 4.1 e).

Figure 4.2 presents data recorded from 08 UT on 11 March to 00 UT on 14 March, 2003 under *Normal_Sound* and *Fast_Sound* parameters. *MSI* data was compared with data recorded with these routine radar programs to ensure *MSI* parameters improved TIGER's ability to detect meteor echoes. Outages and vertical striations are present in Figure 4.2. Most of the scatter detected appears to be sea scatter, even at close ranges. It can therefore be seen that changes in frequency affected the meteor echo detection rates (Chapter 3). This is further confirmation of *MF* results, and the need to maintain a constant transmission frequency to optimise meteor echo detection rates.

Figure 4.3 a and b present the meteor echo flux observed over the same time intervals as Figure 4.1 and Figure 4.2, respectively. The “number of averages” represents the number of identified meteor scatter points for each hour. A marked increase in the meteor flux in Figure 4.3 a relative to the control interval shows *MSI* fulfilled its main aim of increasing echo detection rates. Caution is required, however, when considering the extent to which meteor scatter detection was improved, particularly after comparing Figures 4.1 and 4.3 a. The meteor echoes may have been contaminated by more DPS events during the *MSI* campaign. For example the largest flux peak in Figure 4.3 a occurs at ~35 UT which corresponds to the arrival of a DPS event at the group range of meteor echoes in Figure 4.1. Although there were clear increases in meteor scatter near dawn, one must be cautious about whether all of the echoes were of meteor origin.

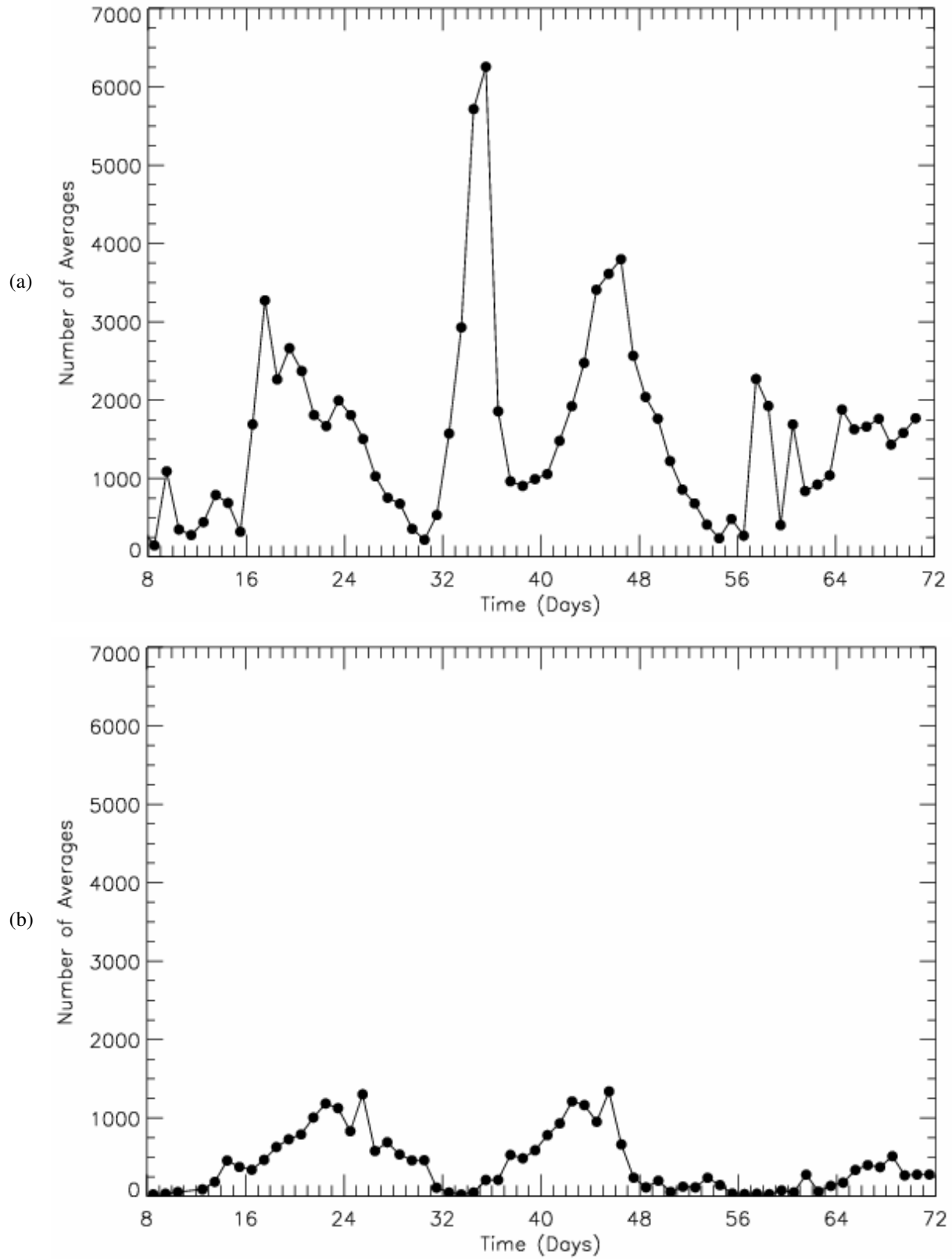


Figure 4.3: (a) *MSI* flux plot for the interval 08 UT on 8 March to 00 on 11 March, 2003. (b) Meteor flux plot for an interval after the *MSI* campaign, 08 UT on 11 March to 00 UT on 14 March.

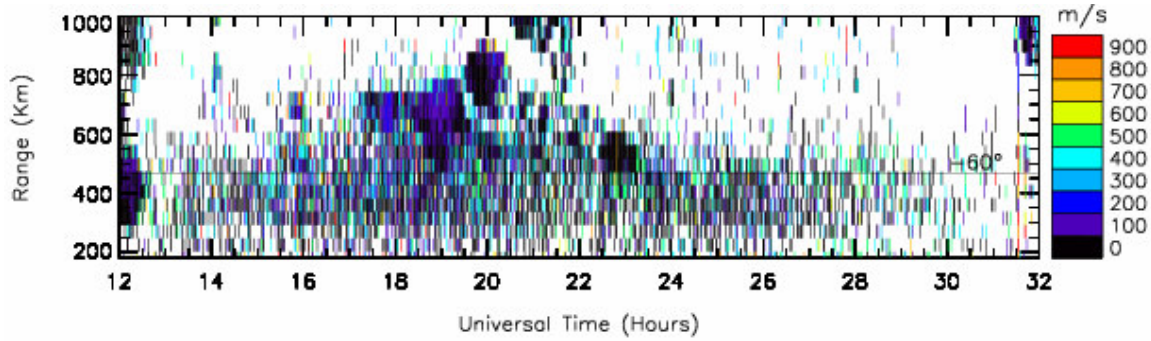


Figure 4.4: Expanded view of Doppler spectral widths recorded from 12 UT on 9 March to 08 UT on 10 March, 2003. Populations of pale blue and green spectral widths are dispersed throughout the meteor scatter.

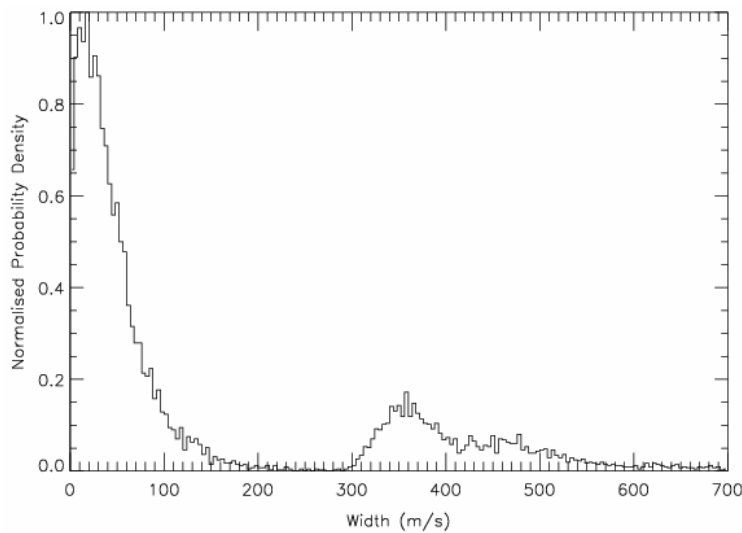


Figure 4.5: Probability distribution function (PDF) of the spectral widths shown in Figure 4.4.

Figure 4.4 is an expanded view of the peak in meteor flux recorded during the *MSI* interval 12 UT on 9 March to 08 UT on 10 March, 2003. Echoes beyond group range 1000 km are not shown, thereby eliminating most 1.0-hop sea echoes and 0.5-hop F-region ionospheric echoes. The spectral width scale was extended to 950 m s^{-1} to illustrate the presence of two different echo populations. There are echoes with high spectral width (green) dispersed amidst echoes with low spectral width (black and purple). Otherwise the characteristics of the echoes with unusually large spectral widths are the same as meteor echoes.

Figure 4.5 shows the probability distribution functions (PDFs) of the spectral widths shown in Figure 4.4. Three distributions are superimposed. The distribution with low

spectral widths and mode value $\sim 18 \text{ m s}^{-1}$ encompasses most of the meteor echoes. However, two other distributions with unusually large spectral widths are present. There is a distribution with mode value $\sim 350 \text{ m s}^{-1}$ followed by a broader distribution ranging to 540 m s^{-1} , after which a long decreasing tail in spectral width was observed.

According to diffusion theory, the mean spectral widths expected for meteor echoes are $10\text{-}25 \text{ m s}^{-1}$ (Arnold et al., 2000). Observations thus far have shown SuperDARN meteor echoes have spectral widths $<50 \text{ m s}^{-1}$ (Hall et al., 1997; Arnold et al., 2003). The meteor echoes with unusually large spectral widths identified here will be discussed further in Chapter 5. The analysis of various features is deferred until the next chapter because it reports measurements obtained with the most refined radar control program of this study.

The E- and F-region ionospheric echoes contaminating the GNREs in Figure 4.4 are closely related to the DPS events discussed in Chapter 3.

4.3 Echoes Recorded at 14 MHz With Spectral Width $<50 \text{ ms}^{-1}$

In Figure 4.6, only the echoes with spectral width $<50 \text{ m s}^{-1}$ have been plotted, thereby removing the aforementioned population of unusually large, and probably erroneous spectral widths. The figure was produced to further investigate the characteristics of meteor echoes, and build upon the knowledge gained from the *MF* campaign, with a view towards the production of a quality assured meteor plot in Chapter 5.

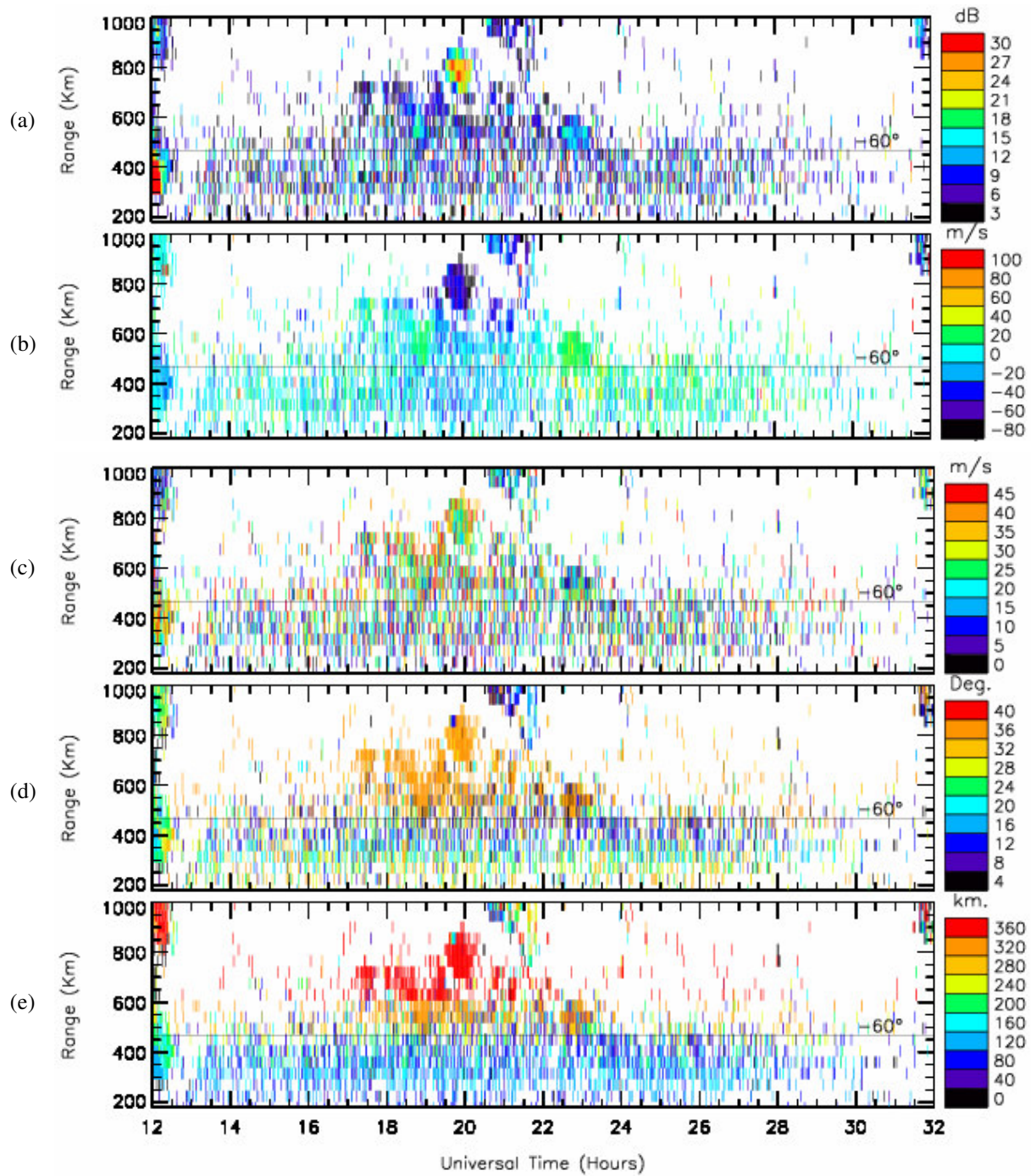
GNREs are an important feature in Figure 4.6. They have characteristically low backscatter powers (a), LOS velocities (b), and spectral widths $<20 \text{ m s}^{-1}$ (c). Their elevation angles also decrease from $\sim 28^\circ$ to 8° over the group range interval ~ 180 to 450 km . The latter corresponds to low virtual heights of 40 to 160 km . However, F-region scatter contaminates the GNREs, mostly between ~ 17 and 23 UT , and at group ranges $>450 \text{ km}$. This F-region scatter is more continuous, and is assumed to be closely related

to the previously identified DPS events. This scatter has larger backscatter power up to ~30 dB (a), low LOS velocities like meteor scatter (b), but slightly greater spectral widths ~25 m s⁻¹. Their most important distinguishing factor is the large elevation angles ~32° to 36°, corresponding to virtual heights from ~280 to >360 km. It is interesting that the virtual heights decrease at closer group ranges, and presumably would have descended to E-region heights at even closer group ranges. This suggests the interferometer measurements can indeed be used to reject F-region echoes contaminating the meteor scatter.

According to Figure 4.6, there was an obvious change in the characteristics of echoes beyond group range ~500 km. This is further illustrated in Figure 4.7, a collection of probability distribution functions comparing the characteristics of echoes detected between ranges 180–400 km and 450–800 km. The PDFs of power for both range intervals (Figure 4.7 a, left and right) show a peak at 3.5 dB with a long descending tail toward higher power. TIGER meteor echoes invariably have low spectral widths; and hence long tail confirms *MF* observations of DPS characteristics.

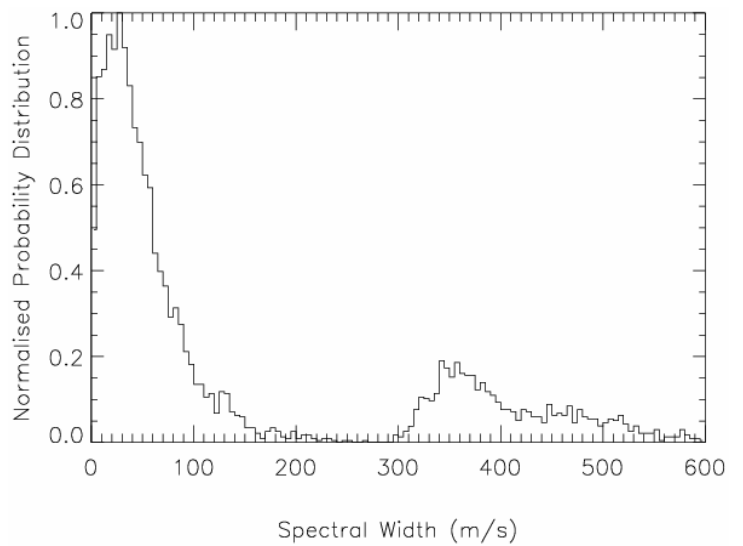
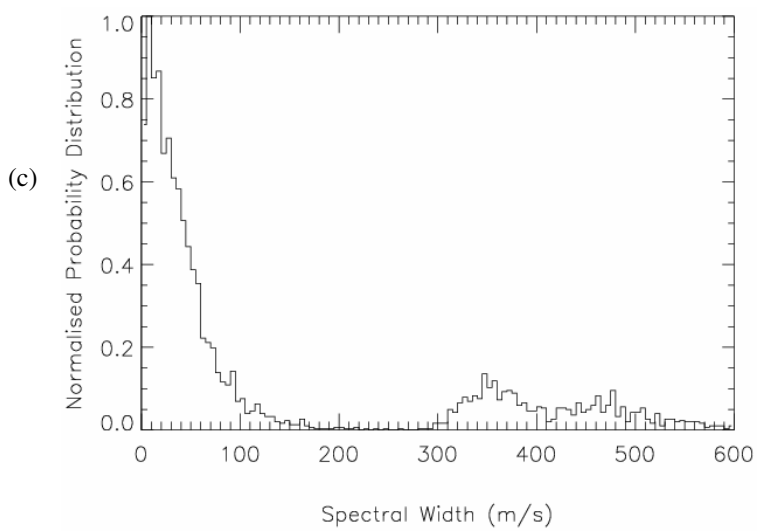
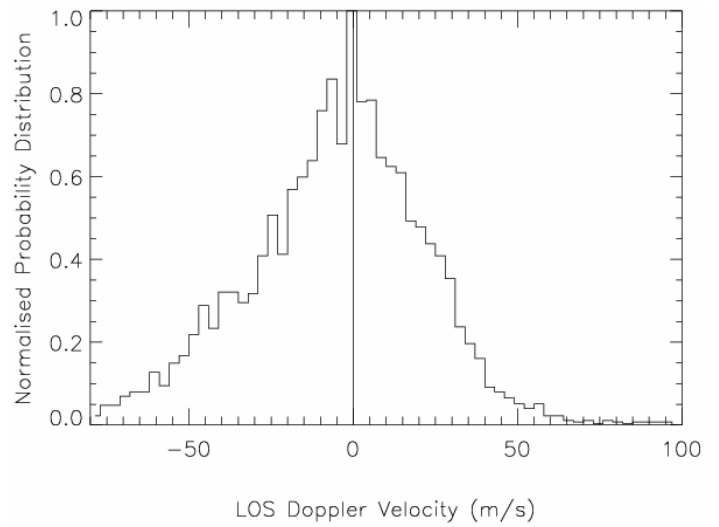
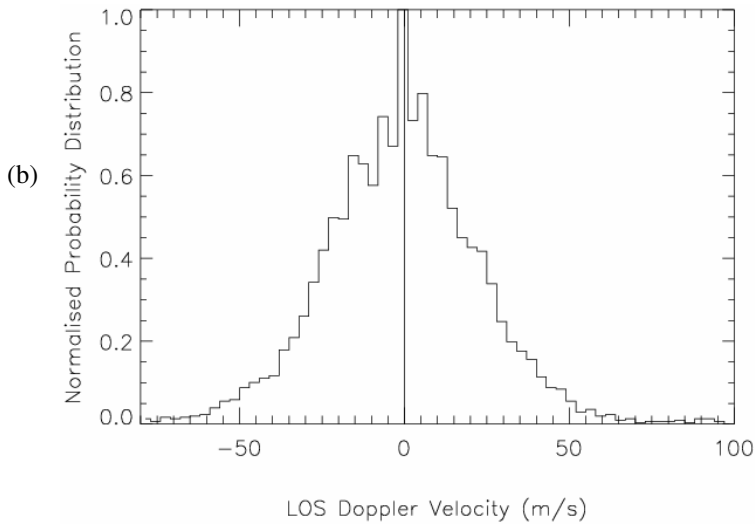
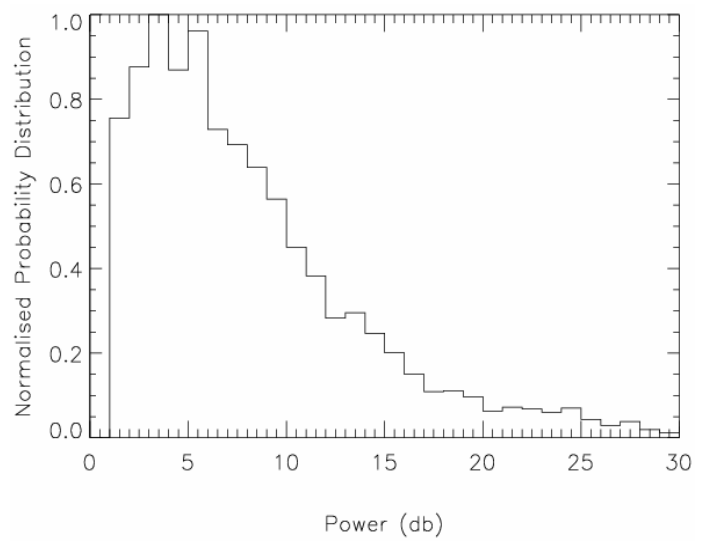
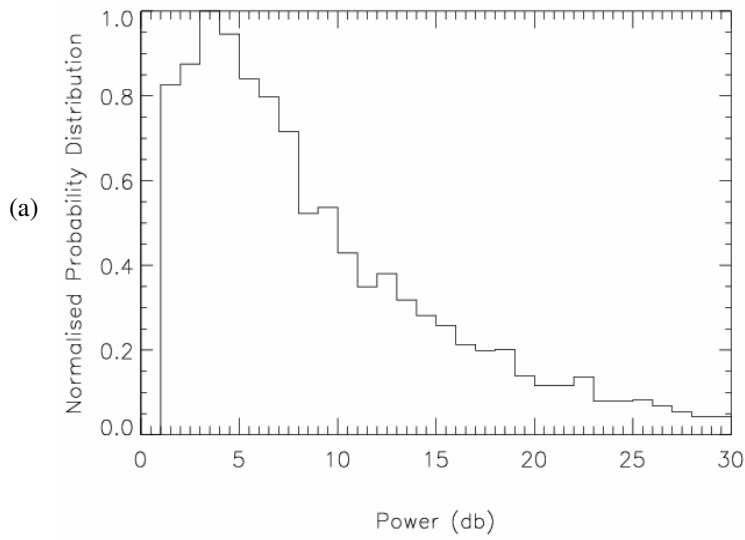
The Doppler velocities presented in Figure 4.7 b do not vary dramatically between the lower and upper group range intervals. The relatively large peak in spectral width at ~10 m s⁻¹ in Figure 4.7 c (left) indicates the presence of numerous meteor echoes between ranges 180 and 450 km. The number of echoes with anomalously large spectral widths of ~360 m s⁻¹ and 460 m s⁻¹ increases relative to the number of meteor echoes with low spectral width in going from near ranges (left) to far ranges (right).

Figure 4.7 d (left and right) are quite different. Between 180 and 450 km the elevation angles are distributed fairly evenly. However, between 450 and 800 km, a major peak was recorded at elevation angles between 33 and 37°. Two distributions can be seen in the corresponding virtual heights, Figure 4.7 e. At closer ranges the 95-km meteor peak dominates, whereas at further ranges ionospheric echoes at E- and F-region heights became more important. As previously shown, these ionospheric echoes tended to be recorded at larger elevation angles.



1

Figure 4.6: Summary plot of echoes with spectral width $< 50 \text{ m s}^{-1}$ detected between 12 UT on 9 March and 08 UT on 10 March. (a) Backscatter power (dB), (b) LOS Doppler velocity (m s^{-1}), (c) spectral width (m s^{-1}), (d) elevation angle ($^\circ$), and (e) virtual height (km)



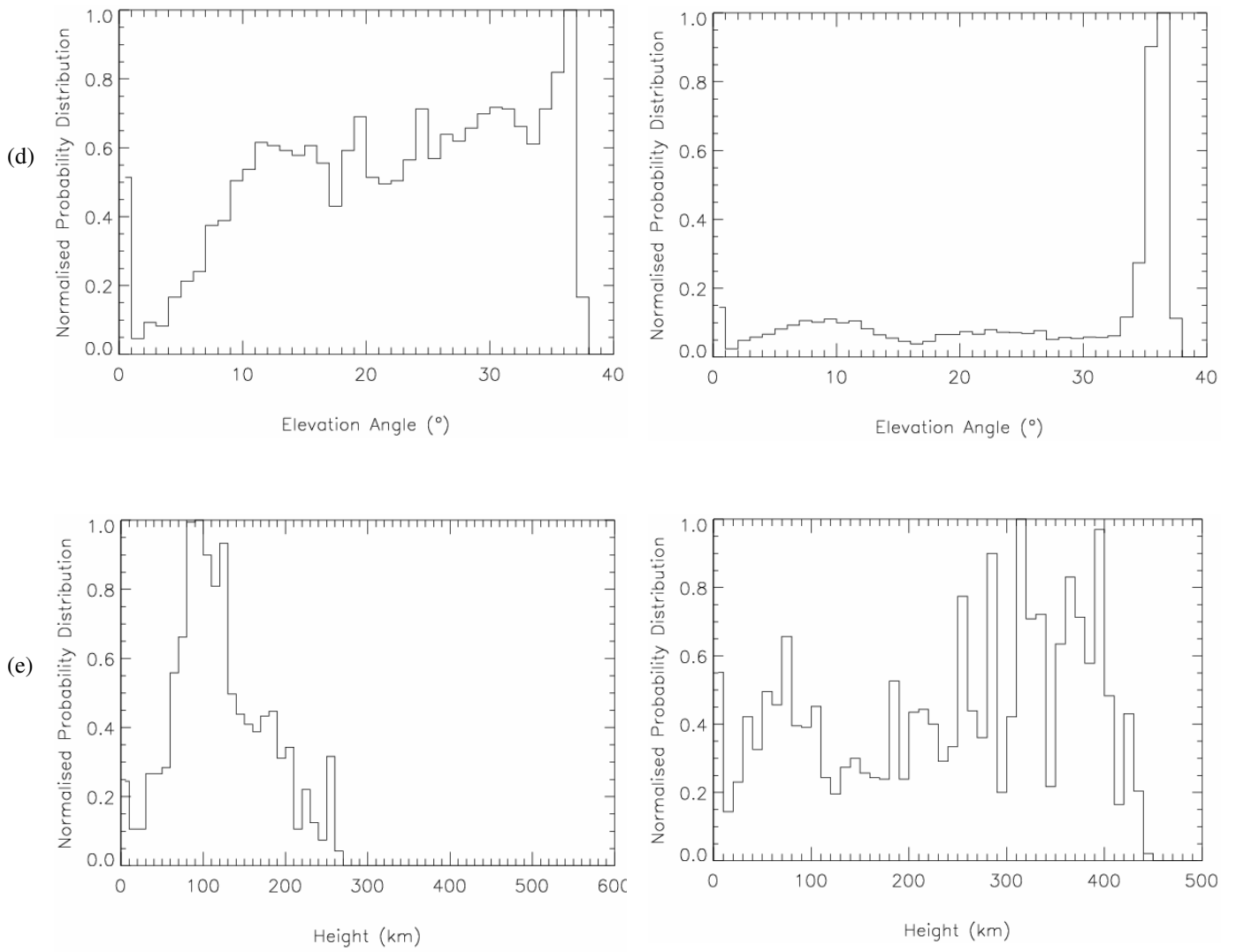


Figure 4.7: PDFs of (a) backscatter power, (b) LOS Doppler velocity, (c) spectral width, (d) elevation angle, and (e) virtual height for group ranges 180–450 km (left column) and 450–800 km (right column).

Chapter 5: “Meteor_Scan2,” 23 to 25 May 2003

5.1 Experiment

The final TIGER meteor campaign, *Meteor_Scan2* (*MS2*), was designed to avoid the shortcomings of *MS1*, and ran from 14 UT on 23 May to 22 UT on 25 May, 2003. Although *MS1* was a successful program, errors in the radar control program *vari_scan* raised questions about the reliability of the data. Therefore, the routine program *fast_scan* was used to implement the *MS2* parameters. The altered and original *fast_scan* parameters are listed in Table 5.0. The integration time was converted from 7-sec to 2-sec, and the pulse width and range separation were successfully changes to 15 km. The first range was decreased to 120 km after TIGER failed to record scatter at lesser ranges during *MS1*. This meant that echoes were recorded out to a maximum range of 1230 km during *MS2*. *MF* results had shown 12 MHz was the optimum day and night radar operating frequency for the detection of meteor echoes (Chapter 3).

The results of analysing *MF*, *MS1*, and *MS2* data will be combined to produce a final quality assured plot, with non-meteor echoes filtered out. The characteristics of these echoes will also be determined and compared to those given by Hall *et al.* (1997) and Arnold *et al.* (2001) (2003).

Table 5.0: *Fast_Scan* and *Meteor_Scan2* operating parameters (all 16 beams).

Parameter	<i>Fast_Scan</i>	<i>Meteor_Scan2</i>
First range <i>frange</i>	180 km	120 km
Range separation <i>rsep</i>	45 km	15 km
Pulse width <i>txpl</i>	45 km	15 km
Integration time <i>intt</i>	7 sec	2 sec
Day frequency <i>day_freq</i>	14,350 Hz	12,050 Hz
Night frequency <i>night_freq</i>	11,650 Hz	12,050 Hz

5.2 “Meteor_Scan2” Results

Figure 5.0 is a summary plot of the entire *MS2* campaign out to range 1200 km displaying the power (dB), line-of-sight (LOS) Doppler velocity (m s^{-1}), and spectral width (m s^{-1}). Overall, the results show a clear diurnal variation of enhanced meteor echo flux, and a decrease in the intensity of descending plasma streams (DPSs) which contaminate the meteor echoes. Figure 5.0 (b) shows the meteor echo Doppler velocities were predominantly between $\pm 40 \text{ m s}^{-1}$. Figure 5.0 (c) shows a significant population of large spectral width scatter (red) below 600 km, otherwise exhibiting the same diurnal behaviour as meteor echoes.

Using *fast_scan* to implement the *MS2* operating parameters did not enable the detection of echoes below range 180 km, suggesting the problem was intrinsic to the radar operating system, and not *vari_scan*. Meteors are known to occur at the D-region altitudes (Arnold *et al.*, 2003); hence they should be detected in near vertical sidelobes of if ranges as low as 80 km can be sampled. Therefore, it must be concluded that a significant population of meteor echoes were not detected in *MS2*.

At high ranges (600–1200 km), there were distinct echo populations with large LOS velocities. They appear to be associated with high-powered echoes occurring at ~29 UT (3 pm LT) and 54 UT (4 pm LT). These features persisted for ~2 hours and emerged at the conclusion of 1.0-hop sea-echo traces. It is not completely certain whether the latter traces were sea echoes because *MS2* was executed with a final range of only 1230 km. However, the traces display characteristics similar to sea echoes, such as high power, ~0 m s^{-1} Doppler velocity, and very low spectral width.

At ~23 UT, there was a marked decrease in the density of GNREs below ~600 km. This coincides with some anomalous echoes with unusually high Doppler velocities, as often occurs during intervals of RF interference. Whence, many meteor echoes with marginal signal-to-noise ratio were lost.

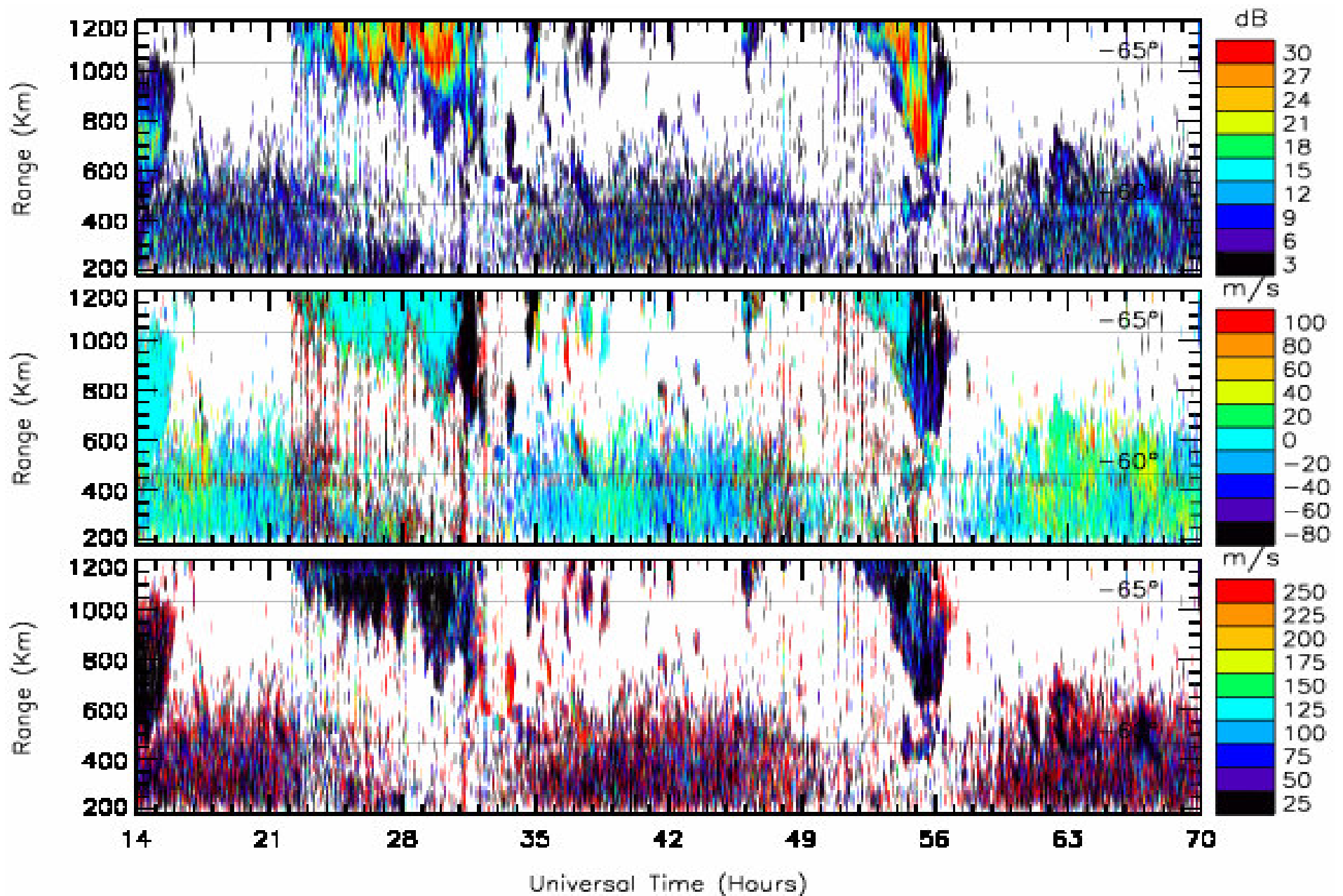


Figure 5.0: Summary plot of all *MS2* echoes recorded at frequency 12,050 kHz on beam 7 during 14 UT on 23 May to 22 UT on 25 May, 2003. The top panel shows the backscatter power (dB), the middle panel the LOS Doppler velocity (m s^{-1}), and the bottom panel the Doppler spectral width (m s^{-1}).

Figure 5.1 (a) and (b) present the “*number of averages*” meteor flux plots for the *MS2* and *MS1* campaigns, respectively. Again, the number of averages is the number of meteor echoes identified each hour, and they were derived from the BAS *.met* files (Chapter 2).

Overall, the area under the curve is greater for Figure 5.1 (a) than Figure 5.1 (b). Hence more meteor echoes were detected at frequency 12 MHz during the *MS2* campaign. Recall that in Chapter 4, the largest peak during the *MS1* campaign (~35 UT) was shown to be caused by a DPS contaminating the meteor echo population. On the other hand, Figure 5.0 suggests that contamination by ionospheric echoes was less important than during the *MS2* campaign.

Finally, note that Figure 5.1 shows peak meteor fluxes of 3000–4000 hour⁻¹ near dawn. However, the program used to estimate the number of averages rejected echoes beyond range gate 4. Thus the true meteor fluxes may have peaked near 6000–8000 hour⁻¹, and even larger if echoes beneath 180 km were recorded.

5.3 Meteor_Scan2 Spectral Width Analysis

Figure 5.2 is a summary plot of all the spectral widths observed during the *MS2* campaign. This is the same as Figure 5.0 (c), except the colour scale has been extended to 950 m s⁻¹. As was found during *MS1*, two echo populations with different spectral widths are shown, those with very low spectral width (black; <50 m s⁻¹), and those with unusually large spectral widths (green; ~500 m s⁻¹). Figure 5.3 are summary plots enlarged on the time interval of the central dawn meteor enhancement shown in Figure 5.2, and part (c) clearly shows the two kinds of meteor echoes.

Table 2.0 (Chapter 2) gave the characteristics of meteor echoes used by Hall *et al.* (1997) and Arnold *et al.* (2001, 2003). According to diffusion theory, the spectral widths of meteor echoes should be small, <50 m s⁻¹. Arnold *et al.* (2001) found the spectral width distributions also had a characteristic diurnal variation, as well as an ~1 m s⁻¹ increase in

spectral width for each range gate. At further ranges, low spectral width, low altitude signals were lost, resulting in an increase of spectral width with range, consistent with diffusion theory.

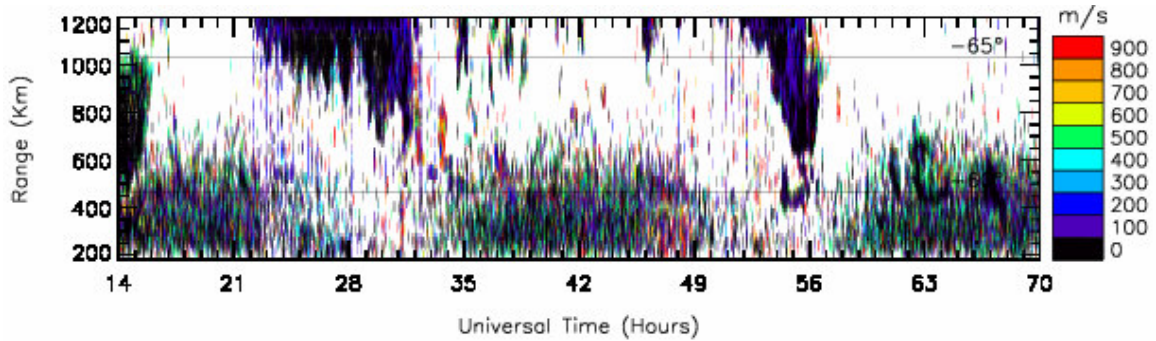


Figure 5.2: MS2 spectral width (m s^{-1}) data recorded from 14 UT, 23 May to 22 UT, 25 May, 2003. Two populations of spectral width echoes are evident (green and black).

The probability distribution functions (PDFs) of the spectral widths shown in Figure 5.2 are presented in Figure 5.4. Each calculation was performed using a 30-km range window between 180 and 570 km. This maximum range reduced the amount of contamination caused by ionospheric echoes. For spectral widths below 100 m s^{-1} , there is evidence the spectral widths increase with range, consistent with the results of Arnold *et al.* (2001). Although very low spectral widths ($<100 \text{ m s}^{-1}$) are predominant, there is also a significant distribution with mode value 460 m s^{-1} . There is a minor overall increase in the relative importance of this secondary distribution, but the mode value remains at $\sim 460 \text{ m s}^{-1}$.

Table 5.1: Mode spectral width values for given range gates.

Range (km)	Spectral Width (m s^{-1})
180–210	7.5
300–330	7.5
360–390	7.5
420–450	22.5
480–510	7.5
540–570	22.5

The mode values corresponding to the PDFs shown in Figure 5.4 are listed in Table 5.1. These results were calculated using a 15 m s^{-1} bin size.

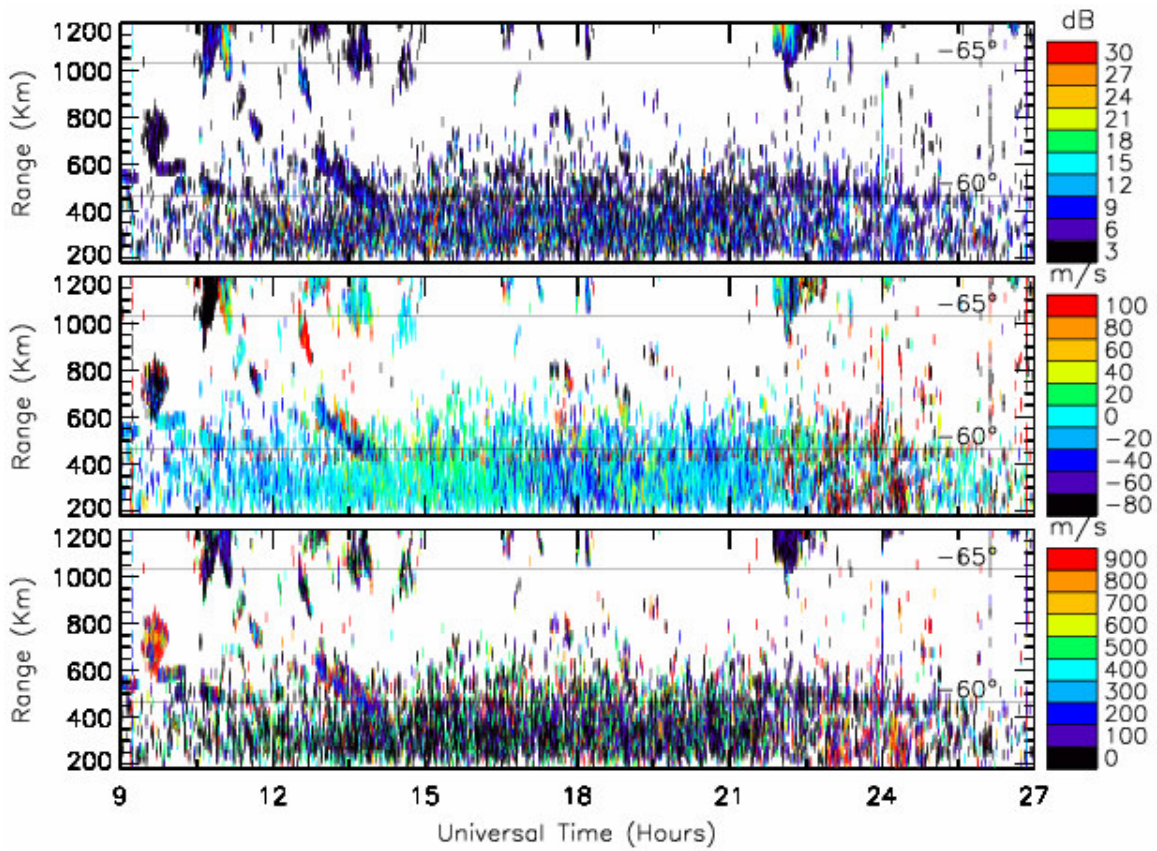


Figure 5.3: Summary plot of basic echo parameters measured during 09 UT on 24 May to 03 UT on 25 May, 2003. The dawn enhancement of meteor echo flux was centred near 18 UT (4 am LT). Two spectral width distributions are evident (green and black).

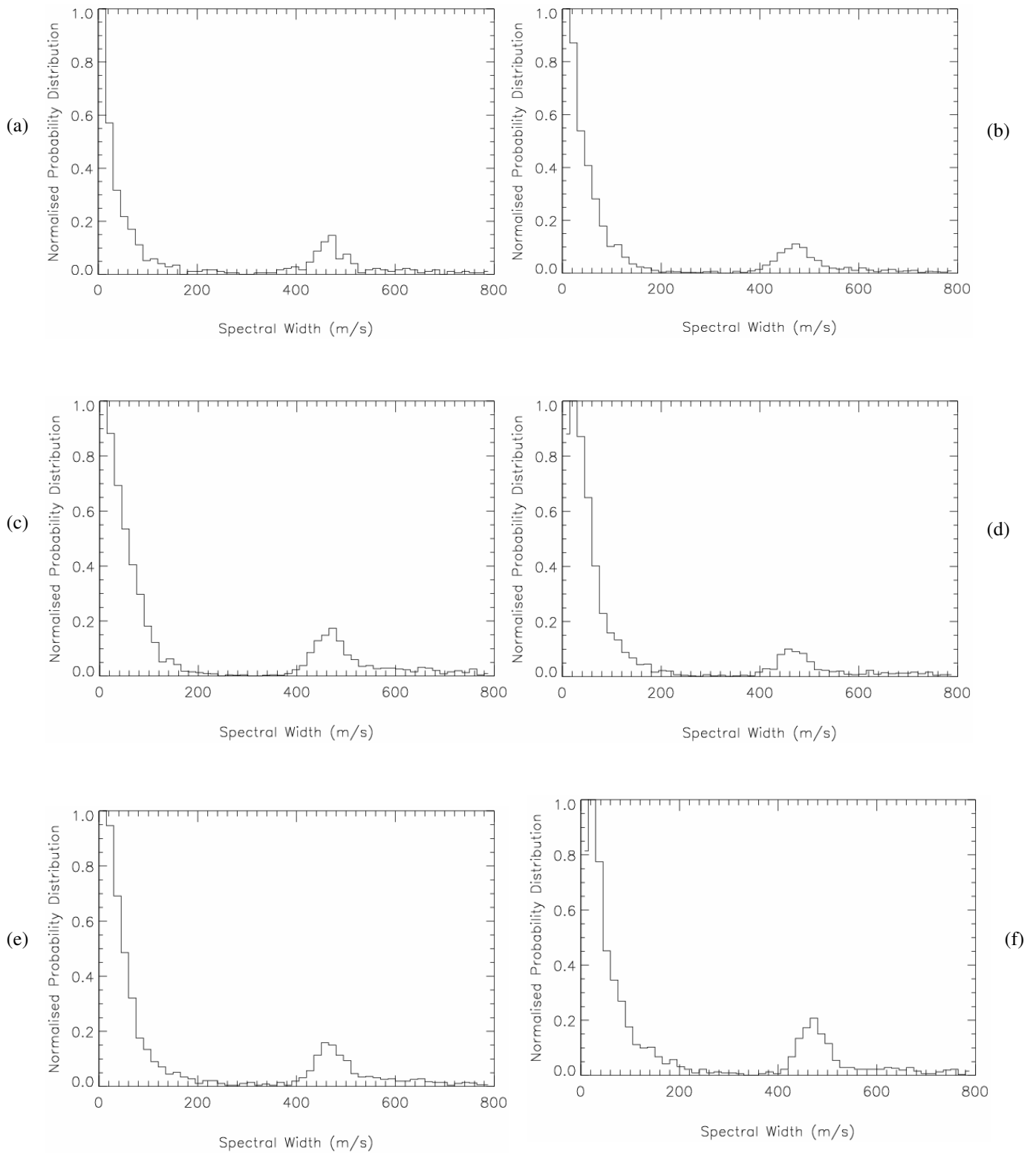


Figure 5.4: PDFs of Doppler spectral width recorded on beam 7 during 14 UT on 23 May to 22 UT on 25 May, 2003. Separate PDFs were calculated for six 30-km wide range windows: (a) 180–210 km, (b) 300–330 km, (c) 360–390 km, (d) 420–450 km, (e) 480–510 km, and (f) 540–570 km.

5.4 Echoes Recorded at Frequency 12 MHz With Spectral Width 300–600 m s⁻¹

In order to determine the origin of the echoes with unusually large spectral width, a spectral width band of 300–600 m s⁻¹ was isolated, and the corresponding power, velocity, and height characteristics investigated. The results are summarised by the summary plot, Figure 5.5, and the PDFs, Figure 5.6. Figure 5.5 confirms these echoes exhibit the same variations in time and range as meteor echoes (i.e., maximum occurrence near dawn, and mostly at group ranges less than 600 km). The backscatter powers were very low (~3 dB), the LOS velocities were low (<50 m s⁻¹), and the elevation angles and corresponding virtual heights increased rapidly with range.

The five PDFs shown in Figure 5.6 correspond to the five panels shown in Figure 5.6. Figure 5.6 a shows the backscatter power had a mode value of only 1.5 dB. Figure 5.6 b shows the Doppler velocities had a mode value of 1.5 m s⁻¹, and they were positively skewed. Figure 5.6 c shows the mode value of the spectral widths was 457.5 m s⁻¹. Similar to the results obtained for *MSI* data at 14.5 MHz (Figure 4.7 d), Figure 5.6 d reveals two distributions of elevation angles, namely a large peak with mode 35.5°, superimposed on a broader distribution of lower elevation angles. The corresponding virtual heights has two main distributions, one peaking at meteor heights <100 km, and the other in the bottom-side F region.

The relationship between group range and virtual height was investigated further, and the results are summarised in Figure 5.7. At group ranges <350 km, most of the echoes originate from the virtual heights of meteors (<120 km). As the group range increases, the mode value of virtual height increases further from 235 km (Figure 5.7 c) to 305 km (Figure 5.7 e). This implies that many meteor-like echoes emanate from F-region altitudes, but as previously discussed, there are questions about the reliability of the interferometer measurements.

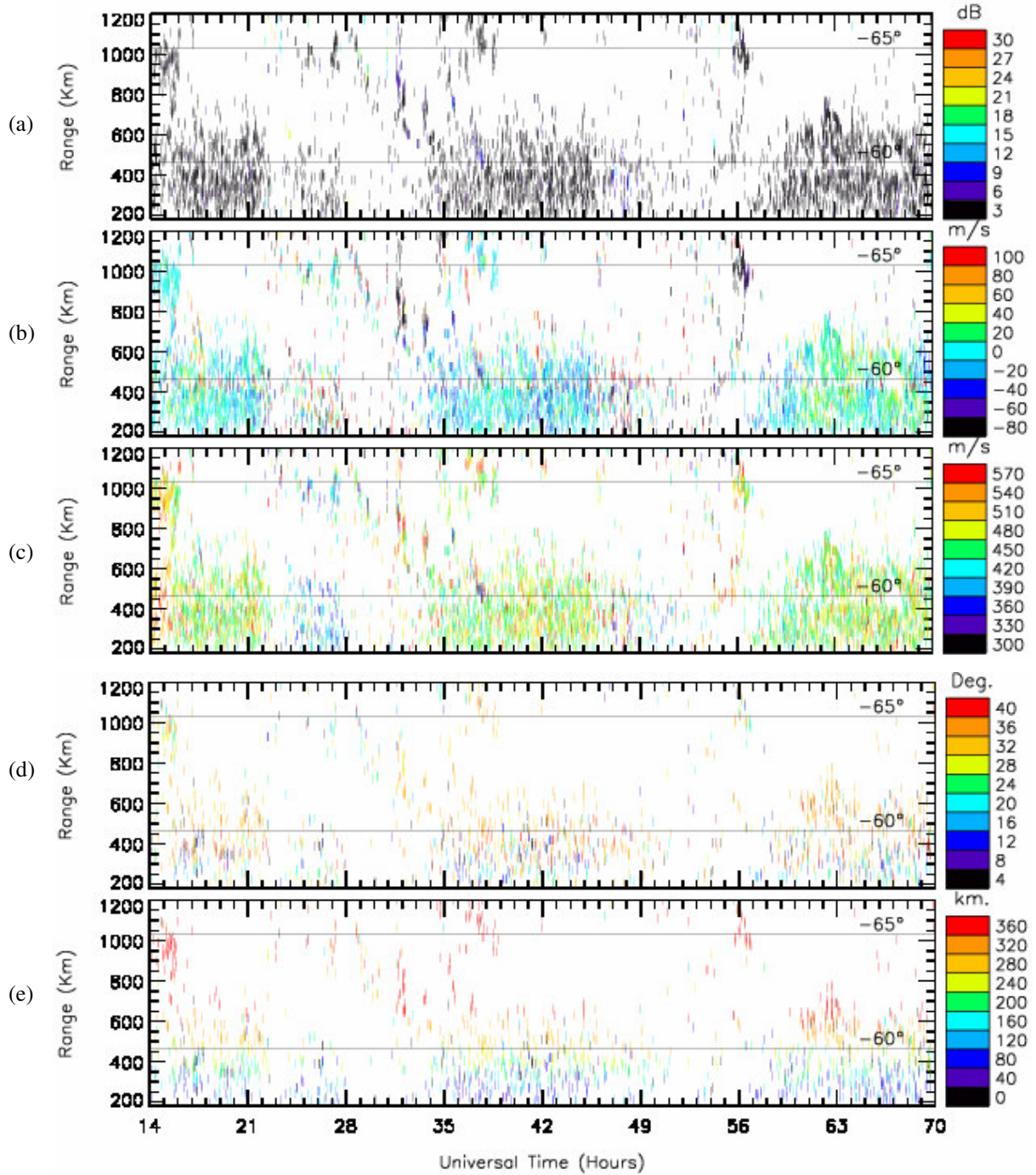


Figure 5.5: Distribution of 300–600 ms^{-1} spectral width echoes: (a) backscatter power (dB), (b) LOS Doppler velocity (m s^{-1}), (c) spectral width (m s^{-1}), (d) elevation angles ($^{\circ}$), and (e) virtual height (km).

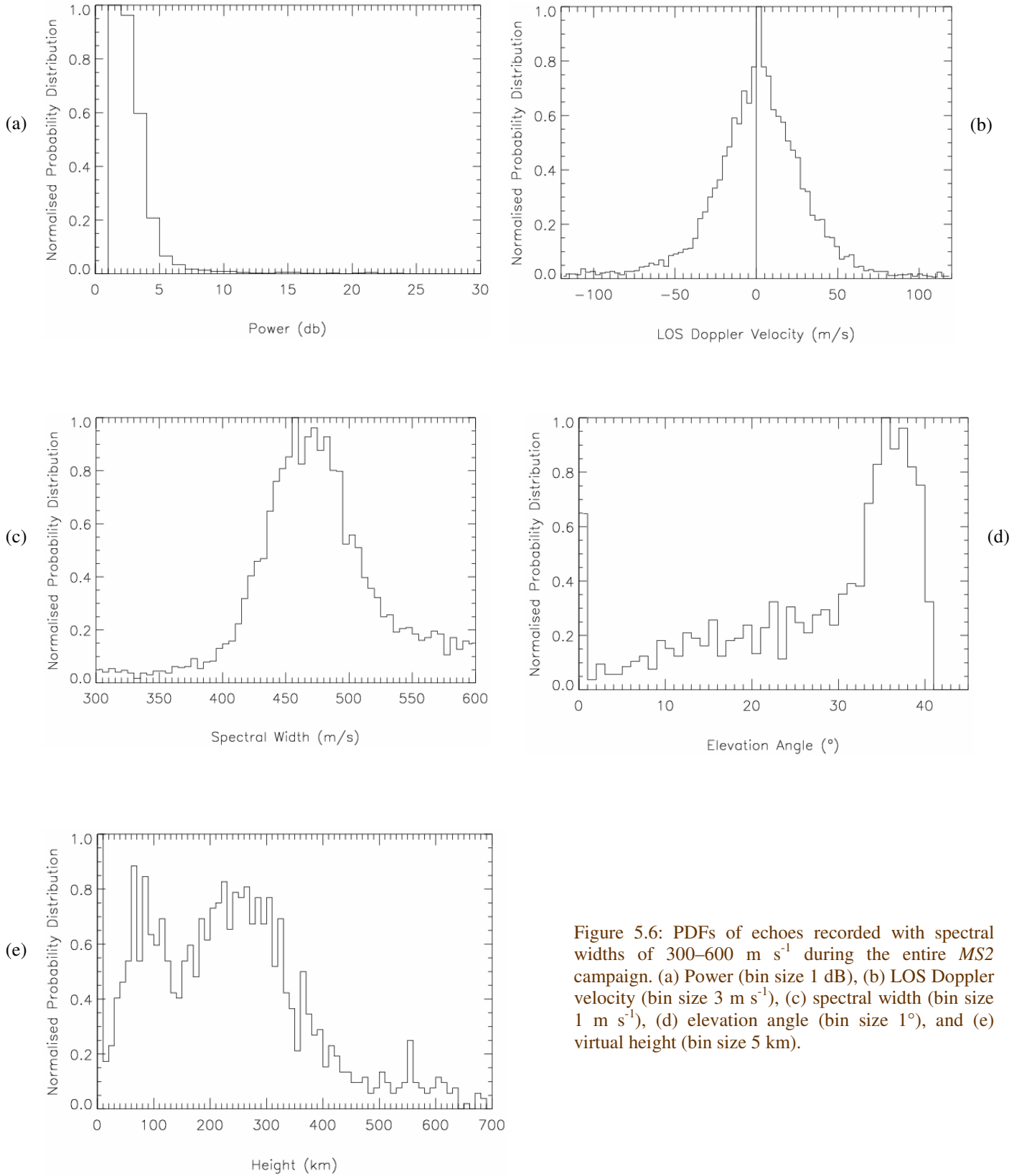


Figure 5.6: PDFs of echoes recorded with spectral widths of 300–600 m s^{-1} during the entire *MS2* campaign. (a) Power (bin size 1 dB), (b) LOS Doppler velocity (bin size 3 m s^{-1}), (c) spectral width (bin size 1 m s^{-1}), (d) elevation angle (bin size 1°), and (e) virtual height (bin size 5 km).

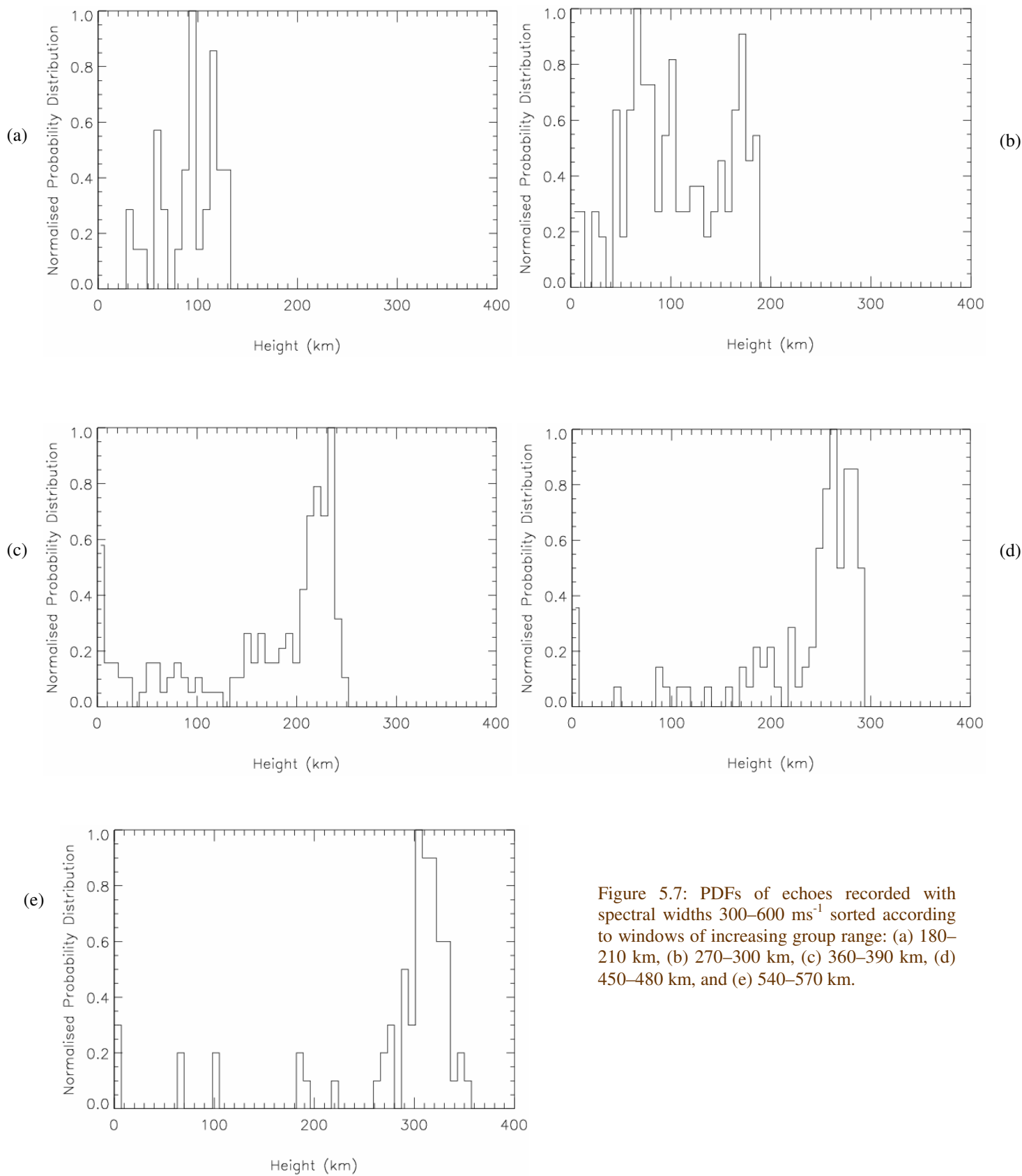


Figure 5.7: PDFs of echoes recorded with spectral widths $300\text{--}600\text{ ms}^{-1}$ sorted according to windows of increasing group range: (a) 180–210 km, (b) 270–300 km, (c) 360–390 km, (d) 450–480 km, and (e) 540–570 km.

5.5 Echoes Recorded at Frequency 12 MHz With Spectral Width $<50 \text{ m s}^{-1}$

Figure 5.8 is a summary plot of the *MS2* echoes recorded with spectral width $<50 \text{ m s}^{-1}$ during 09 UT on 24 May to 03 UT on 25 May, 2003 (i.e., the same time interval as Figure 5.3). Classical diffusion theory presented in Chapter 2 predicts meteor echoes will have spectral widths $<50 \text{ m s}^{-1}$. Arnold *et al.* (2001) found the mean value varied between 10–24 m s^{-1} . Again, Figure 5.8 shows the low backscatter power, LOS velocity, and spectral width, and both the elevation angles and virtual heights increase rapidly with group range.

Again, the five PDFs shown in Figure 5.9 correspond to the five panels shown in Figure 5.8. Overall, the PDFs of the echoes with spectral width $<50 \text{ m s}^{-1}$ (Figure 5.9) are similar to the PDFs of the echoes with spectral width 300–600 m s^{-1} (Figure 5.6). However, the mode value of the power has increased to 4.5 dB, and there are many more echoes with larger power. Whilst the mode value of the LOS velocities is 2 m s^{-1} , this distribution is negatively skewed. Interestingly, a large peak in elevation angle still occurs with a mode value of 35.5° , and many of the corresponding virtual heights are still in the F region, casting further doubts on the reliability of the interferometer.

The meteor echoes with unusually large spectral width had marginal signal-to-noise ratio, and the large spectral widths are also inconsistent with diffusion theory. It is concluded that these echoes may also be caused by plasma instabilities or neutral turbulence acting upon the meteor trails.

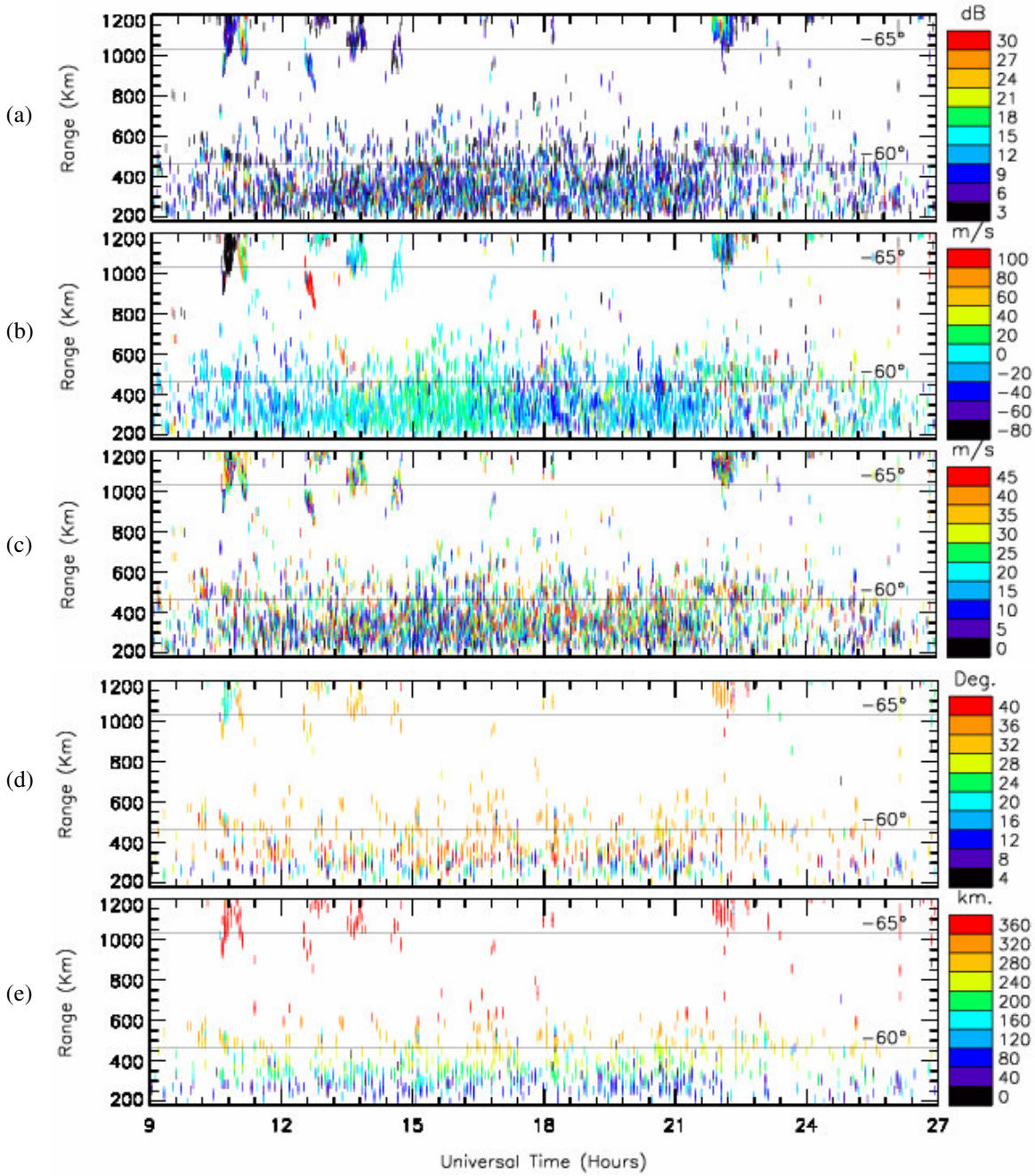


Figure 5.8: Summary plot of *MS2* echoes recorded with spectral width $< 50 \text{ m s}^{-1}$ during the central dawn enhancement, 09 UT on 24 May to 03 UT on 25 May, 2003. (a) Power (dB), (b) LOS Doppler velocity (m s^{-1}), (c) spectral width (m s^{-1}), (d) elevation angle ($^{\circ}$), and (e) virtual height (km).

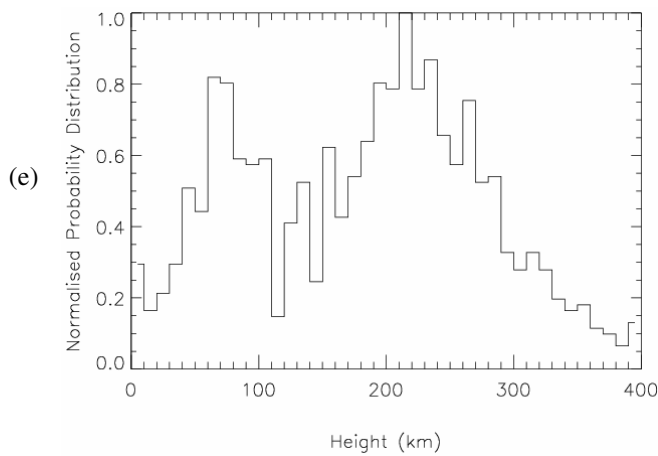
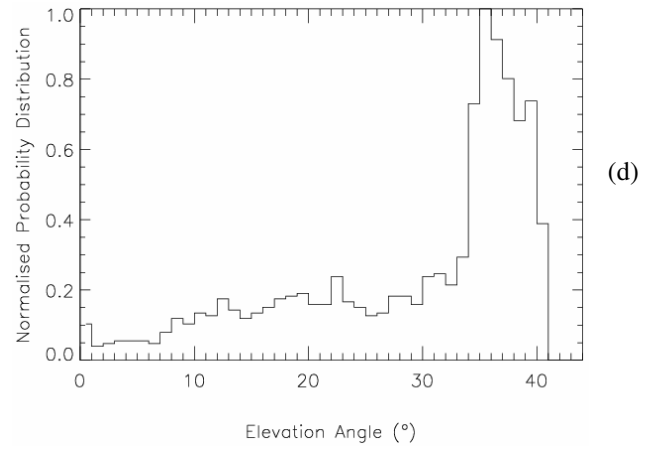
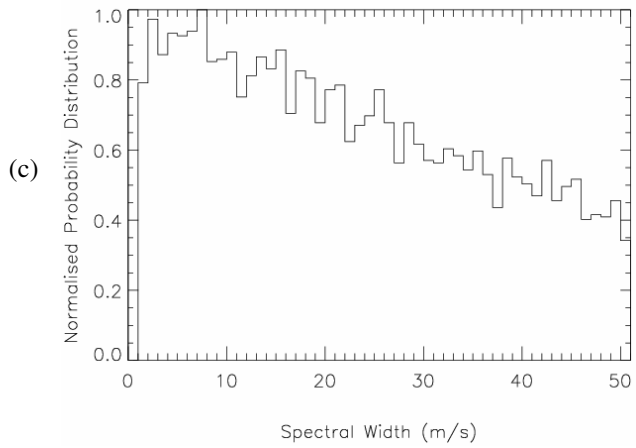
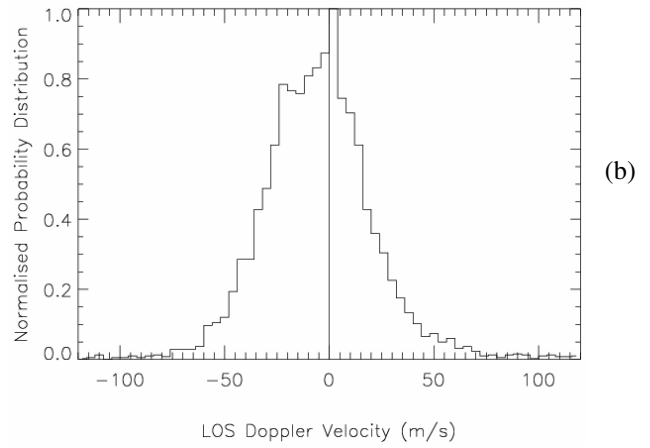
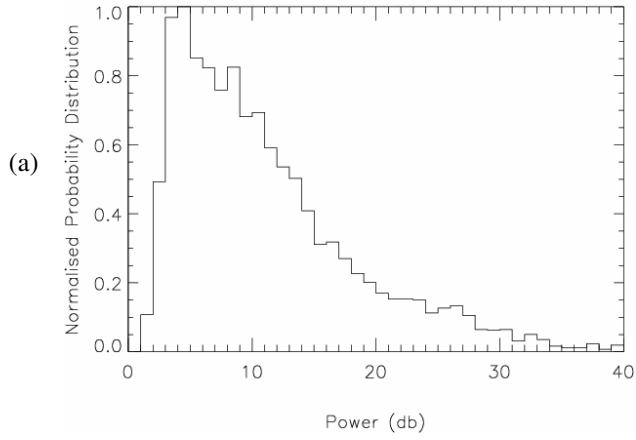


Figure 5.9: PDFs of echoes recorded with spectral width $<50 \text{ m s}^{-1}$ during 09 UT on 24 May to 03 UT on 25 May, 2003. (a) Power (bin size 1 dB), (b) LOS Doppler velocity (bin size 4 m s^{-1}), (c) spectral width (bin size 1 m s^{-1}), (d) elevation angle (bin size 1°), and (e) virtual height (bin size 10 km).

Figure 5.10 is identical to Figure 5.9 (e), except elevation angles greater than 32° were excluded when calculating the virtual heights. The occurrence of F-region echoes has been subdued, and echoes from meteor altitudes dominate the distribution. The removal of high elevation angle rays is suggested when producing final quality assured meteor plots.

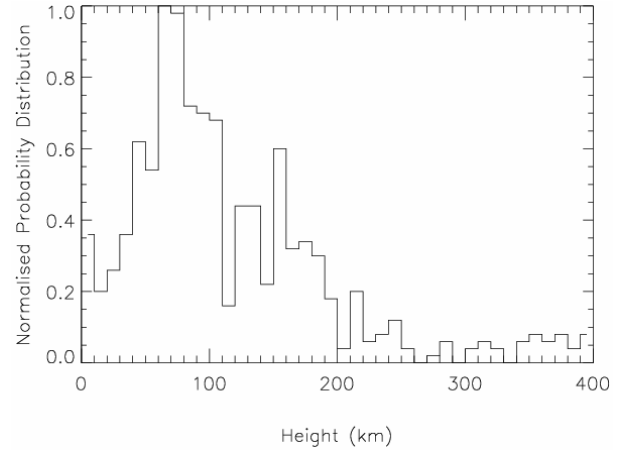


Figure 5.10: PDF of virtual heights recorded with spectral width $<50 \text{ ms}^{-1}$ and elevation angle $<32^\circ$ during 09 UT on 24, May to 03 UT on 25 May, 2003.

Summary and Conclusions

The operation of the TIGER SuperDARN radar was optimised for the detection of meteor echoes. The results of all three TIGER meteor discretionary campaigns have been combined to produce a list of the radar operating and data analysis parameters required to maximise the detection of meteor echoes, yet minimise the contamination by ionospheric echoes. The parameters compiled were based on the results of the “*Meteor_Freq*,” “*Meteor_Scan1*,” and “*Meteor_Scan2*” campaigns, and are presented in Table S.0.

If not for hardware and software limitations of the radar, a first range as low as 60 km would be optimum. Our radar control programs showed that TIGER is currently unable to detect meteor echoes at such close ranges. *MS2* ran with range separation and pulse widths of 15 km, and this proved successful at increasing the number of meteor echoes. Ditto for the 2-sec integration time, but trials using 1-sec integration time might also prove successful. The *MF* campaign showed that 12 MHz was probably the best frequency for detecting meteor echoes. It was also shown the operating frequency should be fixed to prevent echo outages.

When analysing the data, the following parameters are recommended for rejecting ionospheric echoes. Although ionospheric echoes do appear at group ranges <600 km, the vast majority appear at greater ranges. Most of the meteor echoes had Doppler velocities between 50 m s⁻¹ and 50 m s⁻¹, and spectral widths <50 m s⁻¹. The spectral width limit is consistent with diffusion theory, and is in agreement with the results of Arnold *et al.* (2003). Finally, taken at face value, the interferometer results suggest that echoes with elevation angle ≤32° should be rejected. This seemed to eliminate echoes from above the altitude region of meteors, 80–120 km.

Table S.0: Optimum radar operating and data analysis parameters required for the detection of meteor echoes.

Parameter	Optimum Value
First range	120 km
Range separation	15 km
Pulse width	15 km
Integration time	2 sec
Day frequency	12,050 kHz
Night frequency	12,050 kHz
Range	<600 km
Power	3–30 dB
Doppler Velocity	±50 ms ⁻¹
Spectral Width	<50 ms ⁻¹
Elevation Angle	<32 °
Height	<120 km

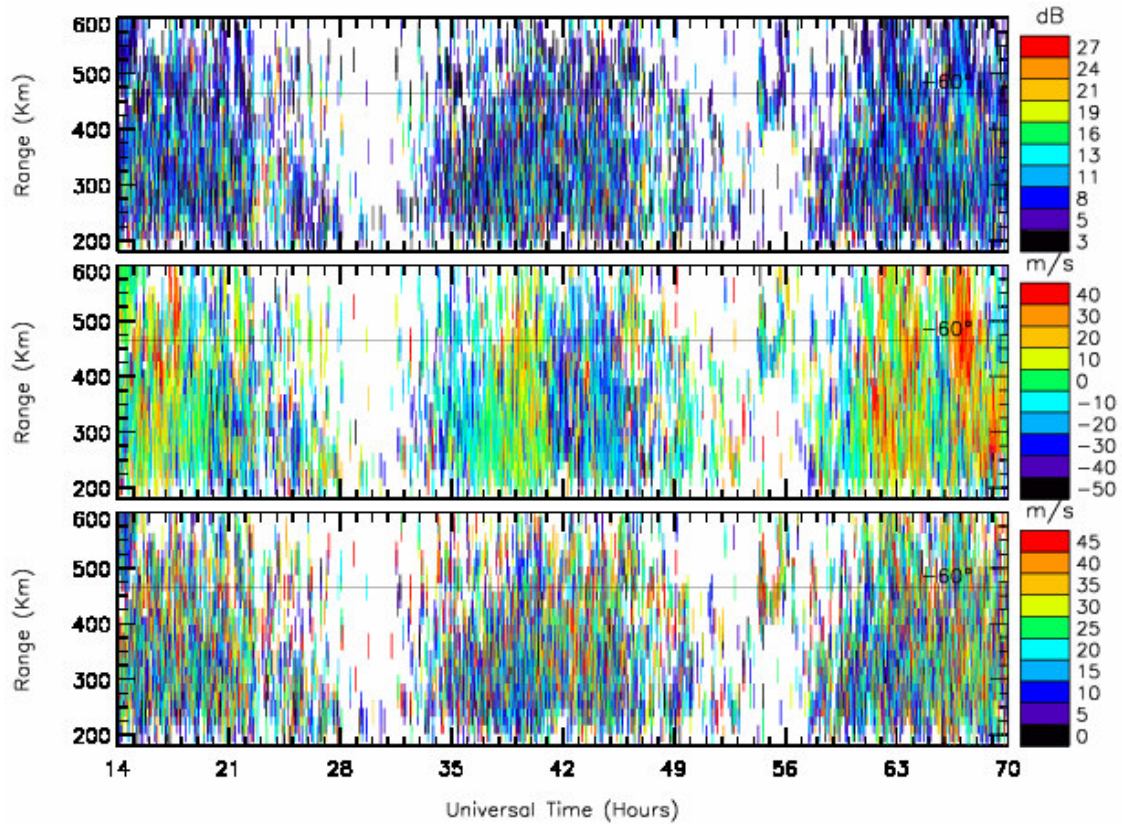


Figure S.0: Final, quality assured summary plot of meteor echoes recorded during 14 UT on 23 May to 22 UT on 25 May, 2003.

The preceding criteria are similar to those found in other SuperDARN radar studies (Hall *et al.* 1997 and Arnold *et al.* 2001). Any one of these criteria will not guarantee the identification of meteor echoes, but when combined, they should be reliable in the majority of cases. Figure S.0 is a final, quality assured summary plot of meteor echoes identified using the criteria given in Table S.0. Very few ionospheric echoes remain in this plot; even so, as will be explained in the following section, these results can still be improved upon.

A population of echoes with spectral widths of 300–600 m s^{-1} was found to contaminate the meteor echoes. Except for their unusually large spectral widths, these echoes had the same characteristics as meteor echoes, and they probably were meteor echoes. Their large spectral widths were probably an artefact generated by FITACF when it processes echoes

with marginal signal-to-noise ratio. However, the large spectral widths may also have been caused by a plasma instability acting upon the meteor trails, or other irregularities in the mesosphere-lower thermosphere.

Finally, descending plasma streams (DPSs) were discovered during the *MF* campaign (see Figure 3.3), and they were also observed during *MS1* and *MS2* campaigns. These ionospheric echo traces began to descend in group range during the late afternoon and evening, and eventually merged into and contaminated the GNREs during the early morning. The interferometer data suggests they were caused by echoes from F-region irregularities at further ranges, but as they approached to the range of GNREs, they gradually became echoes from E-region irregularities.

The exploration of DPS events was not germane to this thesis which focuses on meteor echoes. However, preliminary comparisons of DPS events and magnetograms recorded at Macquarie Island (54.5°S, 158.9°E) show the equatorward expansions and poleward contractions were synchronised with deflections of the geomagnetic *X* component (i.e., auroral current surges in the zonal direction). Coincident observations of precipitating particles made with the Defense Meteorology Satellite Program (DMSP) satellite suggest the DPS traces were collocated with the equatorward edge of the auroral oval. One particular pass of the DMSP F13 satellite revealed 10-keV proton aurora were coincident with the location of the DPS event. The large backscatter powers sometimes observed by TIGER suggests that DPS traces included total reflections from the poleward wall of the main ionospheric trough, a feature well known to form at the equatorward edge of the auroral oval before midnight.

Hence we conclude the DPS events were a relative of the slow long-lived E region plasma structures (SLERPS) reported by Jayachandran et al. (2000). However, their behaviour was also reminiscent of the behaviour of tidal ion layers and ion rain observed by incoherent scatter radars (Mathews et al., 1997).

Future Work

The TIGER radar, and SuperDARN radars in general, require further development to increase the number and accuracy of meteor echo measurements. Meteor detection rates might be greatly increased by reducing the first group range to ~90 km, or even less, but TIGER is currently unable to detect echoes at such close range. The use of range separations of 15 km, or less, will improve the height resolution of meteor echoes and winds. The software required to record in-phase and quadrature samples with high time resolution is presently under development (Yukimatu et al., 2002). The results will eventually enable identification of various meteor echo types (e.g., underdense meteors), as well as echoes from ionospheric instabilities. The ability to measure the life time of underdense meteor echoes, combined with diffusion theory, will improve the height resolution of meteor winds.

The ability of the TIGER interferometer to accurately and unambiguously measure the elevation angles of echoes is a concern. This is so important because the elevation angles almost provide a direct means of inferring the heights of meteor echoes. The main and interferometer receiver channels require calibration, so that they produce the same phase shift versus frequency and signal-processing gain. An aircraft equipped with a transponder might be used to validate the elevation angle measurements.

Unfortunately, an elevation angle measurement is not obtained for every echo recorded by the main antenna array. This happens because the main array consists of 16 elements, whereas the interferometer array only consists of 4 elements, whence the power is a factor of $(16/4)^2 = 16$ weaker — an important consideration for meteor echoes detected with marginal signal-to-noise ratio. Increasing the size of the interferometer array to 16 elements would be ideal, though perhaps prohibitively expensive.

Various populations of echoes were detected amidst the GNREs, and the criteria used to separate them were developed. Analysis software which uses the beam-swinging technique to calculate the mesospheric winds using the different populations needs to be

developed. The winds thus obtained can then be compared to determine if the different kinds of echoes actually emanate from the same atmospheric region. The TIGER meteor winds might also be validated by comparing them with those measured by a classical meteor radar set-up on Bruny Island.

Whilst probably a signature of the equatorward edge of the auroral oval, the descending plasma streams (DPSs) require further investigation. This will involve comparing them with geomagnetic indices, ground-based magnetometer and ionosonde data, and satellite-based data. This might help clarify the conditions when they occur, and contaminate the GNREs, as well as improve upon the method used to reject them.

Appendix A

BAS .met File Contents

Figure A.1: Sample .met file

```
# met file
# Created by $Id: file_util.c,v 2.0 2001/02/14 11:28:58 root
Exp $
# Criteria
Vlos(max)=100.00
S/N(min)=3.00
range(max)=405
Verr(max)=50.00
num_beams(min)=5
w_l(max)=99999.00
# Beam for meridional wind
beam_num=2
wind=meridional
# Station ID
st_id=10
# year,month,day,hour,Vx,Vy,lat,long,Vm,Vm_lat,Vm_long,num_avgs
2000,03,01,01,2,-9,64.6,25.2,-3,64.3,23.6,295
# sdev_vx,sdev_vy
5.53,14.39
# used frang=180 and rsep=45
```

Appendix B

Separation of Results According to Frequency

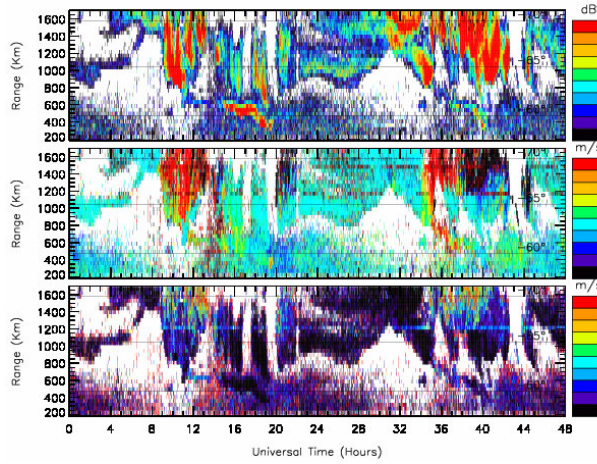


Figure B.1: Summary Plot of 11,400 KHz transmission frequency results

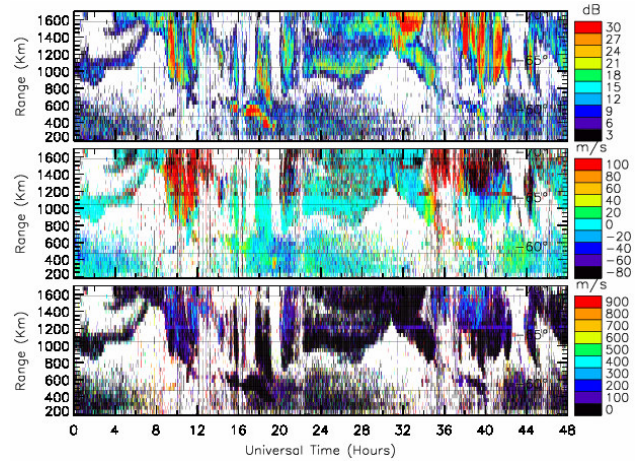


Figure B.2: Summary Plot of 11,650 KHz transmission frequency results

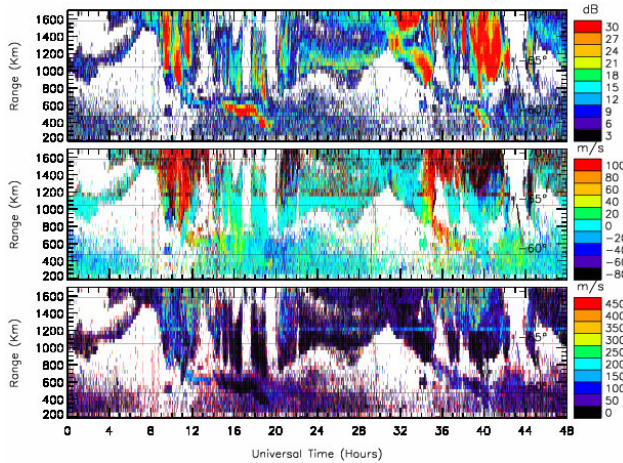


Figure B.3: Summary Plot of 12,050 KHz transmission frequency results

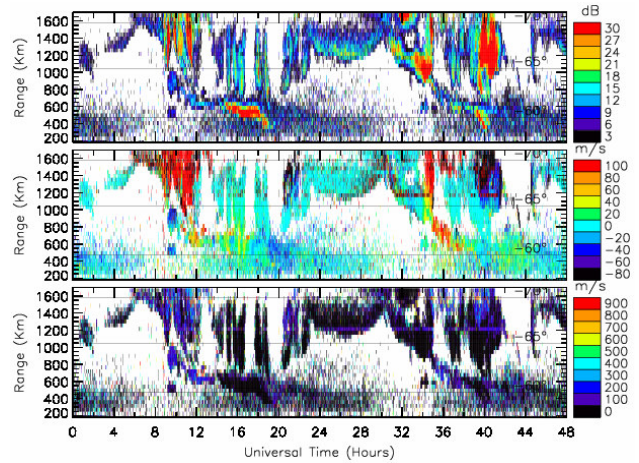


Figure B.4: Summary Plot of 13,410 KHz transmission frequency results

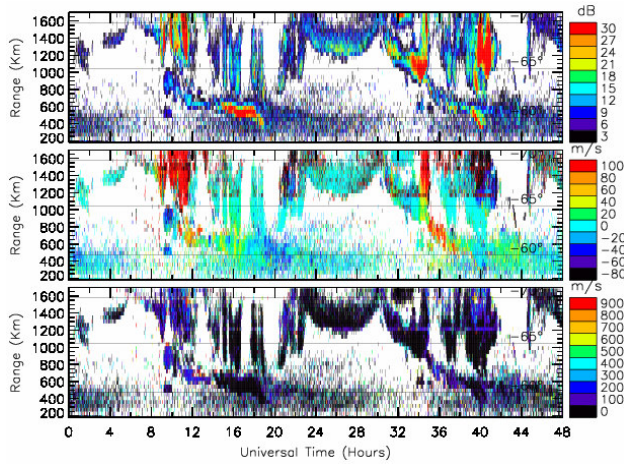


Figure B.5: Summary Plot of 13,800 KHz transmission frequency results

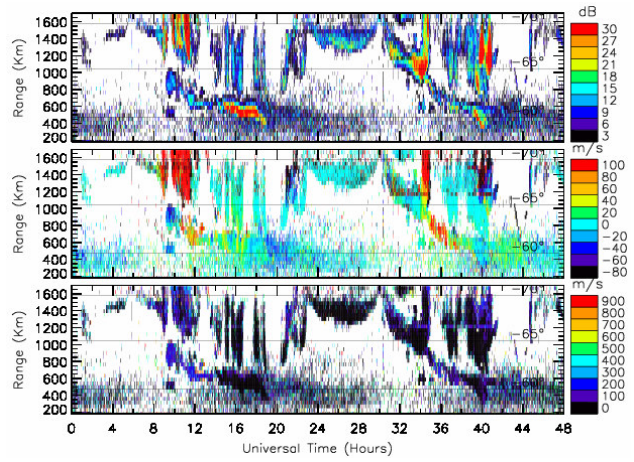


Figure B.6: Summary Plot of 14,350 KHz transmission frequency results

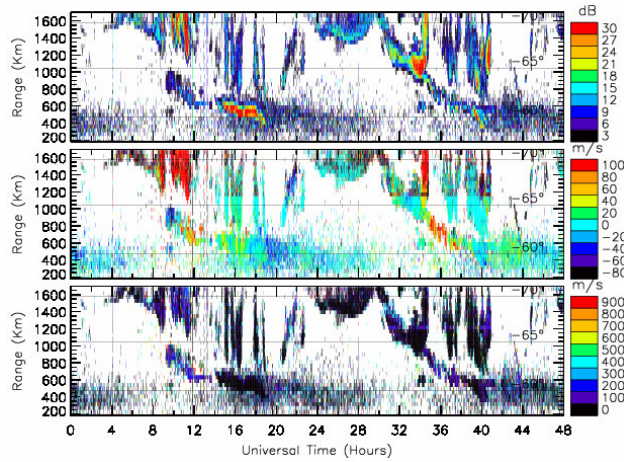


Figure B.7: Summary Plot of 15,100 KHz transmission frequency results

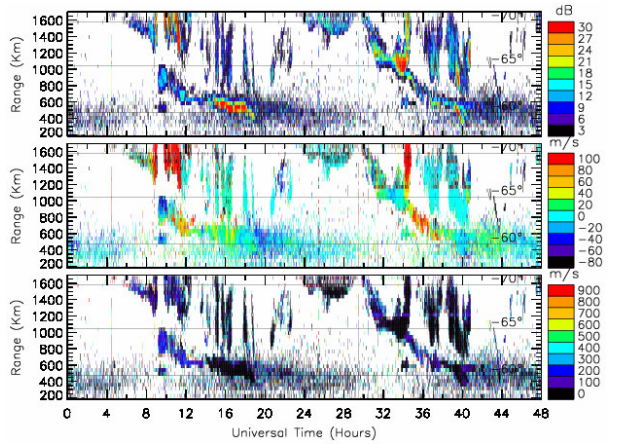


Figure B.8: Summary Plot of 15,600 KHz transmission frequency results

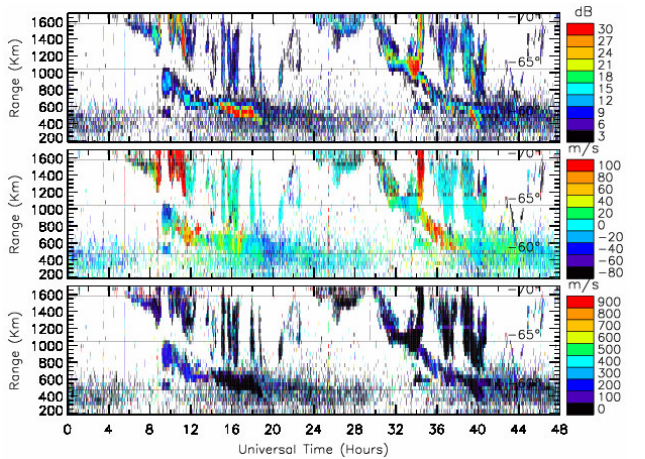


Figure B.9: Summary Plot of 15,800 KHz transmission frequency results

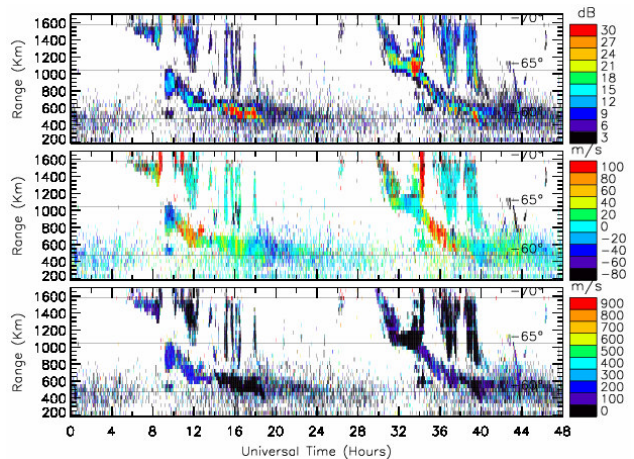


Figure B.10: Summary Plot of 17,410 KHz transmission frequency results

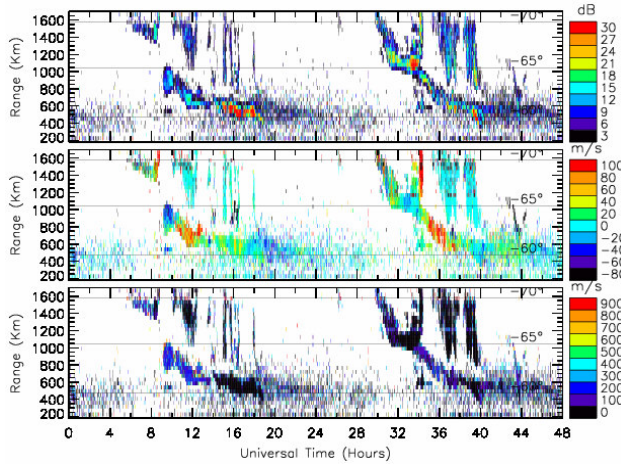


Figure B.11: Summary Plot of 18,030 KHz transmission frequency results

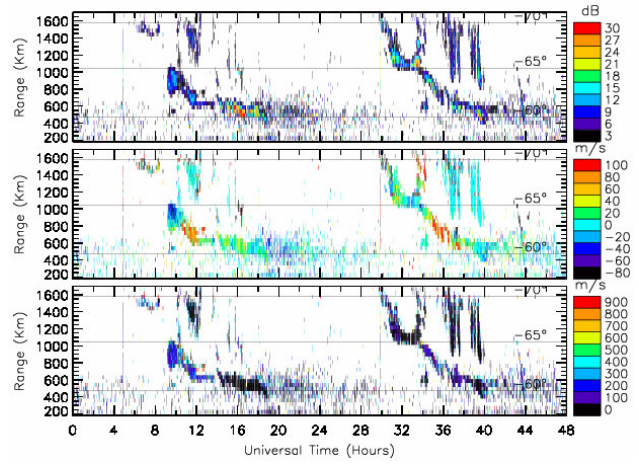


Figure B.12: Summary Plot of 18,168 KHz transmission frequency results

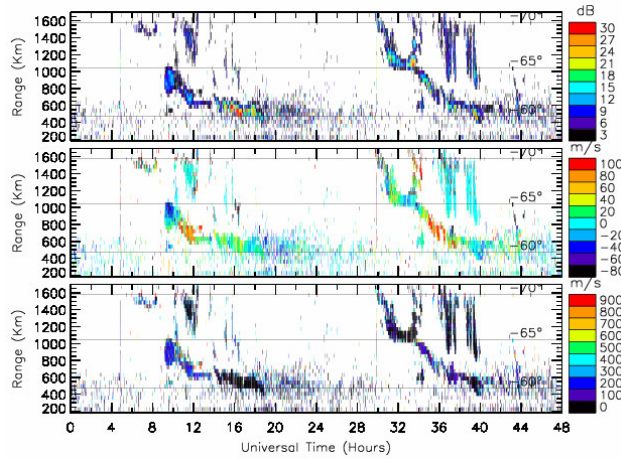


Figure B.13: Summary Plot of 18,900 KHz transmission frequency results

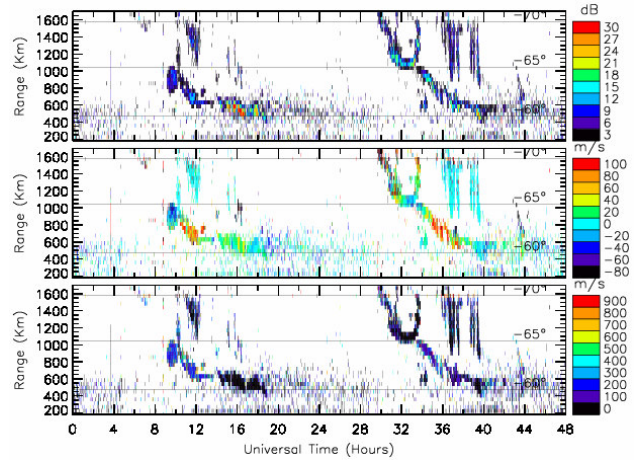


Figure B.14: Summary Plot of 19,020 KHz transmission frequency results

Bibliography

- Arnold, N.F., Cook, P.A., Robinson, T.R. et al. 2001. *Super Dual Auroral Radar Network observation of fluctuations in the spectral distribution of near range meteor echoes in the upper mesosphere and lower thermosphere*. *Annales Geophysicae*, vol. 19, pp. 425–434.
- Arnold, N.F., Robinson, T.R., Lester, M. et al. 2003. *Comparison of D-region Doppler drift winds measured by the SuperDARN Finland HF radar over annual cycle using the Kiruna VHF meteor radar*. *Annales Geophysicae*, 2nd revised edition, submitted January 2003.
- Baker, K.B., Dudeney, K. B., Greenwald, R.A. et al. 1995. *HF radar signature of cusp and low-latitude boundary layer*. *Journal of Geophysical Research*, vol. 100, A5, pp. 7,671–7,695.
- Barnes, Rob. SuperDARN, [web page] <http://superdarn.jhuapl.edu/sites/index.html>
- Berkey, F.T., Fish, C.S., Jones, G.O. 2001. *Initial observations of mesospheric winds using IDI radar measurements at Bear Lake Observatory*. *American Geophysical Union Research Letters*, vol. 28, pp. 1135–1138.
- Brown, P., Simek, M., Jones, J. et al. 1998. *Observations of the 1996 Leonid meteor shower by radar, visual and video techniques*. *Royal Astronomy Society*, vol. 300, pp. 244–250.
- Dyson, P. L., Devlin, J. C. 2000. *The Tasman International Geospace Environment Radar*. *The Physicist (The Australian Institute of Physics)*, vol. 37, pp. 48–53.
- Dyson, P. L., Devlin J.C., Parkinson, M. L. et al. 2003. *The Tasman International Geospace Environment Radar (TIGER) - Current Development and Future Plans*. *IEEE Proceedings of the International Conference on Radar*, pp. 282–287.
- Fritts, D.C., Alexander, M.J. 2003. *Gravity wave dynamics and effects in the middle atmosphere*. *Reviews of Physics*, vol. 41.
- Garbe, G.P., Cogger, L.L. 1997. *The winter mesopause field at 51° north*. *Journal of Atmospheric and Solar-Terrestrial Physics*, vol. 59, no 16, pp. 1999–2008.
- Gardner, C.S., Zhao, Y., Liu, A.Z. 2002. *Atmospheric stability and gravity wave*

- dissipation in the mesopause region*. Journal of Atmospheric and Solar-Terrestrial Physics, vol. 64, pp. 923–929.
- Gebhardt, P. *Radio Detection of Meteors* <http://www.odxa.on.ca/meteor2.html>, [web page] Date accessed 03/03/03.
- Greenwald, R.A., Baker, K.B., Hutchins, R.A. et al. 1985. *An HF phased-array radar for studying small-scale structure in the high-latitude ionosphere*. Radio Science, vol. 20, 1, pp. 63–79.
- Greenwald, R.A., Baker, K.B., Dudeney, J.R., et al. 1995. *DARN/SuperDARN: A global view of the dynamics of high latitude convection*. Space Science Review, vol. 71, pp. 761–796.
- Greet, P.A., Murphy, D.J., Vincent, R., Dyson, P. 2000. *A companion of optical and radar measurements of mesospheric winds and tides*. Geophysical Research Letters, vol. 27, 16, pp. 2477–2480.
- Hall, C.M., Röttger, J. 2001. *Initial observation of Polar Mesospheric Summer Echoes using the EISCAT Svalbard radar*, Geophysical Research Letters, vol. 28, 1, pp. 131–134.
- Hall, G.E., MacDougall, J.W., Moorcroft, D.R. et al. 1997. *Super Dual Auroral Radar Network observations of meteor echoes*. Journal of Geophysical Research, vol. 102, A7, pp. 14603 – 14614.
- Hargreaves, J.K. 1992. *The Solar-Terrestrial Environment*. Cambridge: Cambridge University Press.
- Hathaway, D.H. *Solar Physics: Coronal Mass Ejections* (2003) <http://science.nasa.gov/ssl/pad/solar/cmes.htm>
- Hussey, G.C., Meek, C.E., André, D. et al. 2000. *A comparison of Northern Hemisphere winds using SuperDARN meteor trail and MF radar wind measurements*. Journal of Geophysical Research, vol. 105, D14, pp. 18053 – 18066.
- Igarashi, K., Namboothiri, S.P., Kishore, P. 2002. *Tidal structure and variability in the mesosphere and lower thermosphere over Yamagawa and Wakkanai*. Journal of Atmospheric and Solar-Terrestrial Physics, vol. 64, pp. 1037 – 1053.
- Jayachandran, P.T., St.-Maurice, J.-P., MacDougall, J.W., Moorcroft, D.R. 2000. *HF*

- detection of slow long-lived E region plasma structures.* Journal of Geophysical Research, vol. 105, A2, pp. 2425–2442.
- Jaquith, N. *From There to Here: Interplanetary Space and the Magnetosphere*
<http://www-istp.gsfc.nasa.gov/istp/outreach/theretohere.html>.
Date accessed: 01/11/03.
- Jenkins, B., Jarvis, M.J. 1999. *Mesospheric winds derived from SuperDARN HF radar meteor echoes at Halley, Antarctica.* Earth Planets Space, vol. 51, pp. 685 – 689.
- Kivelson, M.G., Russell, C.T. 1995. *Introduction to Space Physics.* Cambridge University Press, UK.
- MacDougall, J.W., Li, X. *Meteor observations with a modern digital ionosonde.* Journal of Atmospheric and Solar-Terrestrial Physics, vol. 63, pp. 135 – 141.
- Marsh, S.H. et al. 2000. *Measuring meridional mesospheric winds with the AMOR meteor radar.* Journal of Atmospheric and Solar-Terrestrial Physics, vol. 62, pp. 1129 – 1133.
- Mathews, J.D., Sulzer, M.P., Perillat, P. 1997. *Aspects of layer electrodynamics inferred from high-resolution ISR observations of the 80-270 km ionosphere.* Geophysical Research Letters, vol. 24, 11, pp. 1411 – 1414.
- Mathews, J.D., Doherty, J., Wen, C.-H., et al. 2003. *An update on UHF radar meteor observations and associated signal processing techniques at Arecibo Observatory.* Journal of Atmospheric and Solar-Terrestrial Physics, vol. 65, pp. 1139 – 1149.
- Mlynozok, M. 2002. *A comparison of space-based observations of the energy budgets of the mesosphere and troposphere.* Journal of Atmospheric and Solar-Terrestrial Physics, vol. 64, pp 877 – 887.
- Nakamura, T., Morita, S., Tsuda, T., Fukunishi, H., Yamada, Y. 2002. *Horizontal structure of the wind velocity field around the mesopause region derived from meteor radar observations.* Journal of Atmospheric and Solar-Terrestrial Physics, vol. 64, pp. 947 – 958.
- Ogawa, T., Nishitani, N. *Upper mesosphere summer echoes detected with the*

- Antarctic Syowa HF radar. 2002. Geophysical Research Letters, vol. 29 no. 7, pp. 61-1 – 61-4.*
- Parker, E.N. 1963. *Interplanetary Dynamical Processes*. New York: Wiley-Interscience.
- Parkinson M. L. et. al. 1998. *On the role of electric field direction in the formation of sporadic E-layers in the southern polar cap ionosphere*. *Journal Atmospheric and Solar-Terrestrial Physics*, vol. 60, pp. 471-491.
- Rao, J. 2001. *Leonids 2001: The Saga Continues*. *Sky & Telescope*, November 2001.
- Raymundo, P. *Meteor Images*, [web page] (2001)
http://spaceweather.com/meteors/gallery_18nov01_page4.html
- Schlegel, K. 1996. *Coherent backscatter from ionospheric E-region plasma irregularities*. *Journal of Atmospheric and Solar-Terrestrial Physics*, vol. 58, pp. 933 – 941.
- Schlegel, K., Gurevich, A.V. 1997. *Radar backscatter from plasma irregularities of the lower E region induced by neutral turbulence*. *Annales of Geophysicae* vol. 15, pp. 870 – 877.
- Taylor, M.J., Gadsden, M., Lowe, R.P. et al. 2002. *Mesospheric cloud observations at unusually low altitudes*. *Journal of Atmospheric and Solar-Terrestrial Physics*, vol. 60, pp. 991 – 999.
- Thayaparan, T., Hocking, W.K. 2002. *A long term comparison of winds and tides measured at London, Canada (43° N, 81° W) by co-located MF and meteor radars during 1994-1999*. *Journal of Atmospheric and Solar-Terrestrial Physics*, vol. 64, pp. 931 – 946.
- Thomas, G.E. 1991. *Mesospheric clouds and the physics of the mesopause region*. *Reviews of Geophysics* vol. 29, pp. 553 – 575.
- Viereck, R.A. 1991. *A review of mesospheric dynamics and chemistry*. *Reviews of Geophysics Supplement*, pp. 1132 – 1142.
- Walker, J.K., Stauning, P., Troshichev, O. *Space Weather: Timely synoptic modelling of the northern E region electrodynamics*, [web page]
<http://pages.istar.ca/~jwalker/ionosphe.html>. Date accessed: 05/06/03.
- Yukimatu, A.S., Tsutsumi, M. 2002. *A new SuperDARN meteor wind measurement:*

- Raw time series analysis method and its application to mesopause region dynamics.* Geophysical Research Letters, vol. 29.
- Yukimatu, A.S., Tsutsumi, M., Yamagishi, H., Sato, N. 2002. *A new method for monitoring and removing SuperDARN radar DC offsets.* Advances in Polar Upper Atmosphere Research, vol. 16.
- Zielik, M., Gregory, S.A., Smith., E.V.P. 1995 *Introductory Astronomy and Astrophysics*, 3rd Edition. Saunders College Publishing, USA.
- Exploring the Sun*, [web page] (2003), <http://sohowww.nascom.nasa.gov/>.
Date accessed: 05/11/03.
- Hurricane Sol*, [web page]
<http://www-istp.gsfc.nasa.gov/istp/outreach/cmeposter/hurricane.html>.
Date accessed: 10/08/03.
- (2003) *IMO, The International Meteor Organisation*, [web page]
<http://www.imo.net/>. Date accessed: 03/03/03.
- (2002) *Ionosphere*, [web page]
<http://www oulu.fi/~spaceweb/textbook/ionosphere.htm>.
Date accessed: 03/03/03.
- TIMED/CEDAR Global Convection Maps*, [web page]
superdarn.jhuapl.edu/timed/TIMED_Science.jpg. Date accessed: 03/03/03.
http://spaceweb oulu.fi/education/Ionosfaarifysiikka/Ionosfaarifys_5_7.pdf.
Date accessed: 10/08/03.